Second harmonic generation in metallic nanostructured arrays

Hooper, David

Award date:
2019

Awarding institution:
University of Bath

Second harmonic generation in metallic nanostructured arrays

David Charles Hooper
University of Bath

Submitted for the degree of Doctor of Philosophy
February 2019

Supervised by
Professor Ventsislav K. Valev

Centre for Photonics and Photonic Materails
Department of Physics
University of Bath
United Kingdom

Declarations

Copyright notice

Access to this thesis in print or electronically is restricted until .....

Signed on behalf of the Doctoral College .....

Declaration of any previous submission of the work

The material presented here for examination for the award of a higher degree by research has not been incorporated into a submission for another degree.

.....

Declaration of authorship

I am the author of this thesis, and the work described therein was carried out by myself personally. Any contributions made by others is specified within the relevant chapters.

.....

Abstract

The desire to incorporate optical and photonic components into miniaturised devices provides the impetus for the field of nanophotonics to control light at ever decreasing length scales. Traditional optical elements, for instance, lenses, are described by macroscopic properties such as refraction. Designing and building optical elements using these macroscopic properties results in relatively large components that need to be multiple wavelengths thick. This size limitation hinders their integration into small form factor products. One approach to controlling light at the nanoscale is to use plasmonics.

Plasmons are coherent oscillations of the free electrons in a metal and allow light to be confined to nanoscopic volumes. Confining light to small volumes drastically enhances the local electric field, which is particularly favourable for nonlinear optical processes. Utilising nonlinear frequency mixing provides control over the wavelength of light. Therefore, plasmonics is an advantageous platform for nanophotonic control of wavelength. However, engineering plasmonic nanomaterials for nonlinear applications is extremely challenging and would greatly benefit from robust nonlinear characterisation techniques.

This thesis presents the nonlinear characterisation of two metallic nanostructured arrays. The analyses of these characterisations are then related to different physical origins. Presented first are arrays of anisotropic nanoscale helices. The nonlinear chiral optical response of the helices is investigated and how it is affected by anisotropy. It is found that nonlinear chirality cannot be thoroughly characterised without considering sample anisotropy. Secondly, the nonlinear response of nanoparticle arrays that support surface lattice resonances is studied. The electric field enhancements caused by the surface lattice resonances greatly boosts the second harmonic generation of the arrays. Furthermore, the surface lattice resonance dispersion is used to tune this effect.

By providing comprehensive characterisations of these nanomaterials and identifying the physical origins responsible for their nonlinear optical behaviour, this thesis contributes to establishing design rules needed to create practical nonlinear plasmonic nanophotonic systems. The growing body of work on nonlinear plasmonics in nanophotonics will serve as reference guides for future design schemes, enabling the miniaturisation of photonic components able to control the wavelength of light.

Acknowledgments

I would like to thank Ventsislav Valev for his supervision and mentorship over the last four years. Before starting my PhD I had not worked in an optics lab, I do not think Ventsi knew what he was letting himself in for when he took me on. I would also like to thank my friends for supporting through all of this, in particular Joel Collins, Kerrianne Harrington, and Christian Kuppe. Additionally I would like to thank my family, Colin Hooper, Alison Hooper, and Lyndsay Hooper who, to put it bluntly, have put up with and supported me despite my tendency to go incommunicado. Finally, I would be remiss not to thank Jodi Walsh for all of her care and support over all our years together, thank you.

List of publications

[1] **D. C. Hooper**, C. Kuppe, D. Wang, W. Wang, T. W. Odom, and V. K. Valev, "*Second harmonic spectroscopy of surface lattice resonances*", Nano Letters **19**, 165-172 (2019).

[2] J. T. Collins, K. R. Rusimova, **D. C. Hooper**, H.-H. Jeong, F. Pradaux-Caggiano, T. Verbiest, D. Carbery, P. Fischer, and V. K. Valev, "*First observation of optical activity in hyper-Rayleigh scattering*", Physical Review X **9**, 011024 (2019).

[3] A. Webera, **D. C. Hooperb**, M. Jakob, V. K. Valev, A. Kartouziana, and U. Heiza, "*Circular dichroism & isotropy - polarity reversal of ellipticity in molecular films of 1,1'-bi-2-naphtol*", ChemPhysChem **20**, 62-69 (2018).

[4] J. T. Collins, **D. C. Hooper**, A. G. Mark, C. Kuppe, and V. K. Valev, "*Second-Harmonic Generation Optical Rotation Solely Attributable to Chirality in Plasmonic Metasurfaces*", ACS Nano **12**, 5445-5451 (2018).

[5] J. T. Collins, C. Kuppe, **D. C. Hooper**, C. Sibilia, M. Centini, and V. K. Valev, "*Chirality and Chiroptical Effects in Metal Nanostructures: Fundamentals and Current Trends*", Advanced Optical Materials **5**, 1700182 (2017).

[6] **D. C. Hooper**, A. G. Mark, C. Kuppe, J. T. Collins, P. Fischer, and V. K. Valev, "*Strong Anisotropies Affect Nonlinear Chiral Metamaterials*", Advanced Materials **29**, 1605110 (2017).

[7] A. Belardini, M. Centini, G. Leahu, **D. C. Hooper**, R. Li Voti, E. Fazio, J. W. Haus, A. Sarangan, V. K. Valev, and C. Sibilia,"*Chiral light intrinsically couples to extrinsic/pseudo-chiral metasurfaces made of tilted gold nanowires*" Science Reports **6**, 31796 (2016).

[8] A. Belardini, M. Centini, G. Leahu, R. Li Voti, E. Fazio, C. Sibilia, J. W. Haus, A. Sarangan, **D. C. Hooper**, and V. K. Valev, "*Chiral Optical Response of Self-Assembled Plasmonic Metasurface Investigated by Linear and Nonlinear Detection*

Schemes", in 18th Italian National Conference on Photonic Technologies (Fotonica 2016), 31 (2016).

[9] A. Belardini, G. Leahu, M. Centini, R. Li Voti, E. Fazio, C. Sibilia, J. W. Haus, A. Sarangan, **D. C. Hooper**, and V. K. Valev, "*Effective chiral behavior on self-assembled tilted gold nanowires metasurface by means of linear and nonlinear optical techniques*", Proc. SPIE 9894, Nonlinear Optics and its Applications IV, 98941V (2016).

Contents

Chapter 1

Overview and structure

1.1 Introduction

The laser was first demonstrated by Maiman in 1960 using a Ruby pumped by a flash lamp.[1] Now, lasers are ubiquitous in everyday life with applications ranging from medical, such as eye surgery; industrial, cutting and welding, barcode scanners, found at checkouts. Lasers can also be found in homes, reading disk media, they can even fit into our pockets as laser pointers. The invention of the laser also made a tremendous impact on science; for example, soon after the invention of the laser a new field of research was born, nonlinear optics. With the advent of the laser, scientists had access to high intensity, coherent and monochromatic source of light with which to study the optical properties of materials. Using the high-intensity light provided by lasers meant that new optical processes could be studied. The first nonlinear optical process was demonstrated by Franken et al. in 1961 where crystalline quartz was illuminated with a pulsed ruby laser at 694.3 nm and light with a wavelength of approximately 347.2 nm was observed, second harmonic generation (SHG) had been shown.[2] Famously, the data point showing the SHG was removed from the image before publication as it was assumed to be an error in the figure. Each leap in higher available laser power results in new applications involving nonlinear optics. For example, femtosecond pulsed laser systems are found in commercially available multiphoton microscopy systems. These lasers provide high peak powers at wavelengths which are not strongly absorbed by living tissues. The high peak

powers result in multiphoton processes taking place inside the tissue, light from these processes then forms an image. This method of imaging is advantageous as biological systems experience reduced phototoxicity. Nowadays nonlinear optical processes have found applications in optical parametric oscillators, diode-pumped solid-state lasers, and could be used in quantum computing communication schemes. A new and exciting area of research in nonlinear optics is currently unfolding in the field of plasmonics and nanophotonics.

Plasmonics can be traced back to Wood's observations on the transmission of light through metallic gratings. Wood found that the diffracted transmission of certain wavelengths was greatly diminished.[3] He referred to these drops in transmission as anomalies, importantly he discovered that these anomalies occurred with P-polarised light (electric field vector perpendicular to the length of the grating ruling) and anomalies would spectrally shift with a change in the angle of incidence. In 1907, Lord Rayleigh provided the first explanation for these diffraction anomalies.[4][5] Rayleigh described the anomalies has a result of light being diffracted in the plane of the array. The explanation provided by Rayleigh was based purely on geometrical arguments and did not fully agree with Wood's results. Further investigations found that the anomalies were dependent on the metal used to make the grating, something which could not be accounted for by Rayleigh's explanation. It was not until 1941 that Fano was able to produce a satisfactory solution to Wood's anomalies by proposing the idea of surface waves on the gratings, which we now know to be surface plasmon polaritons.[6]

The modern revitalisation of plasmonics was, in part, sparked in 1998 by Ebbesen et al. and the observation of extraordinary transmission of light through subwavelength holes in an optically thick metal film.[7] Surprisingly, it was found that the holes transmitted more light than expected. This lead to a transmission efficiency much greater than previously thought possible.[8] Extraordinary optical transmission can be partially explained by surface plasmon polaritons.[9] The ability to use plasmons to route and control light caused much excitement because of the prospect of subwavelength optics.[10]

The potential to control light at the nanoscale is also a driving force behind research into metamaterials. By manipulating light on subwavelength scales materials can be engineered with bespoke electromagnetic behaviours, such materials are metamaterials. The

origins of metamaterials research began with negative refractive index. In 1968 Victor Veselago published how it is possible for a fictitious material to possess simultaneously negative permittivity and permeability, which would result in a negative refractive index.[11] In 2000 negative refractive index was rediscovered by Sir John Pendry when he also explained how a slab of material with negative refractive index could lead to perfect lensing.[12] Shortly after Pendry's publications, Shelby et al. demonstrated a material showing negative refractive index for a band of microwave frequencies.[13] Negative refractive index and the idea of combining subwavelength elements to control the behaviour of light lead to the field of metamaterials which has given rise to new fields of study such as, transformation optics,[14] cloaking,[15] and epsilon near zero materials,[16], to name a few.

Metamaterials and plasmonics are now being utilised in the study of nonlinear optics.[17] Just as the advent of the laser provided access to high power optical beams that paved the way for observing second harmonic generation; plasmons give rise to enhanced electric fields at the surfaces of metals which boost nonlinear optical processes. Combining the utility of plasmons with the philosophy of engineered electromagnetic responses, inspired by metamaterials, presents new opportunities in controlling light. Nonlinear nanophotonics promises to extend our command of light through the control of its frequency.

1.2 Thesis structure

This thesis presents second harmonic generation studies from two families of nanophotonic systems. Chapter 2 delves into the first central theme of this thesis, nonlinear optics in particular second harmonic generation. Chapter 3 explores the second central theme, plasmonics and nanophotonics. This chapter deals with how light interacts with the free electrons of a metal and the different types of plasmons. In particular, the localised surface plasmon resonance is discussed, as they are integral to enhancing nonlinear optical processes in metallic nanostructures. Chapter 4 discusses the main experimental techniques used to investigate the nonlinear optical properties of the nanophotonic systems under study. Importantly, it covers the gated photon counting detection scheme used to measure

SHG.

The results of investigations on nanohelix metasurface are presented in Chapter 5. This body of work focuses on how anisotropy affects the nonlinear chiroptical response of an artificial material. Three sets of nanohelices were studied and the effects of changing their geometrical parameters analysed. In Chapter 6 the enhancement of SHG by surface lattice resonances is presented. SHG spectroscopy was performed on arrays of plasmonic nanoparticle that support surface lattice resonances. It is shown that the SHG signal is greatly increased (up to 450 times) by surface lattice resonances. The sensitivity of the SHG enhancement is demonstrated by varying the parameters that determine the surface lattice resonance, namely: fundamental wavelength, angle of incidence, nanoparticle material and lattice spacing of the arrays. An enhancement of SHG attributed to higher-order multipoles is also identified. Furthermore, arrays of ferromagnetic nanoparticles are investigated as are arrays that support hybrid-quadrupole lattice modes. Finally, in Chapter 7 the work is summarised and the direction of future work is discussed.

Chapter 2

Nonlinear Optics

This chapter serves as an introduction to nonlinear optics and in particular to second harmonic generation (SHG) which is one of the unifying themes of this thesis. The aim of this chapter is to provide the reader with a solid foundation of knowledge on SHG so that they can follow the discussions and analyses presented in later chapters. For the interested reader there are many good books on nonlinear optics. The books which I have found most useful are, Boyd[18], Powers[19], Shen[20], Butcher & Cotter[21] and Verbiest[22].

2.1 Linear harmonic oscillator

The linear optical properties of dielectrics can be described by electrons held in a potential well with a quadratic shape. This model assumes that any external driving force is sufficiently weak enough that the restoring force on the perturbed electron can be described by a quadratic function. The potential energy of an electron displaced from equilibrium, at $x = 0$, is given by,

$$U = \frac{1}{2} m\omega_0^2 x^2, \tag{2.1}$$

where m is the mass of the electron, ω_0 is the characteristic angular frequency of the undamped system, and x is the electron displacement from equilibrium. The restoring force on the displaced electron is characterised by,

$$\mathbf{F}_{\text{restoring}} = -\nabla U = -m\omega_0^2 x. \tag{2.2}$$

Equation 2.2 can be identified as Hooke's law, where $m\omega_0^2$ plays the role of the spring constant. When the electron is driven by an external electric field, its equation of motion can be written as,

$$m\frac{\mathrm{d}^2x}{\mathrm{d}t^2} + m\gamma\frac{\mathrm{d}x}{\mathrm{d}t} + m\omega_0^2 x = -eE. \tag{2.3}$$

In Equation 2.3, the first term on the left-hand side is the force acting on the electron from Newton's second law, the second term represents the damping forces experienced by the electron, where γ is a phenomenological damping rate, the third term is the restoring force given in Equation 2.2. On the right-hand side of the equation is the force exerted on the electron of charge $-\mathtt{e}$ by an external electric field of amplitude E. If we consider an electric field oscillating at angular frequency ω, $E(t) = E_0\mathrm{e}^{-i\omega t}$, where E_0 is the electric field amplitude, then a solution for the electron displacement can be found in the form of, $x(t) = x_0\mathrm{e}^{-i\omega t}$, where phase information is incorporated into the complex amplitude x_0. Substituting our solution for x into Equation 2.3 we can solve for x_0 to find that,

$$x_0 = \frac{-eE_0}{m(\omega_0^2 - \omega^2 - i\gamma\omega)}. \tag{2.4}$$

In real materials, the electron resides in the potential well of its positively charged parent ion. The displacement of the electron away from its parent ion creates an electric-dipole moment, which is defined as, $\mathbf{p} = q\mathbf{d}$, where q is the charge of each particle, and $\mathbf{d}$ is the vector separation between the two charges. The overall polarisation of a material is given by $\mathbf{P} = N\mathbf{p}$, where N is the number density of electric-dipole moments. The polarisation can then be expressed in terms of the electron displacement to give,

$$P = \frac{Ne^2E_0}{m(\omega_0^2 - \omega^2 - i\gamma\omega)}. \tag{2.5}$$

For linear materials, the dependence of the polarisation on applied electric field can also be expressed as, $P = \varepsilon_0\chi E$, where ε_0 is the vacuum permittivity, and χ is the linear electric susceptibility of the medium. Using this relation we can write the linear electric susceptibility in terms of the electron's displacement in its potential well caused by the

external field,

$$\chi = \frac{Ne^2}{\varepsilon_0 m(\omega_0^2 - \omega^2 - i\gamma\omega)}. \tag{2.6}$$

2.2 Anharmonic oscillator

The potential well of an electron in a dielectric can be better approximated by including higher-order terms such that the potential takes the form:

$$U = \frac{1}{2}m\omega_0^2 x^2 + \frac{1}{3}amx^3 + \frac{1}{4}bmx^4 + \cdots, \tag{2.7}$$

where a and b are expansion coefficients. The restoring force on the electron is now given by,

$$\mathbf{F}_{\text{restoring}} = -m\omega_0^2 x - amx^2 - bmx^3 + \cdots, \tag{2.8}$$

leading to a new equation of motion for the electron:

$$\frac{\mathrm{d}^2x}{\mathrm{d}t^2} + \gamma\frac{\mathrm{d}x}{\mathrm{d}t} + \omega_0^2 x + ax^2 + bx^3 = -\frac{eE}{m}. \tag{2.9}$$

If the displacement is small then it can be expanded as a power series, $x = x^{(1)} + x^{(2)} + x^{(3)} + \cdots$. Substituting this expansion into Equation 2.9 and equating higher-order terms we arrive at,

$$\frac{\mathrm{d}^2x^{(1)}}{\mathrm{d}t^2} + \gamma\frac{\mathrm{d}x^{(1)}}{\mathrm{d}t} + \omega_0^2 x^{(1)} = -\frac{eE}{m}, \tag{2.10}$$

$$\frac{\mathrm{d}^2x^{(2)}}{\mathrm{d}t^2} + \gamma\frac{\mathrm{d}x^{(2)}}{\mathrm{d}t} + \omega_0^2 x^{(2)} + a(x^{(1)})^2 = 0, \tag{2.11}$$

$$\frac{\mathrm{d}^2x^{(3)}}{\mathrm{d}t^2} + \gamma\frac{\mathrm{d}x^{(3)}}{\mathrm{d}t} + \omega_0^2 x^{(3)} + 2ax^{(1)}x^{(2)} + b(x^{(1)})^3 = 0. \tag{2.12}$$

To solve for the higher order terms in x the solution to the lowest order equation must be found first, as in Section 2.1. The solution for the lowest order displacement is then used to solve the next order equation, and so on.

As we wish to see how nonlinear terms give rise to frequency mixing we examine the case where the driving electric field consists of two fields at angular frequencies ω_1, and

ω_2,

$$E(t)_{\text{total}} = E_{01}\mathrm{e}^{-i\omega_1 t} + E_{02}\mathrm{e}^{-i\omega_2 t}. \tag{2.13}$$

The electron displacement for the lowest order equation of motion is then,

$$x^{(1)} = x_{01}^{(1)}\mathrm{e}^{-i\omega_1 t} + x_{02}^{(1)}\mathrm{e}^{-i\omega_2 t}, \tag{2.14}$$

where $x_{01}^{(1)}$ and $x_{02}^{(1)}$ are complex amplitudes in the form of Equation 2.4. We now substitute Equation 2.14, the linear displacement, into Equation 2.11, the second-order equation of motion, to arrive at:

$$\frac{\mathrm{d}^2x^{(2)}}{\mathrm{d}t^2} + \gamma\frac{\mathrm{d}x^{(2)}}{\mathrm{d}t} + \omega_0^2 x^{(2)} + a\left(x_{01}^{(1)}\mathrm{e}^{-i\omega_1 t} + x_{02}^{(1)}\mathrm{e}^{-i\omega_2 t}\right)^2 = 0. \tag{2.15}$$

Expanding the square of the linear displacement in Equation 2.15 leads to terms oscillating at different frequencies:

$$x_{01}^2\mathrm{e}^{-i2\omega_1 t} + \text{c.c.} \qquad \text{Second harmonic of } \omega_1 \tag{2.16}$$

$$x_{02}^2\mathrm{e}^{-i2\omega_2 t} + \text{c.c.} \qquad \text{Second harmonic of } \omega_2 \tag{2.17}$$

$$2x_{01}x_{02}\mathrm{e}^{-i(\omega_1+\omega_2)t} + \text{c.c.} \qquad \text{Sum frequency of } \omega_1 + \omega_2 \tag{2.18}$$

$$2x_{01}x_{02}^*\mathrm{e}^{-i(\omega_1-\omega_2)t} + \text{c.c.} \qquad \text{Difference frequency of } \omega_1 - \omega_2 \tag{2.19}$$

$$2x_{01}x_{01}^* + 2x_{02}x_{02}^* \qquad \text{Optical rectification} \tag{2.20}$$

where each term gives rise to a different nonlinear optical process. The work presented in this thesis is concerned with second harmonic generation and therefore we solve the second-order displacement associated with Equation 2.16 to find,

$$x^{(2)}(2\omega_1) = \frac{-ax_{01}^2}{\omega_0^2 - i2\omega_1\gamma - 4\omega_1^2}. \tag{2.21}$$

Then, by substituting the solution for x_{01} given in Equation 2.14, and introducing the term $D(\omega) = (\omega_0^2 - i\omega\gamma - \omega^2)$, we can now define a susceptibility for the second harmonic at ω_1,

$$\chi^{(2)}(2\omega_1) = \frac{Nae^3}{\varepsilon_0 m^2 D(2\omega_1)D(\omega_1)^2}, \tag{2.22}$$

which enables us to write the nonlinear polarisation at the second harmonic,

$$P(2\omega_1) = \varepsilon_0 \chi^{(2)}(2\omega_1) E(\omega_1) E(\omega_1). \tag{2.23}$$

2.3 Nonlinear polarisation

In Section 2.1 we saw that, in the linear optical regime the induced polarisation of a material is linearly dependent on the incident electric field and can be expressed as,

$$\mathbf{P}(\omega) = \varepsilon_0 \chi(\omega) \cdot \mathbf{E}(\omega), \tag{2.24}$$

where $\mathbf{E}(\omega)$ is the electric field strength at angular frequency ω, and $\chi(\omega)$ is the linear electric susceptibility.

The motivation for focusing on polarisation stems from the fact that it is through a material's polarisation that an electric field can exchange energy with a medium. To illustrate this we examine the wave equation in medium without free currents:

$$\nabla \times \nabla \times \mathbf{E} = -\mu_0 \frac{\partial^2 \mathbf{D}}{\partial t^2}, \tag{2.25}$$

where μ_0 is the permeability of free space and $\mathbf{D}$ is the electric flux density. Substituting in the constitutive relation, $\mathbf{D} = \varepsilon_0 \mathbf{E} + \mathbf{P}$, leads to,

$$\nabla \times \nabla \times \mathbf{E} = -\mu_0 \left(\varepsilon_0 \frac{\partial^2 \mathbf{E}}{\partial t^2} + \frac{\partial^2 \mathbf{P}}{\partial t^2} \right), \tag{2.26}$$

where we can see that the material polarisation plays an essential role in the wave equation. The function of the polarisation is eloquently presented in §2.1.3 of Powers, where Poynting's theorem is presented as:[19]

$$\oint \mathbf{S} \cdot \mathrm{d}\mathbf{a} = -\left[\frac{\mathrm{d}W_{\mathrm{mech}}}{\mathrm{d}t} + \frac{\mathrm{d}}{\mathrm{d}t} \int \mathcal{U} \mathrm{d}V + \int \mathbf{E} \cdot \frac{\partial \mathbf{P}}{\partial t} \mathrm{d}V \right], \tag{2.27}$$

where $\mathbf{S}$ is the Poynting vector, $\mathbf{a}$ is the area of the closed surface of the integral, W_{mech} is the mechanical work done, $\mathcal{U}$ is the energy density stored in the field, and V is the enclosed

volume. Powers explains how Equation 2.27 describes the flow of power out of a closed surface, where the final term on the right-hand side shows the rate of work done on the medium by the electromagnetic field via the material's polarisation. Hence, demonstrating the key role of the polarisation in exchanging energy between electromagnetic fields and a medium, which allows light of different frequencies to interact via nonlinear optical processes.

In Section 2.1 we saw how the expression for polarisation given in Equation 2.24 describes a system where the restoring force on the charges is linear, and hence the system can be treated as a linear harmonic oscillator. Then, in Section 2.2, higher-order terms were included in the restoring force, which combined with a power series displacement of the charges, allows for frequency mixing. The anharmonic oscillator model describes when incident electric fields are strong enough to drive charges beyond the regime of a linear restoring force meaning the polarisation can be expanded into a power series,

$$\mathbf{P}(t) = \varepsilon_0 \chi^{(1)} \mathbf{E}(t) + \varepsilon_0 \chi^{(2)} \mathbf{E}^2(t) + \varepsilon_0 \chi^{(3)} \mathbf{E}^3(t) + ..., \tag{2.28}$$

here $\mathbf{E}(t)$ is the incident electric field and $\chi^{(\mathrm{n})}$ is the susceptibility of the n^{th} order, for example $\chi^{(1)}$ is the linear susceptibility and $\chi^{(2)}$ is the second order susceptibility, and so on. It can be convenient to rewrite Equation 2.28 in summation notation as,

$$P_{\mathrm{i}}(t) = \varepsilon_0 \chi^{(1)}_{\mathrm{ij}} E_{\mathrm{j}}(t) + \varepsilon_0 \chi^{(2)}_{\mathrm{ijk}} E_{\mathrm{j}}(t) E_{\mathrm{k}}(t) + \varepsilon_0 \chi^{(3)}_{\mathrm{ijkl}} E_{\mathrm{j}}(t) E_{\mathrm{k}}(t) E_{\mathrm{l}}(t) + ..., \tag{2.29}$$

where summation over repeated indices is implied, and the indices can take any of the Cartesian directions x, y, z. In this form it is now easily seen that the total material polarisation can depend on more than one input field and their polarisations. It can also be seen that the electric susceptibilities are tensors of rank $\mathrm{n} + 1$. Each higher order contribution to the polarisation gives rise to various nonlinear optical processes, as seen in Equations 2.16 - 2.20. However we focus our attention on one specific process, second harmonic generation (SHG).

Second harmonic generation is the nonlinear optical process whereby two input photons of the same energy annihilate to create a single photon with twice the energy. The source

of second harmonic generation is the second order polarisation In the electric dipole approximation, where only dipole contributions are considered, the second order polarisation can be expressed in index notation as,

$$P_{\mathrm{i}}^{(2)}(2\omega) = \varepsilon_0 \chi_{\mathrm{ijk}}^{(2)} E_{\mathrm{j}}(\omega) E_{\mathrm{k}}(\omega). \tag{2.30}$$

Here, $\chi_{\mathrm{ijk}}^{(2)}$ is a 3^{rd} rank tensor containing 27 elements, which are generally complex. The first index of $\chi^{(2)}$ denotes the direction of the polarisation while the last two indices refer to the polarisation direction of the two input fields. For examples $P_x^{(2)}(2\omega) = \chi_{xyx}^{(2)} E_y(\omega) E_x(\omega)$ gives the second harmonic polarisation in the x direction due to input fields polarised along the y and x directions.

2.4 Nonlinear susceptibility

The second order nonlinear electric susceptibility tensor can be written as a matrix in the form,

$$\chi_{\mathrm{ijk}}^{(2)} = \begin{bmatrix} \chi_{xxx} & \chi_{xyy} & \chi_{xzz} & \chi_{xyz} & \chi_{xzy} & \chi_{xzx} & \chi_{xxz} & \chi_{xxy} & \chi_{xyx} \\ \chi_{yxx} & \chi_{yyy} & \chi_{yzz} & \chi_{yyz} & \chi_{yzy} & \chi_{yzx} & \chi_{yxz} & \chi_{yxy} & \chi_{yyx} \\ \chi_{zxx} & \chi_{zyy} & \chi_{zzz} & \chi_{zyz} & \chi_{zzy} & \chi_{zzx} & \chi_{zxz} & \chi_{zxy} & \chi_{zyx} \end{bmatrix}, \tag{2.31}$$

where the superscript (2) has been omitted for individual tensor elements, as all discussion from now on will be concerned with the second order susceptibility. In general, each tensor element is complex with the imaginary part representing relative phase information. Nonlinear processes that do not excite an electronic resonance occur via virtual levels and take place on femtosecond to sub-femtosecond time scales. In this nonresonant scheme the imaginary parts of the tensor elements can be regarded as negligible because the nonlinear process can be considered instantaneous, negating the need for phase information.

It would be preferable to reduce the number of elements in the susceptibility tensor in order to make it more tractable. Fortunately, tensor components can be eliminated by symmetry and permutation relations.

2.4.1 Reducing $\chi^{(2)}$ via permutation

The number of independent tensor elements in $\chi^{(2)}$ can be reduced via permutation. In SHG the two annihilated photons have the same energy, meaning that it does not matter in which order the electric fields are written in Equation 2.30. This indistinguishability means that the indices j and k of the susceptibility can be freely interchanged. Therefore, tensor elements with different permutations of the last two indices become degenerate. For example, χ_{xyx} is equivalent to χ_{xxy} because they share the same last two indices. This permutation relation allows the SHG susceptibility to be written as,

$$\chi^{\mathrm{SHG}} = \begin{pmatrix} xxx & xyy & xzz & xyz & xxz & xxy \\ yxx & yyy & yzz & yyz & yxz & yxy \\ zxx & zyy & zzz & zyz & zxz & zxy \end{pmatrix}, \tag{2.32}$$

where the term χ has been dropped for readability.

2.4.2 Reducing $\chi^{(2)}$ via symmetry

According to Neumann's principle the symmetry properties of a crystal must also apply to its physical properties.[23] Applying the symmetry operations, under which a medium is invariant, to the susceptibility tensor reduces the number of independent elements. For the second order susceptibility tensor of rank three this is achieved with the following operation:[19]

$$\chi^{(2)'}_{\mathrm{ijk}} = R_{\mathrm{i}\alpha} R_{\mathrm{j}\beta} R_{\mathrm{k}\gamma} \chi^{(2)}_{\alpha\beta\gamma}, \tag{2.33}$$

where R is a transformation matrix, $\chi_{\alpha\beta\gamma}$ is the untransformed tensor and $\chi^{(2)'}_{\mathrm{ijk}}$ is the tensor after transformation. It is now straight forward to demonstrate one of the key symmetry properties of SHG, it is forbidden in centrosymmetric systems. In other words, the system must break inversion symmetry for SHG to occur. The inversion operation is given by,

$$R^{\mathrm{inv}}_{\mathrm{ij}} = \begin{bmatrix} -1 & 0 & 0 \\ 0 & -1 & 0 \\ 0 & 0 & -1 \end{bmatrix}, \tag{2.34}$$

which represents the transformations of:

$$x \to -x,$$

$$y \to -y,$$

$$z \to -z.$$

We note that this matrix is the negative of the Kronecker delta, $-\delta_{\mathrm{ij}}$, which takes the values:

$$\delta_{\mathrm{ij}} = \begin{cases} 0 & \text{if i} \neq \text{j}, \\ 1 & \text{if i} = \text{j}. \end{cases} \tag{2.35}$$

Applying the inversion operation in Equation 2.34 to $\chi^{(2)}_{\alpha\beta\gamma}$ we find that,

$$\chi^{(2)'}_{\mathrm{ijk}} = (-\delta_{\mathrm{i}\alpha})(-\delta_{\mathrm{j}\beta})(-\delta_{\mathrm{k}\gamma})\chi^{(2)}_{\alpha\beta\gamma} = -\chi^{(2)}_{\mathrm{ijk}}. \tag{2.36}$$

For a system to posses a symmetry it must be left unchanged after undergoing the relevant transformation. In the case of inversion we find that $\chi^{(2)}_{\mathrm{ijk}} = -\chi^{(2)}_{\mathrm{ijk}}$, which can only hold true if every tensor element is zero. Hence, it must be that $\chi^{(2)}_{\mathrm{ijk}} = 0$, thereby demonstrating that SHG cannot occur in centrosymmetric systems. In fact, this result is true for any even-order process.

Another way to see this is to consider the higher order terms of the potential given in Equation 2.7. For a centrosymmetric material the electrons reside in a potential that is given by an even function. That is to say that $U(x) = U(-x)$, which requires the expansion coefficient a in Equation 2.7 to equal zero. Therefore, the quadratic term of the restoring force in Equation 2.8 is zero and second order processes cannot occur.

While the application of inversion symmetry to $\chi^{(2)}$ yields a trivial solution, other symmetries act to yield tensors with a reduced number of elements. Next, we consider the symmetry operation of rotation, as shown in Figure 2.1 with the example of a 4-fold rotation. A medium possesses 4-fold symmetry (C_4) when it is unchanged by a rotation of 90° around a chosen axis. In the case of rotation around the z-axis the transformation

matrix is given by,

$$R_{\mathrm{ij}}^{\mathrm{rotation}}\left(\theta_z = \frac{\pi}{2}\right) = \begin{bmatrix} 0 & -1 & 0 \\ 1 & 0 & 0 \\ 0 & 0 & 1 \end{bmatrix}. \tag{2.37}$$

To determine the tensor elements that survive this operation the original and transformed susceptibilities are compared. In order to avoid having to perform the entire calculation given in Equation 2.33, a method known as direct inspection can be used to determine the surviving tensor elements instead. Direct inspection works by operating on each index of a tensor element. For 4-fold rotational symmetry the operations are:

$$x \to -y,$$

$$y \to x,$$

$$z \to z.$$

The operations are then applied directly to the indices of a tensor element, such as $xxx \to -yyy$, then applying the transformation again, $-yyy \to -xxx$. Here we see that the tensor element $xxx \to -xxx$, meaning it must vanish, because there cannot be inversion symmetry. The surviving elements and their relations can be found by applying these operations to the other tensor elements. For C_4 symmetry the resulting susceptibility is given by,

$$\chi_{C_4}^{(2)} = \begin{pmatrix} 0 & 0 & 0 & xyz & xxz & 0 \\ 0 & 0 & 0 & xxz & yxz & 0 \\ zxx & zxx & zzz & 0 & 0 & zyx \end{pmatrix}. \tag{2.38}$$

We now consider mirror symmetry, which is important for Chapter 5 which deals with chiral materials. Mirror symmetry is central to the idea of chirality because objects with no mirror symmetry are said to be chiral, while objects with mirror symmetry are deemed achiral. The operation for a mirror plane in the $x - z$ plane is given by,

$$R_{\mathrm{ij}}^{\sigma_{xz}} = \begin{bmatrix} 1 & 0 & 0 \\ 0 & -1 & 0 \\ 0 & 0 & 1 \end{bmatrix}, \tag{2.39}$$

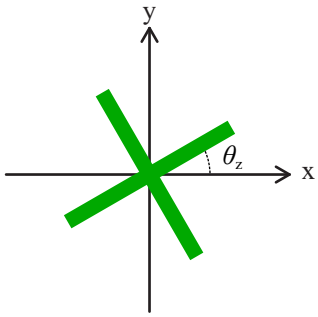

Figure 2.1: An object with four-fold rotational symmetry undergoing rotation in the $x-y$ plane.

where the superscript σ_{xz} denotes the mirror plane in the $x-y$ plane. From Equation 2.39, the transformations for direct inspection are

$$x \to x,$$

$$y \to -y,$$

$$z \to z.$$

A cursory analysis leads to the rule that tensor elements with an odd number of y indices must vanish. Applying this rule yields the following susceptibility tensor,

$$\chi^{(2)}_{\sigma_{xz}} = \begin{pmatrix} xxx & xyy & xzz & 0 & xxz & 0 \\ 0 & 0 & 0 & yyz & 0 & yxy \\ zxx & zyy & zzz & 0 & zxz & 0 \end{pmatrix}. \tag{2.40}$$

Later, we will use the application of mirror symmetry to identify chiral tensor components in Chapter 5.

2.5 Direction of SHG radiation

The electric field radiated by the second harmonic polarisation due to electric dipoles can be calculated using,[24]

$$\mathbf{E}(2\omega) \approx [\mathbf{n} \times \mathbf{P}(2\omega)] \times \mathbf{n}, \tag{2.41}$$

where $\mathbf{E}(2\omega)$ is the electric field vector of the second harmonic, and $\mathbf{n}$ is the unit vector in the direction of observation. Using Equation 2.30 expanded in matrix form and using the contracted notion for χ^{SHG} in Equation 2.32 the second harmonic polarisation can be calculated,

$$\begin{pmatrix} P_x(2\omega) \\ P_y(2\omega) \\ P_z(2\omega) \end{pmatrix} = \begin{pmatrix} xxx & xyy & xzz & xyz & xxz & xxy \\ yxx & yyy & yyz & yyz & yxz & yxy \\ zxx & zyy & zzz & zyz & zxz & zxy \end{pmatrix} \begin{pmatrix} E_x(\omega)^2 \\ E_y(\omega)^2 \\ E_z(\omega)^2 \\ 2E_y(\omega)E_z(\omega) \\ 2E_x(\omega)E_z(\omega) \\ 2E_x(\omega)E_y(\omega) \end{pmatrix}. \tag{2.42}$$

Here, the susceptibility tensor can be changed to represent the symmetry of the medium. Also note that the factor of two for some of the incident electric fields. This factor arises due to a need to double count degenerate tensor elements not explicitly written because of permutation. To calculate the second harmonic field we define the direction unit vector,

$$\hat{\mathbf{n}}_{\mathrm{T}}^{\mathrm{R}} = \sin\theta\hat{\mathbf{x}} \pm \cos\theta\hat{\mathbf{z}}, \tag{2.43}$$

where the superscript R refers to reflection and the subscript T denotes transmission, and θ is the angle of incidence of the fundamental beam. Performing the first cross product in Equation 2.41 gives,

$$\begin{aligned} \hat{\mathbf{n}}_T^R \times \mathbf{P}(2\omega) &= \begin{pmatrix} \sin\theta \\ 0 \\ \pm\cos\theta \end{pmatrix} \times \begin{pmatrix} P_x \\ P_y \\ P_z \end{pmatrix} = \begin{vmatrix} \hat{\mathbf{i}} & \hat{\mathbf{j}} & \hat{\mathbf{k}} \\ \sin\theta & 0 & \pm\cos\theta \\ P_x & P_y & P_z \end{vmatrix} \\ &= (\mp P_y\cos\theta)\hat{\mathbf{i}} + (\pm P_x\cos\theta - P_z\sin\theta)\hat{\mathbf{j}} + (P_y\sin\theta)\hat{\mathbf{k}}, \end{aligned} \tag{2.44}$$

Continuing on from Equation 2.44 we obtain the full expression of both cross products in Equation 2.41:

$$\begin{aligned}\mathbf{E}(2\omega) = (\hat{\mathbf{n}}_T^R \times \mathbf{P}(2\omega)) \times \hat{\mathbf{n}}_T^R &= \begin{vmatrix} \hat{\mathbf{i}} & \hat{\mathbf{j}} & \hat{\mathbf{k}} \\ (\mp P_y \cos\theta) & (\pm P_x \cos\theta - P_z \sin\theta) & (P_y \sin\theta) \\ \sin\theta & 0 & \pm\cos\theta \end{vmatrix} \\ &= (P_x \cos^2\theta \mp P_z \sin\theta\cos\theta)\hat{\mathbf{i}} - (-P_y \cos^2\theta - P_y \sin^2\theta)\hat{\mathbf{j}} \\ &+ (\mp P_x \sin\theta\cos\theta + P_z \sin^2\theta)\hat{\mathbf{k}}\end{aligned} \tag{2.45}$$

The second harmonic electric field can now be calculated for a medium of any known symmetry as long as the incident electric fields are known and decomposed into the frame of reference of the medium. The intensity of the SHG is then found using the relation,

$$I(2\omega) \approx |\mathbf{E}(2\omega)|^2 . \tag{2.46}$$

2.6 Multipolar second harmonic generation

In Equation 2.30 the only source of SHG comes from dipole contributions, in this section we examine contributions from higher-order and multipole terms. A more general expression for the second harmonic polarisation obtained by a multipole expansion is given by,[25]

$$\mathbf{P}_{\text{eff}}^{(2)}(2\omega) = \mathbf{P}^{(2)}(2\omega) - \nabla \cdot \overleftrightarrow{Q}^{(2)}(2\omega) + \frac{c}{i2\omega}\nabla \times \mathbf{M}^{(2)}(2\omega), \tag{2.47}$$

where $\mathbf{P}$, $\overleftrightarrow{Q}$, and $\mathbf{M}$ denote the electric-dipole polarisation, electric-quadrupole polarisation, and magnetisation at the second harmonic, respectively. Note that while the electric-dipole polarisation and magnetisation are vectors and are hence bold typeface, the electric-quadrupole polarisation is a tensor and is denoted by a double ended arrow hat. This notation is used to here to signifiy a tensor while it is omitted elsewhere because either the tensor can be recognised by indices or context. The electric dipole term can be further expanded with a Taylor expansion of the electric field,[26]

$$\mathbf{EE} = \mathbf{EE} + (\nabla\mathbf{E})\mathbf{E} + \mathbf{E}(\nabla\mathbf{E}) + \cdots . \tag{2.48}$$

Meaning that the electric dipole term from Equation 2.30 can be rewritten as,

$$P_{\mathrm{i}}^{(2)}(2\omega) = \chi_{\mathrm{ijk}}^{(2\mathrm{D})} E_{\mathrm{j}}(\omega) E_{\mathrm{k}}(\omega) + \chi_{\mathrm{ijkl}}^{(2\mathrm{Q})} E_{\mathrm{j}}(\omega) \nabla_{\mathrm{k}} E_{\mathrm{l}}(\omega), \tag{2.49}$$

where $\chi_{\mathrm{ijk}}^{(2\mathrm{D})}$ is the electric dipole susceptibility seen in Equation 2.30, and $\chi_{\mathrm{ijkl}}^{(2\mathrm{Q})}$ is the bulk quadrupolar susceptibility. This new term acts as a source of SHG at interfaces where the electric fields fall off rapidly giving rise to strong field gradients. It is referred to as a quadrupolar term due to its dependence on field gradients.

In this work most of the samples investigated are primarily fabricated from the noble metals gold and silver. These two metals have a face-centred cubic crystal structure, which is centrosymmetric. Therefore, in the dipole approximation the bulk structure does not contribute to SHG. In other words, the first term in Equation 2.49 vanishes for the metal bulk. We now want to find an expression for the second harmonic polarisation from the bulk, we start with the tensor elements and their relations for $\chi_{\mathrm{ijkl}}^{(2\mathrm{Q})}$:[21]

$$\begin{aligned}
&\chi_{xxxx} = \chi_{yyyy} = \chi_{zzzz}, \\
&\chi_{xxyy} = \chi_{yyxx} = \chi_{yyzz} = \chi_{zzyy} = \chi_{zzxx} = \chi_{xxzz}, \\
&\chi_{xyxy} = \chi_{yxyx} = \chi_{yzyz} = \chi_{zyzy} = \chi_{zxzx} = \chi_{xzxz}, \\
&\chi_{xyyz} = \chi_{yxxy} = \chi_{yzzy} = \chi_{zyyz} = \chi_{zxxz} = \chi_{xzzx}.
\end{aligned} \tag{2.50}$$

These elements are substituted into the second term of Equation 2.49. The following vector identity is then expanded in three stages,

$$\nabla(A \cdot B) = A \times (\nabla \times B) + B \times (\nabla \times A) + (A \cdot \nabla)B + (B \cdot \nabla)A. \tag{2.51}$$

First the cross products are expanded to give:

$$\nabla \times B = (\nabla_y B_z - \nabla_z B_y)\hat{\mathbf{i}} + (\nabla_z B_x - \nabla_x B_z)\hat{\mathbf{j}} + (\nabla_x B_y - \nabla_y B_x)\hat{\mathbf{k}}, \tag{2.52}$$

$$\begin{aligned} A \times (\nabla \times B) = A_y(\nabla_x B_y - \nabla_y B_x) - A_z(\nabla_z B_x - \nabla_x B_z) \\ + A_z(\nabla_y B_z - \nabla_z B_y) - A_x(\nabla_x B_y - \nabla_y B_x) \\ + A_x(\nabla_z B_x - \nabla_x B_z) - A_y(\nabla_y B_z - \nabla_z B_y). \end{aligned} \tag{2.53}$$

Second, the initial dot products are expanded as:

$$\begin{aligned} (A \cdot \nabla)B &= (A_x\nabla_x + A_y\nabla_y + A_z\nabla_z)B \\ &= A_x\nabla_x B_x + A_x\nabla_x B_y + A_x\nabla_x B_z \\ &+ A_y\nabla_y B_x + A_y\nabla_y B_y + A_y\nabla_y B_z \\ &+ A_z\nabla_z B_x + A_y\nabla_y B_y + A_y\nabla_y B_z. \end{aligned} \tag{2.54}$$

Finally, the last dot product is expanded:

$$\begin{aligned} A(\nabla \cdot B) &= A(\nabla_x B_x + \nabla_y B_y + \nabla_z B_z) \\ &= A_x\nabla_x B_x + A_x\nabla_y B_y + A_x\nabla_z B_z \\ &+ A_y\nabla_x B_x + A_y\nabla_y B_y + A_y\nabla_z B_z \\ &+ A_z\nabla_x B_x + A_z\nabla_y B_y + A_z\nabla_z B_z. \end{aligned} \tag{2.55}$$

The terms of the expanded vector identity can be equated with terms found from substituting the elements from Equation 2.50 into Equation 2.49. However, expanding the vector identity causes some tensor elements to appear too often or not at all. Therefore, a final term is needed to compensate for the missing or extra terms:

$$(\chi_{xxxx} - \chi_{xyyx} - \chi_{xxyy} - \chi_{xyxy}) \sum_{\mathrm{i}} E_{\mathrm{i}} \nabla_{\mathrm{i}} E_{\mathrm{i}}. \tag{2.56}$$

Putting these altogether we arrive at a more tangible expression for the material polarisation at the second harmonic due to quadrupolar contributions:[17]

$$\begin{aligned} \mathbf{P}(2\omega) = (\delta - \beta - 2\gamma)(\mathbf{E}(\omega) \cdot \nabla)\mathbf{E}(\omega) + \beta\mathbf{E}(\omega)(\nabla \cdot \mathbf{E}(\omega)) + \gamma\nabla(\mathbf{E}(\omega) \cdot \mathbf{E}(\omega)) \\ + \zeta \sum_{\mathrm{i}} E_{\mathrm{i}}(\omega)\nabla_{\mathrm{i}} E_{\mathrm{i}}(\omega), \end{aligned} \tag{2.57}$$

where δ, β, and γ are phenomenological constants, related to the susceptiblity tensor com-

ponents, that describe the isotropic response of the medium. The first term in Equation 2.57 vanishes if only a single plane wave fundamental is considered. The second term also vanishes because $\nabla \cdot \mathbf{E} = 0$ from Maxwell's equations. The final term represents the anisotropic response of the medium because it is sensitive to the orientation of the crystal axes, for isotropic media $\zeta = 0$ and does not contribute.[27]

2.7 Summary

This chapter on nonlinear optics has covered how a harmonic oscillator can be used to model the linear optical response of a medium. Then, to describe the nonlinear behaviour, the model is extended to an anharmonic oscillator that gives rise to higher-order terms in the electron equation of motion and hence displacement. The second-order equation of motion is then shown to allow frequency mixing which is the basis of nonlinear optical processes.

Particular attention is then paid to the polarisation and how it is through the polarisation that an electromagnetic field can exchange energy with a medium, thus allowing frequency mixing. We then concentrated on the second-order process of second harmonic generation and how its sensitivity to symmetry shapes the susceptibility tensor, $\chi^{(2)}_{\mathrm{ijk}}$. In turn we explored how to retrieve the SHG intensity for a medium of arbitrary symmetry, assuming knowledge of the incident fields and sample symmetry.

Finally, we examined how the dipole approximation of SHG can be extended through a multipole expansion to include contributions from magnetisation and quadrupoles. Furthermore, the dipolar contribution to the polarisation was expanded to include higher-order terms through a Taylor expansion. This expansion allowed us to see how field gradients in the bulk and at interfaces can give rise to SHG in centrosymmetric systems such as the noble metals gold and silver, which are favoured for plasmonic applications.

Chapter 3

Plasmonics and nanophotonics

Plasmon resonances are the coherent oscillations of free electrons in a metal. Strictly speaking, a plasmon itself is a quantum of oscillating plasma; the plasma is formed of the free electrons and the ionic cores of a metal. There exist three main types of plasmons, firstly the bulk, or volume plasmons, which occurs within the metal itself. Second, surface plasmon polaritons (SPP) which arise at the interface between a metal and dielectric. The final, and most relevant to this work, are the localised surface plasmon resonances (LSPR) which emerge due to the geometrical confinement provided by metallic nanoparticles. This chapter presents the three types of plasmons, bulk, surface plasmon polariton, and localised surface plasmon resonance given their importance for understanding the work presented in Chapters 5 and 6.

3.1 Volume plasmons

We start with the wave equation derived from Maxwell's equations in the absence of external sources,

$$\nabla \times \nabla \times \mathbf{E} = -\mu_0 \frac{\partial^2 \mathbf{D}}{\partial t^2}, \tag{3.1}$$

$$\mathbf{k}(\mathbf{k} \cdot \mathbf{E}) - k^2 \mathbf{E} = -\varepsilon(\mathbf{k}, \omega) \frac{\omega^2}{c^2} \mathbf{E}, \tag{3.2}$$

in the time and Fourier domain respectively. Here $\mathbf{E}$ is the electric field vector, μ_0 is the permeability of free space, $\mathbf{D}$ is the displacement field, $\mathbf{k}$ is the wave vector, ω is the angular frequency of the electric field, ε is the dielectric function and, c is the speed of

light. Equation 3.2 has longitudinal wave solutions.

A longitudinal wave has direction of propagation and field displacement in the same direction. Therefore, in the case of a longitudinal wave, we find that $\mathbf{k} \cdot \mathbf{E}$ simply becomes kE and hence the left-hand side of Equation 3.2 becomes zero. A non-trivial solution exists when $\varepsilon(\mathbf{k}, \omega) = 0$. We can see the importance of this solution by examining the constituent relation:

$$\mathbf{D} = \varepsilon_0 \mathbf{E} + \mathbf{P}, \tag{3.3}$$

where $\mathbf{P}$ is the polarisation, which is a measure of how much a medium becomes polarised in response to an electric field, expressed as $\mathbf{P} = \varepsilon_0 \chi \mathbf{E}$. Using this relation between the polarisation and the electric field and that $\varepsilon = 1 + \chi$ allows us to rewrite Equation 3.3 as $\mathbf{D} = \varepsilon_0 \varepsilon \mathbf{E}$. If $\varepsilon = 0$ then $\mathbf{D} = 0$ and therefore the electric field is given by, $\mathbf{E} = -\frac{\mathbf{P}}{\varepsilon_0}$. This situation can arise in a slab of metal where a collective displacement of the free electrons produces a charge density $\sigma = nex$, where n is the electron number density, e is the charge of the electron, and x is the displacement. The charge densities on opposing faces of the metal slab have opposite sign, which causes an electric field $\mathbf{E} = \frac{\sigma}{\varepsilon_0}$. This electric field acts as a restoring force on the displaced electrons, $nm_{\text{eff}}a = -\frac{n^2e^2x}{\varepsilon_0} = F_{\text{restoring}}$, where m_{eff} is the electron's effective mass, and a is acceleration. This force can then be rewritten as an equation of motion for the electron, $\frac{\mathrm{d}^2x}{\mathrm{d}t^2} + \omega_{\text{p}}^2 x = 0$, where $\omega_{\text{p}} = \frac{ne^2}{m_{\text{eff}}\varepsilon_0}$ is the natural frequency of oscillation of the plasma formed by the free electrons, called the plasma frequency. Due to the longitudinal nature of volume plasmons they do not couple to transverse electromagnetic waves.

3.2 Surface plasmon polaritons

Surface plasmon polaritons (SPP) are coherent charge density oscillations at the interface between a metal and a dielectric that are coupled to electromagnetic waves. SPPs can propagate along the surface interface and are therefore sometimes called propagating surface plasmon polaritons. To examine the properties of SPPs we consider the interface between two media, as shown in Figure 3.1. The first medium is located in the region $z > 0$ and possesses a purely real and positive dielectric function ε_2. The second medium

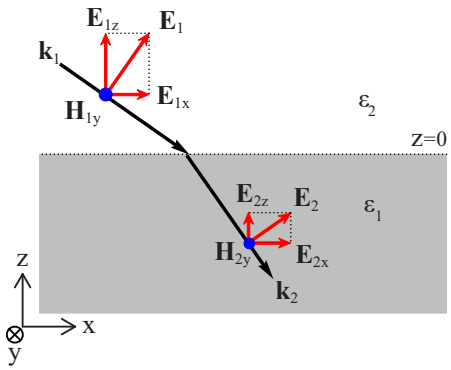

Figure 3.1: An electromagnetic wave incident on the interface between a dielectric and metal.

is located in the region $z < 0$ and has a complex dielectric function ε_1. The interface between the two media is situated at $z = 0$.

We consider a P-polarised electromagnetic wave incident with the interface at an acute angle of incidence. Conservation of the wavevector component in-plane with the interface then allows us to write expressions for the wavevectors on either side of the interface,

$$k_x^2 + k_{1z}^2 = \varepsilon_1 k_0^2, \tag{3.4}$$

$$k_x^2 + k_{2z}^2 = \varepsilon_2 k_0^2, \tag{3.5}$$

where $k_0 = \frac{2\pi}{\lambda}$, λ is the vacuum wavelength, and $k_x = k_{1x} = k_{2x}$. The system is source free and therefore we can use $\nabla \cdot \mathbf{D} = 0$ to impose the conditions:

$$k_x E_{1x} + k_{1z} E_{1z} = 0, \tag{3.6}$$

$$k_x E_{2x} + k_{2z} E_{2z} = 0. \tag{3.7}$$

Furthermore, continuity of the in-plane electric field components leads to the boundary condition,

$$E_{1x} = E_{2x}. \tag{3.8}$$

The perpendicular components of the displacement field $\mathbf{D}$ must also be continuous leading

to a second boundary condition,

$$\varepsilon_1 E_{1z} = \varepsilon_2 E_{2z}. \tag{3.9}$$

Solving this system of equations yields, $k_{2z}\varepsilon_1 - k_{1z}\varepsilon_2 = 0$. We can now find the dispersion relation for the in-plane wavevector,

$$k_x^2 = \frac{\omega^2}{\mathrm{c}^2}\frac{\varepsilon_1\varepsilon_2}{\varepsilon_1 + \varepsilon_2}. \tag{3.10}$$

The out-of-plane wave vector components are,

$$k_{1z}^2 = \frac{\omega^2}{\mathrm{c}^2}\frac{\varepsilon_1^2}{\varepsilon_1 + \varepsilon_2}, \tag{3.11}$$

$$k_{2z}^2 = \frac{\omega^2}{\mathrm{c}^2}\frac{\varepsilon_2^2}{\varepsilon_1 + \varepsilon_2}. \tag{3.12}$$

For k_x to correspond to a propagating solution requires it to be real. Furthermore, for the solution to be bound to the surface requires that the out-of-plane wave vectors k_z to be imaginary. The first condition for k_x to be real is satisfied if the numerator and denominator in Equation 3.10 are both either positive or negative. The second condition that k_z be imaginary in both media occurs when the denominators in Equations 3.11 and 3.12 are negative. These restrictions mean that $\varepsilon_1 + \varepsilon_2 < 0$ which then constrains the condition on k_x such that the numerator in Equation 3.10 must be negative, $\varepsilon_1\varepsilon_2 < 0$. To satisfy these conditions requires one of the dielectric functions to be negative and to have a greater magnitude than the other, $\varepsilon_1 < 0$ and $|\varepsilon_1| > \varepsilon_2$. These conditions on the dielectric functions are satisfied at the interface between a metal and a dielectric. The real part of the dielectric function of metals is generally large and negative in the visible, meaning the interface with a dielectric can support surface plasmon polaritons.

In order to plot the plasmon dispersion we need to find an expression for the dielectric function of a metal as a function of wavelength. The dielectric function of a free electron gas can be written as:[28]

$$\varepsilon(\omega) = 1 - \frac{\omega_p^2}{\omega^2 + i\gamma\omega}, \tag{3.13}$$

where γ represents damping of the free electrons. In te case of negligible damping, γ

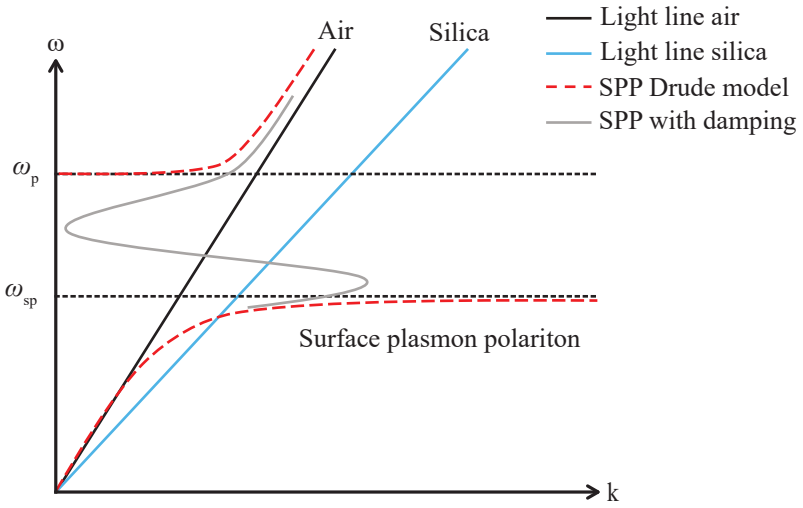

Figure 3.2: Illustrations of the dispersion relations for Drude model of surface plasmon polariton (dashed red line), surface plasmon with damping (solid grey line), Light line in vacuum (solid black line), light line in silica (solid blue line). The labelled dotted lines indicate the plasma frequency and surface plasmon frequency.

vanishes and the dispersion relation reduces to:

$$\varepsilon(\omega) = 1 - \frac{\omega_p^2}{\omega^2}, \tag{3.14}$$

which is known as the Drude model of the dielectric function of a free electron gas. Now we are equipped with our dielectric functions we can proceed to plotting our dispersion relations.

The dispersion relation in Equation 3.10 is shown in Figure 3.2. The solid black line shows the light linein air with the dispersion relation $\omega = ck$. The red dashed line is the dispersion of the surface plasmon polariton in using the Drude model for the dielectric function of a metal. In the Drude model damping is neglected. However, when damping is incorporated into the dielectric function of a metal the plasma dispersion resembles the solid grey line. We can see that the light line and the SPP dispersion curves (with or without damping) do not intersect, meaning that free space radiation cannot excite a SPP. The solid blue line shows the light line in a dielectric such as silica, which has a refractive index $n > 1$, and intersects the plasmon dispersion curves. This means a plasmon can be

excited at the interface between a dielectric, such as silica glass, and a metal.

Various methods and experimental geometries are utilised to momentum match incident light with SPP mode. The most well-known methods are the Kretschmann and Otto configurations, shown in Figures 3.3a and 3.3b respectively. These methods use a prism with relatively high refractive index ($n = \sqrt{\varepsilon}$) to essentially pull the light line down so that the dispersion curves of the light travelling through the prism and the SPP mode intersect. Another method is to fabricate grating structures onto the metal surface, shown in Figure 3.3c. The grating provides lattice momentum so that incident light is momentum matched to the SPP mode, gratings can also be used to scatter SPPs so that they can be detected. The sensitivity of surface plasmons polaritons on their dielectric environment and hence the surrounding refractive index has made them useful for sensing applications.

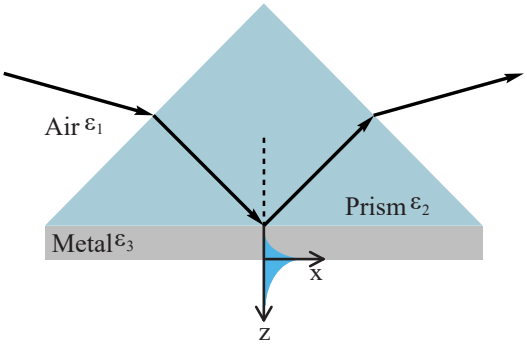

(a) Kretschman configuration

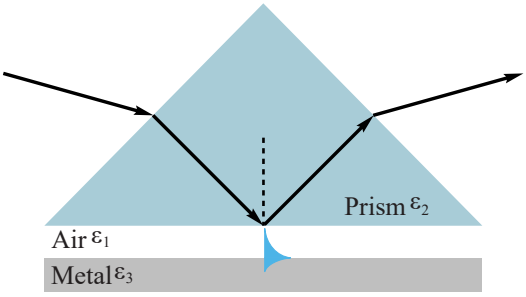

(b) Otto configuration

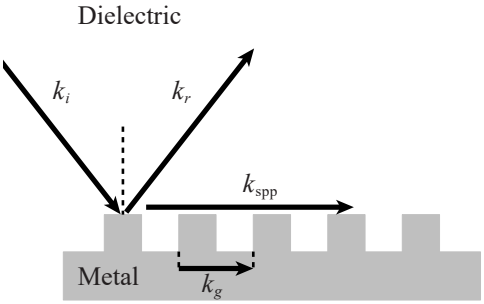

(c) Plasmon coupling via a grating

Figure 3.3: Methods for coupling an electromagnetic wave to a surface plasmon.

3.3 Localised surface plasmon resonances

The final type of plasmon covered in this chapter is the localised surface plasmon resonance (LSPR), which is of most interest to us in this body of work. Localised surface plasmon resonances are relevant to this work as they give rise to increased local electric fields, which can enhance nonlinear optical processes such as second harmonic generation.

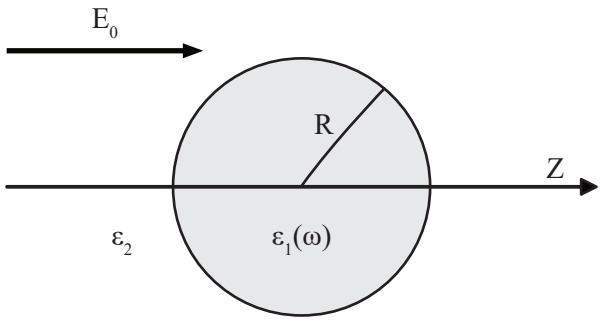

Figure 3.4: Metallic nanoparticle in a dielectric environment in the quasistatic approximation.

Localised surface plasmon resonances are excitations of the conduction band electrons of metallic nanoparticles. The modes of these excitations can be found by considering a metallic nanoparticle in the quasi-static approximation, where the size of the nanoparticle is much smaller than the wavelength of incident light.[29] In the quasi-static approximation, the nanoparticle is small enough that the phase of the electric field can be treated as constant over the volume of the nanoparticle and retardation effects can be excluded.[30] Therefore, the quasi-static approximation allows the system to be solved as an electrostatic problem where the electric field distribution is calculated.[28] The system under consideration is a sphere of radius R, where $R << \lambda$, and complex dielectric function $\varepsilon_1(\omega)$ in a surrounding medium with a real dielectric constant of ε_2. The nanoparticle is illuminated with a homogeneous electric field with amplitude E_0 travelling in the positive z direction, as shown in Figure 3.4.

In the quasi-static approximation, the sphere behaves as a point dipole located at the sphere's centre. The incident electric field induces a polarisation inside the metal sphere, given by $\mathbf{p} = \varepsilon_0 \varepsilon_1 \alpha_{\text{sph}} \mathbf{E}_0$, where α_{sph} is the polarisability of the sphere. The polarisability

of the sphere is given by,[31]

$$\alpha_{\text{sph}}(\omega) = 4\pi R^3 \frac{\varepsilon_1(\omega) - \varepsilon_2}{\varepsilon_1(\omega) - 2\varepsilon_2}. \tag{3.15}$$

Inspecting Equation 3.15, we see that resonance occurs when the denominator is small, which causes the polarisability to become large. In the case of small damping the imaginary part of $\varepsilon_1(\omega)$ is negligible and the resonance condition becomes $\text{Re}[\varepsilon_1(\omega)] = -2\varepsilon_2$, which is known as the Frohlich condition and determines frequency of light needed to excite the lowest order electric dipole.[28] Using the Drude model dielectric function in the case of small damping,[32]

$$\varepsilon(\omega) = 1 - \frac{\omega_{\text{p}}^2}{\omega^2}, \tag{3.16}$$

and substituting in the dielectric function given by the Frolich condition, the resonance frequency is,

$$\omega_{\text{LSPR}} = \frac{\omega_{\text{p}}}{\sqrt{1 + 2\varepsilon_2}}, \tag{3.17}$$

where ε_2 is the dielectric constant of the surrounding medium. From Equation 3.17 we see that changing the surrounding dielectric medium of the nanoparticle tunes the resonance wavelength for example, increasing ε_2 causes the resonance wavelength to redshift.

In the near zone of a nanoparticle at resonance the electric field is highly concentrated at the surface. This high degree of localisation of the electric field in the nanoparticle near field is key to applications in sensing and for increasing the strength of nonlinear optical processes.[33, 34] In the far field radiation zone the electric field pattern appears as a dipole antenna as seen in Figure 3.5.

The advantage of using LSPRs for sensing or enhancing nonlinear optical processes is that LSPRs can be excited directly by illumination, with no need for the phase matching techniques required to obtain SPPs. There exist analytical expressions for the optical properties of nanoparticles with different geometries, such as a nanoparticle wires or nanoparticle ellipsoids.[35] However, numerical simulations are needed to ascertain the optical properties of nanoparticles with more complex geometries.

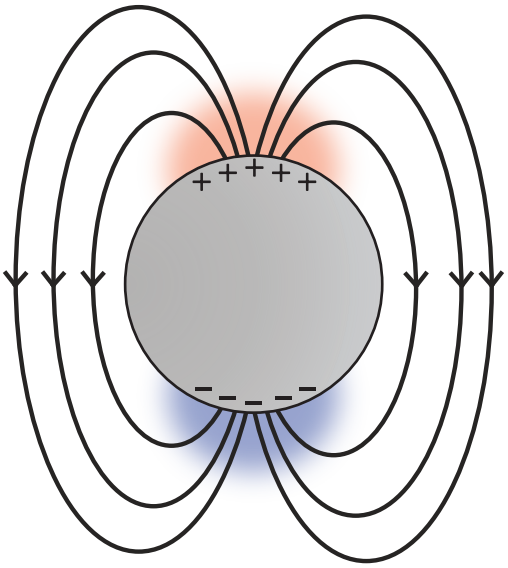

Figure 3.5: The charge distribution and dipole radiation pattern of a nanoparticle under resonance.

3.4 Nanophotonics and metamaterials

The driving force behind research into nanophotonics is the ability to control light on sub-wavelength scales. Manipulating light in optical systems such as a microscopes generally requires the use of bulky optical elements like objectives. Microscope objectives can be designed to produce images with a high magnification, however more elements must to be added to an objective to correct for chromatic, spherical and other aberrations. As a result of minimising aberrations, good quality microscope objectives tend to be rather large. Furthermore, microscope objectives cannot resolve features below the diffraction limit. For an ideal objective, free of imperfections, the diffraction limit states that the smallest resolvable length is given by $d = \frac{\lambda}{2n \sin\theta} = \frac{\lambda}{2NA}$ where λ is wavelength, n is refractive index, θ is the acceptance angle of the objective, and $NA = n \sin\theta$ is the numerical aperture of the objective. To decrease the minimum resolvable length the wavelength can be decreased or the refractive index increased. However, for optical wavelengths the diffraction limit poses a hard limit on resolving power because we are restricted to available materials and cannot arbitrarily reduce the refractive index.

Another way of manipulating light is by routing it from one point to another using waveguides. The most well known waveguide is the optical fibre, on which much of the

worlds telecommunications is now built. Optical fibres are generally made with silica glass and consist of a core and cladding where the refractive index of the core is greater than that of the cladding. Changing the refractive index of either the core or the cladding can be achieved by doping the silica glass. The light in the fibre is guided by the fibre because the refractive index contrast between the core and cladding causes total internal reflection, provided that the incident angle of the light is greater than the critical angle required for total internal reflection. In the last decade waveguides have been incorporated into microelectronics by way of silicon photonics, which have enabled data transmission rates of more than tens of gigahertz.[36] However, just as with microscope objectives, waveguides still rely on the optical properties of available materials. If we want to exert even greater control of light at various length scales it would be advantageous to create materials with bespoke optical properties. One such method is to build metamaterials.

Optical metamaterials consist of subwavelength elements, such that an incident electromagnetic wave experiences an effective medium. The properties of the metamaterial are then determined by the response of the individual elements. Changing the material, size, geometry and arrangement of the subwavelength elements allows for great flexibility in designing metamaterials. Metamaterials arose from the pursuit of negative refractive index.

In 1968 Victor Veselago proposed that a material with simultaneously negative permittivity and permeability would not violate any laws of physics and could therefore exist.[11] A material possessing both negative permittivity and permeability would then have a negative refractive index. However, at the time, it was not possible to create a negative refractive index material and the idea lay mostly dormant.

In the 90's, Sir John Pendry laid the foundations for the resurgence of interest in negative refractive index. First, arrangements of metallic wires were shown to display negative permittivity at gigahertz frequencies, giving rise to low frequency plasmons.[37] Second, split ring resonators were used to achieve negative permeability. Now, the ingredients for a negative index material were at hand.

Interest in negative index materials truly erupted with Pendry's seminal paper, "Negative Refraction Makes a Perfect Lens".[12] In his landmark paper Pendry pointed out how

a slab of negative index material can beat conventional lens by imaging beyond the diffraction limit. Soon after, a material composed of metallic wires and split ring resonators was shown to possess a negative index of refraction for a band of microwave frequencies by Shelby et al..[13] Later, Pendry also published how negative refraction could be achieved with chirality, meaning a negative index metamaterial would only need a single type of element.[38] This then sparked interest in chiral metamaterials, where the individual elements of the metamaterial lacked inversion symmetry.[39][40]

Three-dimensional metamaterials were built to extend negative refractive index to wavelengths shorter than microwaves. Popular designs included stacked split ring resonators[41][42][43] and double fishnet metamaterials.[44][45] To obtain values for the effective permittivity and permeability, the transmission and reflectivity of the metamaterial was measured and then fitted to simulations to extract information, in a process dubbed parameter retrieval.[46] The downside to these layered metamaterials was their arduous fabrication processes, requiring multiple photolithographic steps and precise alignment between layers.[47] A much simpler fabrication strategy is planarization.

Metasurfaces are a class of metamaterials with elements distributed in a single plane. The material parameters permittivity, permeability, and refractive index are bulk properties, which are not easily ascribed to subwavelength metasurfaces. Therefore, negative refractive index has not been the focus of metasurface research.[48] However, metasurfaces are poised for applications including wavefront shaping, holography,[49] beam steering, and polarisation control.[50] Due to their quasi-two-dimensional nature, metasurfaces are more amenable to conventional lithography techniques. Being ultra-thin also means that metasurfaces have reduced losses compared to their three-dimensional counterparts.[51] All of these advantages make metasurfaces more appealing for achieving applications in planar optics.[52]

3.5 Plasmonic enhancement of second harmonic generation

In the endeavour to control light, metamaterials and plasmonics can also modify the wavelength of light. Plasmonics is well suited to enhancing nonlinear optical processes, in particular second harmonic generation (SHG). Firstly, as discussed in Chapter 2 nonlinear

optical processes have a power law dependence on the electric field amplitude. Therefore, enhanced electric near-fields at surfaces boost nonlinear optical processes. Secondly, SHG is highly symmetry sensitive and therefore used to study plasmonic nanostructures.[53] In particular to SHG, the bulk of most metals are centrosymmetric and isotropic, hence electric dipolar SHG from the metal bulk is forbidden. The most significant source of SHG from metals comes from surface electric dipoles. Surface plasmons, and their enhanced fields, are confined to the interface between a metal and dielectric. Therefore, the source of SHG is directly enhanced by surface plasmons.

Furthermore, plasmonics and metasurfaces bypass the need for phase matching.[54] Conventionally, nonlinear crystals are used to achieve frequency conversion but require phase matching in order to generate a significant output. A multitude of phase matching techniques can be employed such as periodic poling, temperature control, and angle tuning. These strict conditions imposed on nonlinear crystals means that only one nonlinear process can be phase matched at a time.[55] On the other hand, plasmonic metasurfaces avoid the need for phase matching because all of the nonlinear sources are excited simultaneously and in a single plane. Therefore, the single plane of nonlinear sources does not need to be phase matched to another set of nonlinear sources. Additionally, all possible nonlinear processes can occur at the metasurface because their sources do not experience destructive interference as they would in a phase matched crystal.

In the ideal case of a perfectly spherical plasmonic nanoparticle, dipole contributions from the metal bulk are forbidden because of the centrosymmetric crystal structure. For particles much smaller than the wavelength of light, the symmetry of a perfect sphere results in the cancellation of the second harmonic surface dipoles.[56] However, metallic nanoparticles deviate in shape from perfect spheres, which breaks inversion symmetry and allows electric dipolar SHG.[57] Second harmonic hyper-Rayleigh scattering experiments on plasmonic nanoparticles examined the output radiation pattern as a function of particle size to determine the dominant contribution to SHG. It was found that gold nanoparicles 20 nm in diameter exhibited a two lobe radiation pattern, indicative of dipolar emission, while 80 nm gold nanoparticles displayed four lobe patterns, illustrating quadrupolar emission.[58] Similar experiments on silver nanoparticles showed dipolar SHG for nanoparticles

as large as 40 nm, while 60 and 80 nm silver nanoparticles demonstrated quadrupolar emission.[59]

Multiple approaches can be taken when designing a plasmonic antenna specifically for enhancing SHG. The most straight forward method is to ensure that antennae have a localised surface plasmon resonance at the fundamental frequency. SHG studies on gold nanorods less than 200 nm long and 60 nm wide determined that SHG was maximised when the polarisation of the fundamental field was parallel to the long axis of the rods and when the fundamental frequency excited a LSPR.[60] Instead of resonances at the fundamental frequency, antennae with resonances at the second harmonic can enhance SHG. For example, aluminium nanorods less than 150 nm long and 60 nm wide displayed a resonance at 520 nm illumination which lead to an enhancement of upto 70 times for SHG emitted along the long axis of the rod, compared to SHG from the rod short axis, when pumped with a near infra-red laser.[61]

Antennae can also be designed with resonances at the fundamental frequency and the second harmonic in order to boost SHG.[62] To demonstrate the advantage of resonances at both the fundamental and second harmonic, doubly resonant antennae consisting of three nanorods were fabricated where the gap between the middle and right rods is resonant at the fundamental and the gap between the middle and left rods is resonant at the second harmonic. The doubly resonant antenna design exhibited a factor of two enhancement of SHG in comparison to antennae only resonant at the fundamental.[63] The spatial overlap of resonances at the fundamental and second harmonic can also increase SHG. Carefully designed antennae comprised of a V-shaped structure coupled to a rod were fabricated to display resonances at both the fundamental and second harmonic in the gap between the V structure and rod, leading to strong SHG.[64]

3.6 Summary

Three types of plasmons have been introduced. First, bulk plasmons which arise from longitudinal wave solutions to Maxwell's equations and are purely depolarising fields that cannot be excited by transverse electromagnetic fields. Second, surface plasmon polaritons which occur at the interface between a dielectric and a metal, but only for P-polarised in-

cident radiation and phase matching techniques. Lastly, the localised surface plasmon was introduced, where the finite size of metallic nanoparticles confines free electrons thereby providing a restoring force that leads to a resonance. The spectral properties of an LSPRs can be tuned by varying the nanoparticle's size, shape, material, and surrounding dielectric environment. This ability to tune LSPRs makes them very attractive for sensing applications, which is already a flourishing field. The highly concentrated electric fields of LSPRs are also utilised in the field of nanophotonics.

Plasmonic materials and nanostructures have been implemented in the fabrication of metamaterials with the ambition to control light at the nanoscale. One particular aim is to control the wavelength of light which can be achieved through nonlinear optical processes. The field enhancements of LSPRs act to boost nonlinear processes, therefore making plasmonic metamaterials an appealing platform for novel nonlinear nanophotonics.

Chapter 4

Experimental overview

The purpose of this chapter is to introduce the equipment, procedures, and techniques common to all of the nonlinear optical experiments performed in Chapters 5 and 6. This includes outlining the specifications of the laser source used to provide the fundamental frequency for the experiments and how its power was controlled. All nonlinear experiments also share the same detector and detection scheme, namely a photomultiplier tube used in a gated photon counting regime. The basic working principles of photomultipliers are covered along with details on how to setup a photon counting scheme. Matters specific to an experiment are covered in the relevant chapter as finer points change between experiments.

4.1 Laser specifications and power control

A Mai Tai HP laser from Spectra-Physics provided the fundamental beam for all of the nonlinear optical experiments. The Mai Tai is a femto-second pulsed tunable titanium-sapphire laser. It has a repetition rate of 80 ± 1 MHz, with a pulse width of approximately 100 fs. When tuned to a wavelength of 800 nm the Mai Tai produces 2.9 W of average power which is enough to destroy most samples. To avoid damaging the samples under investigation it is necessary to reduce the incident power. Reduction of the incident laser power is achieved using two methods.

The first method used to reduce the laser power is to use an optical chopper wheel (SR540 from Stanford Research Systems (SRS)) which consists of a black rotating metal

disc with a window or windows cut out of it. The chopper wheel only lets the laser beam pass through during the windowed portion of its rotation and then blocks the beam the rest of the time. Using an optical chopper has the advantage of reducing the average power while still maintaining the peak pulse power, which is desired for driving nonlinear optical processes. All the nonlinear experiments used a chopper wheel a with 1.7% duty cycle, the duty cycle being the portion of the chopper wheel that is windowed. The chopper was set to a frequency of 42 Hz, which is chosen because the chopper wheel only has one window, making it unbalanced, and causing it to become unstable at higher frequencies and it is also not a multiple of the electric mains frequency.

The second method used to control the incident power was by using two Glan-laser polarisers both with anti-reflection coating (650 - 1050 nm R <1%). The first polariser was mounted in a rotation mount while the second polariser had its orientation fixed with its transmission axis vertical. In this configuration the first polariser is rotated to reduce the power. The laser beam after the fixed polariser then has a clean and known polarisation, because of the 100 000:1 extinction ratio, which can be worked with for experiments.

4.2 Photomultiplier tubes

Photomultiplier tubes (PMTs) are sensitive light detectors that work based on the photoelectric effect and use electron gain to produce measurable current pulses. The schematic layout of a PMT is shown in Figure 4.1. The window allows photons to enter the vacuum tube and strike the photocathode which ejects an electron due to the photoelectric effect. The ejected electron is then accelerated towards the first dynode; all the dynodes are held at a high voltage to accelerate electrons towards them. At each dynode the striking electrons cause secondary electron emissions which travel to the subsequent dynode, which in turn produces more electrons. This process provides a gain in the number of electrons. When the electron pulse strikes the anode, a current pulse is produced. This pulse can be amplified and processed by electronics, such as a photon counter. There are many factors to consider in the choice of a PMT, for example the layout and configuration of the dynodes in the vacuum tube. The window material needs to be transparent for the wavelengths being detected. The choice of photocathode material determines the oper-

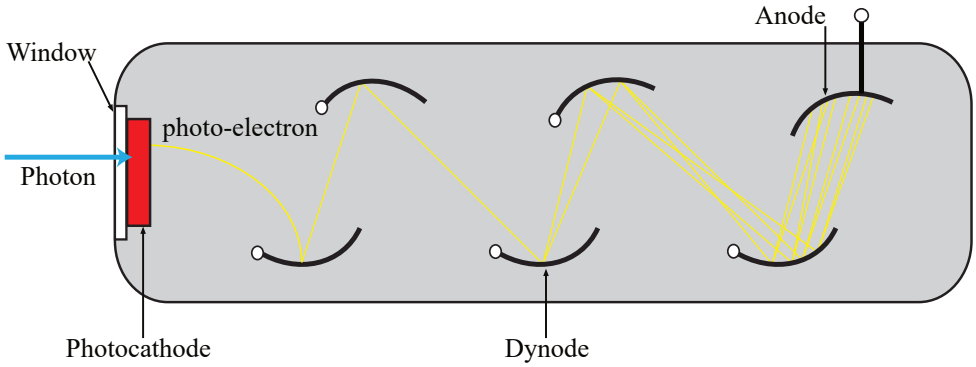

Figure 4.1: Schematic of a head-on photomultiplier tube showing the basic components. The photon passes through the window, striking the photocathode and produces an electron (yellow lines). The electron is accelerated towards the nearest dynode. Upon collision with the dynode secondary electrons are produced. Finally, a current pulse is output from the anode.

ational wavelength range of the PMT because a photon must possess enough energy for an electron to overcome the work function of the photocathode. The configuration of the dynodes affects the collection efficiency of incoming electrons, time response of the system, and pulse shape.

Noise from a PMT appears as dark counts, signal pulses that occur when no light falls on the PMT. Dark counts are mainly caused by thermionic emission of electrons from inside the tube which undergo gain if they are collected by the dynodes. Keeping a PMT inside a cooled housing reduces rate of thermionic emission which dramatically reduces the number of dark counts. However, other sources of dark counts exist, such as cosmic rays and radioactive decay from the materials inside the tube.

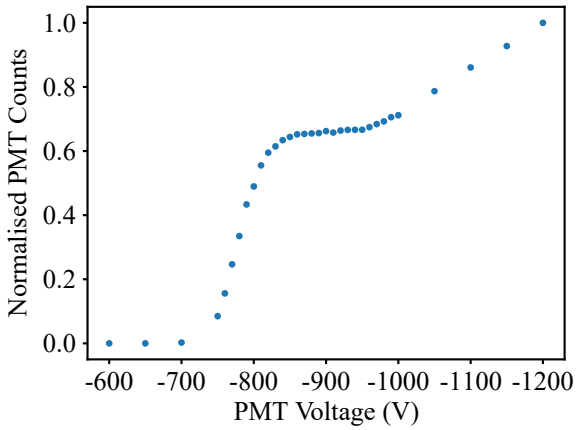

Figure 4.2: Photomultiplier tube plateau characteristics.

A photomultiplier tube (PMT) in a gated photon counting regime was used to detect the signal from second harmonic generation experiments. The PMT used was a model R585 from Hamamatsu and is sensitive to wavelengths in the range of 160 - 650 nm. The quantum efficiency of the PMT at 400 nm is approximately 15%. A FuG power supply was used to apply a voltage of of 875 V across the dynodes of the PMT. This voltage was selected because of a plateau in the gain of the PMT as shown in Figure 4.2. Setting the voltage within the plateau region ensures that the gain is constant, independent of voltage, which may change due to ripple in the PMT power supply. The PMT was enclosed in a FACT50 PMT housing and air cooled to $-20°C$ to reduce the number of dark counts. The PMT housing is able to cool to 50°C below ambient room temperature, however problems with condensation occur when the PMT temperature is low and the humidity in the lab is high.

4.3 Gated photon counting

SHG signal photons generate current pulses that are then output from the PMT anode. The current pules travel along BNC connections to a pre-amplifier (Model SR445 with 350 MHz bandwidth from SRS) where they are amplified by a gain of $\times 25$ and converted to voltage pulses. The amplified voltage pulses are then counted by a gated photon counter (SR400 from SRS). Gating is triggered by using the chopper wheel frequency as a reference. The photon counter has two channels, one gate commences counting once the chopper signal is received. At this point the chopper wheel blocks the laser and therefore only background signal is detected. The second gate starts counting after a set delay so that it counts during the windowed portion of the chopper. Therefore, the second gate counts the signal generated by the sample as well as any background signal. The signal from the first gate is subtracted from the second gate ensuring that only the signal produced by the sample under investigation is recorded. The time for which the channels count pulses is called the gate width which must be equal for both channels for the correct amount of background signal to be subtracted. The timing of the gates relative to the chopper state is shown in Figure 4.3, albeit with a 50% duty cycle for illustrative purposes. The input signal to the photon counter needs to be discriminated once it has been amplified.

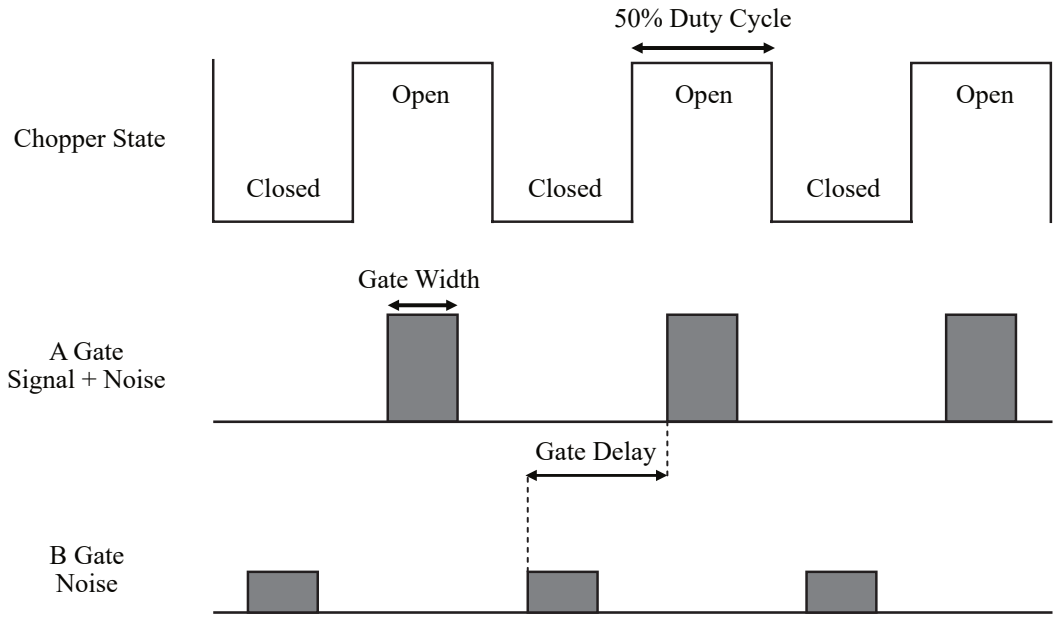

Figure 4.3: Timing of the gates for counters A and B with respect to the state of the optical chopper. The open state refers to the windowed portion of the chopper and the closed state signifies when the beam is blocked by the chopper. Gate A detects signal and noise while gate B detects only noise.

This means rejecting pulses that are below a threshold voltage. Discriminating the pulses stops dark and erroneous signals from being counted, such as pulses from cosmic rays. Discrimination is performed by the photon counter where only voltage pulses within a predetermined window if amplitude are counted. The discriminator levels for gates A and B should be identical. The discriminator levels are set by blocking the entrance to the PMT and waiting for it cool to a stable baseline temperature that will be used in the experiments. If cooling the PMT to $-20°C$ it is best to wait approximately one hour. Once the PMT has cooled the voltage power supply is switched on. Further details on establishing the settings for the photon counter can be found in Appendix C.

Chapter 5

Nanohelices

Sections of this chapter are based on the published manuscript "*Strong Anisotropies Affect Nonlinear Chiral Metamaterials*", David C. Hooper et al.. The work was performed in collaboration with Peer Fischer and Andrew Mark from the Max Planck Institute for Intelligent Systems. All samples were fabricated by A. Mark. Linear characterisation that appears in the published manuscript was performed by C. Kuppe nad J. T. Collins. Nonlinear optical experiments were performed by myself. The data was analysed by myself. The first draft of the manuscript was produced by V. K. Valev and myself.

In Section 3.4 we discussed how metamaterials can be engineered to control light. For example, metamaterials can control the polarisation of light, such as rotating polarisations or even generating exotic polarisation states, like vector vortex beams.[65] Of particular interest is the ability to control circularly polarised light (CPL), because many chemicals and biomolecules are chiral and can therefore be probed with CPL. This has led to a strong interest in chiral metamaterials, which has also been motivated by the idea of optical chirality introduced by Tang and Cohen for sensing chiral molecules as well as Pendry's proposed approach for achieving negative refractive index through chiral metamaterials.[38, 66]

Section 3.5 examined how plasmonic nanostructures enhance nonlinear optical processes allowing metamaterials to control another aspect of light, its frequency. The liberty provided by metamaterial design means that a metamaterial can be designed to control more than one property of light simultaneously. For example, one may wish to specifically

create a metamaterial to achieve strong nonlinear chiroptical (chiral-optical) effects.

To fabricate and characterise a nonlinear chiroptical metamaterial requires a method of quantifying the chirality in the nonlinear regime. While linear chiroptical effects can be related to material parameters, in the case of nonlinear chiroptical effects it is not so straightforward. Other than in the simplest situations, anisotropy greatly complicates the ability to quantify nonlinear chiroptical effects. In this chapter we examine how the rotational anisotropy affects the nonlinear chiroptical response of metamaterial nanohelices.

5.1 Introduction

5.1.1 Chirality and linear chiroptical effects

An object is said to be *chiral* if it cannot be superimposed onto its mirror image through any successive application of rotational or translational symmetry transformations. On the other hand, objects that can be superimposed onto their mirror image are said to be *achiral*. The two mirror images of a chiral object are called enantiomers, usually in reference to molecules, or enantiomorphs, referring to chiral objects in general. Enantiomorphs are labelled as either left- or right-handed, with the convention stemming from the fact that the word 'chiral' originates from the Greek for 'hand'.

The first recorded, written, use of the word chiral was by Lord Kelvin in 1894 [67, 68]. However, the study of chirality predates the term with the observation of optical rotation by the French scientist Arago in 1811[69]. Today, chiroptical (chiral optical) effects fulfil a crucial role in the life sciences as many bio-molecules and pharmaceuticals are chiral. Chiroptical effects are used to discriminate between enantiomers of a molecule or to determine the prevalence of one enantiomer over the other in a mixture. The importance of chiral sensing is apparent when considering how two enantiomers can have vastly disparate effects on the human body. While one enantiomer can act as a medicine, the other enantiomer can have more sinister and potentially deadly effects. Most notable is the infamous case of thalidomide, where one enantiomer alleviates morning sickness, while the other causes birth defects.[70]

The chirality of an object only becomes apparent when it interacts with another chiral

system. Therefore, to investigate the chirality of a material we need to use a probe that also possesses chirality. Fortuitously, light can be chiral. An electromagnetic wave is chiral when the electric field vector rotates about its axis of propagation in time. To obtain a chiral electromagnetic wave first consider a wave propagating in the z direction, and linearly polarised along x,

$$\mathbf{E}_{\mathrm{x}}(z,t) = E_{0\mathrm{x}}\cos(kz-\omega t)\hat{\mathbf{i}}, \tag{5.1}$$

where $E_{0\mathrm{x}}$ is the electric field amplitude, k is the wavevector, and ω is the angular frequency. Using the principle of superposition, another wave can be added or subtracted to the original wave. This additional wave shall propagate in the same direction as the wave in Equation 5.1 and be linearly polarised along the y direction. Importantly, the new wave will have a phase difference of $\frac{\pi}{2}$ so that it can written as,

$$\mathbf{E}_{\mathrm{y}}(z,t) = E_{0\mathrm{y}}\sin(kz-\omega t)\hat{\mathbf{j}}. \tag{5.2}$$

The result of adding or subtracting the linearly polarised waves in Equations 5.1 and 5.2 yields,

$$\mathbf{E}_{\mathrm{RCP}}(z,t) = E_{0\mathrm{x}}\cos(kz-\omega t)\hat{\mathbf{i}} + E_{0\mathrm{y}}\sin(kz-\omega t)\hat{\mathbf{j}}, \tag{5.3}$$

$$\mathbf{E}_{\mathrm{LCP}}(z,t) = E_{0\mathrm{x}}\cos(kz-\omega t)\hat{\mathbf{i}} - E_{0\mathrm{y}}\sin(kz-\omega t)\hat{\mathbf{j}}, \tag{5.4}$$

where $E_{0\mathrm{x}} = E_{0\mathrm{y}}$, and the subscripts RCP and LCP denote whether the wave is left- or right-circularly polarised. As a circular wave propagates forward in time its electric field vector traces out a circle in the $x-y$ plane. The handedness of the wave is determined by the direction of rotation of the electric field vector, which depends on the observer's frame of reference. The convention used here fixes the reference frame from the point of view of the source looking along the direction of propagation. If the electric field vector rotates in a clockwise fashion, then the wave is right-handed. If the electric field vector rotates in an anti-clockwise fashion, then the wave is left-handed. We can now examine how our probe, circularly polarised light (CPL), interacts with chiral media and how their

interaction results in different chiroptical effects.

5.1.2 Linear chiroptics

To describe the linear optical response of an isotropic chiral material it is necessary to introduce the chirality parameter κ into the constituent relations, which relate the electric displacement and magnetic fields to the electric and magnetic induction fields, respectively. The chirality parameter describes magneto-electric cross coupling, whereby an incident electric field gives rise to a magnetic response and vice versa. It appears in the constituent relations as,[39]

$$\begin{bmatrix} \mathbf{D} \\ \mathbf{B} \end{bmatrix} = \begin{bmatrix} \varepsilon_0\varepsilon_r & i\kappa\sqrt{\mu_0\varepsilon_0} \\ -i\kappa\sqrt{\mu_0\varepsilon_0} & \mu_0\mu_r \end{bmatrix} \begin{bmatrix} \mathbf{E} \\ \mathbf{H} \end{bmatrix}, \tag{5.5}$$

where $\mathbf{D}$ is the electric displacement field (electric flux density), $\mathbf{B}$ is the magnetic induction field, ε_0 is the permittivity of free space, ε_r is the material permittivity, μ_0 is the magnetic permeability of free space, μ_r is the material magnetic permeability, $\mathbf{E}$ is the electric field, and $\mathbf{H}$ is the magnetic field intensity. As a result of the constituent relations in Equation 5.5 CPL experiences a different index of refraction depending on its handedness.[71] The refractive indices for RCP and LCP light can be written as $n_+ = n + \kappa$ and $n_- = n - \kappa$, where n is the refractive index of the racemic medium.[72] Due to the difference in refractive indices, RCP and LCP light undergo different amounts of absorption in chiral media. This difference in absorption between LCP and RCP is called circular dichroism (CD). Depending on its handedness, circularly polarised light also experiences a different phase velocity in a chiral medium. The difference in phase velocity between the two polarisation states results in optical rotation (OR), where the plane of polarisation of a transmitted linearly polarised wave is rotated. Initially, optical rotation seems counterintuitive given that linearly polarised light is achiral. However, a linear polarisation can be expressed as the sum of two circularly polarised waves with opposite handedness, much like how circularly polarised light is expressed as the sum of linear polarisations in Equation 5.4.

The two chiroptical effects of CD and OR are linked by the Kramers-Kronig relations which allows the behaviour of both effects to be found when only one has been measured,

provided a full spectrum is obtained, in other words a wide range of wavelengths need to be measured the relations to be effective.[32] We have now seen how CPL can be used to probe chiral media by measuring different chiroptical effects. While the chirality of physical media is quantified by κ, the chirality of light can also be parametrised.

The chirality of optical fields can be quantised by the optical chirality parameter, C which is a conserved quantity of electromagnetic fields first introduced by Lipkin [73] who named it the Lipkin 00 zilch,

$$C = \frac{\varepsilon_0}{2}\mathbf{E}\cdot\nabla\times\mathbf{E} + \frac{1}{2\mu_0}\mathbf{B}\cdot\nabla\times\mathbf{B}. \tag{5.6}$$

In a geometrical picture the optical chirality parameter is a measure of how parallel the electric and magnetic fields are to each other. The zilch was initially dismissed as it could not be directly probed and was consequently was not developed.[74] However, the zilch was later popularised by Tang and Cohen, who rebranded it as optical chirality.[66] Tang and Cohen went on to devise a system to generate a field with optical chirality greater than that of CPL for applications in enantioselective sensing of molecules.[75] Numerous works studied how best to achieve fields with high optical chirality using nanostructures.

We have now briefly seen how chirality in linear optics can be quantified. The linear chiroptical effects of circular dichroism and optical rotation are essentially a probe of a material's refractive index. CD measuring the imaginary part and OR measuring the real part. Because they both measure the complex refractive index they are linked by the Kronig-Kramers relation. The chirality of light can also be quantified by way of the optical chirality parameter C. Next we shall examine chirality in the nonlinear optical process of second harmonic generation (SHG).

5.1.3 Chirality in SHG

As we have seen in the previous section, the chirality of a material and its interaction with light is expressed by the chirality parameter κ, which can be used to describe CD and OR. However, quantifying the interaction of chiral media with light in the nonlinear optical regime requires a different approach. In this section we examine how chirality is quantified in the nonlinear optical process of SHG.

In Section 2.4 we demonstrated how the symmetry of a material is applied to its nonlinear susceptibility tensor. In order to examine chirality in SHG we begin by finding the susceptibility tensor for a surface that is rotationally isotropic in the $x-y$ plane. To obtain this isotropic tensor we apply the transformation matrix for an arbitrary rotation, θ, around the z axis,

$$R_z(\theta) = \begin{bmatrix} \cos(\theta) & -\sin(\theta) & 0 \\ \sin(\theta) & \cos(\theta) & 0 \\ 0 & 0 & 1 \end{bmatrix}. \tag{5.7}$$

The resulting reduced tensor is then given by:

$$\chi_{C_\infty} = \begin{bmatrix} 0 & 0 & 0 & xyz & xxz & 0 \\ 0 & 0 & 0 & xxz & -xyz & 0 \\ zxx & zxx & zzz & 0 & 0 & 0 \end{bmatrix}, \tag{5.8}$$

where the following tensor relations have already been applied: $zxx = zyy$, $xxz = yyz$, $xyz = -yxz$. The tensor in Equation 5.8 is chiral because mirror symmetry has not been applied it. To find the tensor components related to chirality we apply mirror symmetry to the C_∞ tensor and find which ones vanish. Applying mirror symmetry in either the $x-z$ or $y-z$ plane yields the following tensor for an isotropic achiral surface:

$$\chi_{C_{\infty v}} = \begin{bmatrix} 0 & 0 & 0 & 0 & xxz & 0 \\ 0 & 0 & 0 & xxz & 0 & 0 \\ zxx & zxx & zzz & 0 & 0 & 0 \end{bmatrix}. \tag{5.9}$$

Examining the difference between the tensors in Equations 5.8 and 5.9 we find that the only component eliminated by mirror symmetry is xyz. Because the xyz component is eliminated in the achiral isotropic tensor it is often referred to as the *chiral tensor component*. In molecular thin films isotropy arises because all the molecules are randomly orientated. However, using conventional lithography to create a nanostructured surface where the elements are randomly orientated would be challenging. Fortunately, there is route to obtaining chiral planar isotropy that is compatible with traditional lithography techniques. Inspecting the second order nonlinear susceptibility tensor for 4-fold rotational

symmetry in Equation 2.38 we can see that it is remarkably similar to the C_∞ tensor in Equation 5.8.[76] The only extra component in the C_4 tensor is zxy. As the present discussion is limited to SHG we can apply the permutation rule presented in Section 2.4 whereby the last two indices of any component can be freely interchanged. Keeping permutation symmetry in mind and using direct inspection to apply the relevant transformation to the zxy component, we find that $zxy \rightarrow -zyx$. In the case of SHG, we can now see that $zxy = -zxy$ and must therefore vanish. We have just demonstrated that the C_4 and C_∞ SHG susceptibility tensors are equivalent. It can also be shown that the C_{4v} tensor is identical to the $C_{\infty v}$ tensor using the same method of applying mirror symmetry to the C_4 tensor. Nanostructures with C_4 symmetry can easily be fabricated and thus chirality in SHG investigated. This tactic of creating geometries with C_4 symmetry has been used to make the interpretation of results easier as the chirality is characterised by a single tensor component, xyz.[77]

5.1.4 Nonlinear chiroptical effects

We have shown how chirality in SHG is determined by the single susceptibility tensor component xyz, for the simplest case of an isotropic chiral surface. Now, we turn our attention to chiroptical effects in nonlinear optics. First, we shall examine SHG circular dichroism which is defined as,

$$\text{SHG-CD} = \frac{I_{\text{RCP}}(2\omega) - I_{\text{LCP}}(2\omega)}{I_{\text{RCP}}(2\omega) + I_{\text{LCP}}(2\omega)}, \tag{5.10}$$

where ω is the angular frequency of the fundamental and $I_{\text{RCP/LCP}}(2\omega)$ is the intensity of the SHG, with subscripts denoting the handedness of incident CPL. It should be noted that some definitions used in literature include a factor of 2 due to normalising the sum of the intensities. The definition used here is normalised to give values between 1 and -1. There is also some contention in the literature as to whether this effect should be referred to as a circular dichroism or a circular intensity difference. This is because the effect is not due to differences in the refractive index and is, strictly speaking, therefore not a dichroism.[78]

Chirality can also give rise to SHG optical rotation (SHG-OR). Similar to its linear

counterpart, SHG-OR results in the plane of polarisation of the SHG being rotated. When the fundamental beam is S-polarised the angle of SHG-OR is given by,

$$\phi_{\text{SHG-OR}} = \arctan\left(\frac{E_{\text{S}}(2\omega)}{E_{\text{P}}(2\omega)}\right), \tag{5.11}$$

where $E_{\text{S/P}}(2\omega)$ is the S- or P-polarised component of the second harmonic electric field. For an isotropic chiral surface incidence with P-polarised light, SHG-OR simply becomes the ratio of the chiral to achiral tensor components.

Finally, chirality can give rise to an SHG linear dichroism (SHG-LD). The nonlinear chiroptical effect of SHG-LD produces a different SHG intensity when illuminated with linearly polarised light rotated $+45°$ or $-45°$ from the S-polarisation direction and is quantified by,

$$\text{SHG-LD} = \frac{I_{-45°}(2\omega) - I_{+45°}(2\omega)}{I_{-45°}(2\omega) + I_{+45°}(2\omega)}, \tag{5.12}$$

where $I_{-45°/+45°}$ is the SHG intensity with subscripts denoting the rotation of the incident linear polarisation.

5.1.5 Anisotropy and nonlinear chiroptics

From previous work on chiral molecular films, it is known that the anisotropy of a medium and the geometry of an experiment affects the measured nonlinear chiroptical response.[79–82] In fact, measurement techniques have been demonstrated to avoid the issue by illuminating the samples at normal incidence.[83, 84] However, investigating nonlinear chiroptical effects at normal incidence limits the number of tensor elements that can be probed. For example, if the sample lies in the $x - y$ plane then tensor elements containing a z index cannot be addressed. Therefore, normal incidence studies impose a limit on the information that can be retrieved, hindering nonlinear chiroptical characterisations.

Comprehensive studies of chiral G-shaped nanomaterials have explicitly addressed the significant effects that anisotropy can have on the SHG chiroptical response. The anisotropic coupling of plasmon modes to the incident polarisation was found to explain azimuthally dependent enhancements of the SHG response of planar G-shape structures.[85] It was also found that anisotropy affected the SHG-OR of four-fold supercell G-shaped

nanostructures, as the degree of polarisation rotation was dependent on the azimuthal orientation of the sample.[86] Later work examined the effect of anisotropy on the SHG-CD of the supercell G-shape structures and again found a strong dependence on sample azimuthal rotation as well as on the angle of incidence, with the SHG-CD even changing sign.[87]

Another form of anisotropy arises when a tilted achiral metamaterial displays chiroptical behaviour. This response is known as extrinsic chirality, or pseudo-chirality in the study of molecular thin films. Extrinsic chirality occurs because a tilted achiral surface forms a different image in the frame of reference of the incident light, depending on if it is tilted left or right, as shown in Figure 5.1. This effect was observed by Plum et al. by changing the angle of illumination upon asymmetric split ring resonators. [88, 89] An advantage of using extrinsic chirality to engineer a material's chiroptical response is that the effect is amenable to planar designs which are easier to fabricate with traditional lithography techniques. Additionally, only one sample needs to be fabricated as the other enantiomorph is obtained by switching the angle of incidence which then reverses the chiroptical response.

Extrinsic chirality has also been demonstrated in SHG-CD by Belardini et al. with the use of curved and tilted nanowires.[90, 91] In these cases the curve or tilt of the nanowires, the sample normal, and the incident wavevector form a chiral triad of vectors which gives rise to the effect of extrinsic chirality. Moreover, by adjusting the orientation of the nanowires relative to the incident light causes the susceptibility tensor to change.[91]

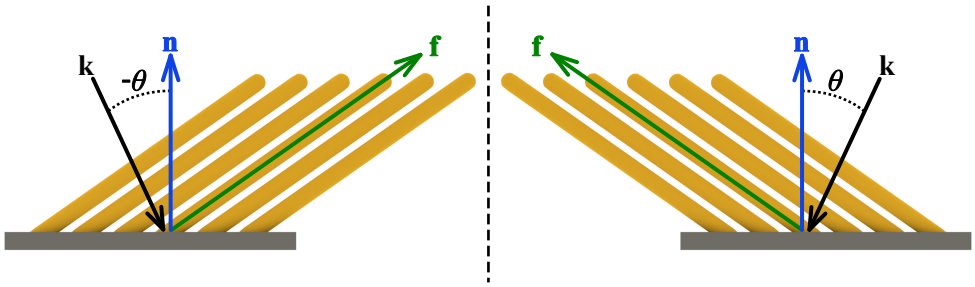

Figure 5.1: Example of extrinsic chirality with tilted wires. The vector **f** points along the direction of the wires. The vectors in the mirror image form a triad with opposite handedness compared to the original object.

5.1.6 Chiral metamaterials

Chiral nanomaterials [39, 40, 72, 92–95] have attracted attention for applications in controlling light, such as negative refractive index,[38], enhanced enantiomeric chemical sensing,[96], enhancing optical chirality of near fields [97, 98] and use as broadband circular polarisers [99, 100] or detectors.[101]

Chirality is an intrinsically a three-dimensional property because inversion symmetry must be broken in each dimension, however a great number of works have focused on so-called "planar" nanostructures. A few recent examples include S-shaped nanostructures,[102, 103] three- and four-fold symmetric propellers,[104] and heptamers.[105] These planar chiral nanostructures are very attractive because of their ease of fabrication with conventional top down methods such as electron beam lithography. The necessary three-dimensional symmetry-breaking arises from a dissymmetry along the axis perpendicular to the sample plane,[106] for instance, due to the presence of a substrate on one side of the sample and air on the other. Although planar metamaterials are thus three-dimensional, it is clear that their three-dimensionality is not very pronounced. At optical frequencies various three-dimensional structured nanomaterials have been proposed, such as rosettes,[107, 108] twisted arcs,[109] 3D shuriken,[110] stacked split rings,[42, 111] oligomers,[112, 113] gyroids,[114] and helices.[98, 115–117] Of all these examples, the latter (i.e., the helix) is the archetypical chiral structure. The strong interaction of nanohelices with circularly polarised light gives rise to large chiroptical effects, such as circular dichroism. This makes them attractive for applications involving CPL.[99–101, 118, 119] Thus, the nonlinear optical response of helical nanomaterials is of particular interest as they already demonstrate strong linear chiroptical effects.

Nonlinear chiroptical effects are appealing for their various advantages over their linear counterparts. Firstly, the magnitude of nonlinear chiroptical effects, such as SHG-CD and SHG-OR, are much more pronounced in comparison to their linear analogues.[120–122] Additionally, nonlinear chiroptical effects proceed via different mechanisms than their linear counterparts. For instance, linear circular dichroism requires coupling between electric and magnetic dipoles, while on the other hand, SHG-CD can be observed due solely to electric dipoles.

In many cases the linear chiroptical response of a medium can be understood and quantified by way of the chirality parameter. For example, negative refractive index in chiral materials can be understood as different refractive indices for left- and right-handed CPL, where one handedness experiences such a large chirality parameter that the refractive index becomes negative. Optical fields can also be chiral, such as the well-known example of CPL, and is quantified by optical chirality parameter which can be calculated numerically using commercial software. However, when it comes to quantifying and understanding how the chirality of a material affects its nonlinear chiroptical response it is not so straightforward.

In Section 5.1.3 we demonstrated that the chirality of an isotropic chiral surface is characterised by the single tensor component xyz. To deduce which tensor components are related to chirality requires finding which components vanish with the application of mirror symmetry. For a chiral object with low symmetry, such as a helix, this results in many tensor components contributing to its nonlinear chiroptical response. Therefore, the nonlinear chiroptical behaviour cannot be quantified by a single parameter. Furthermore, as explained in Section 5.1.5, the geometry of an experiment gives rise to extrinsic chirality, which additionally complicates the matter.

Here, in this chapter, the nonlinear chiroptical response of metamaterial nanohelices are presented. Three sets of helical enantiomorphs with different geometrical parameters were studied. Their nonlinear chiroptical response was probed using continuous polarisation measurements. From these measurements we identify symmetries in the response attributable to different parts of the array and helical structure. The behaviour as a function of sample rotation is examined to reveal the effects of anisotropy. Finally, we see how rotational anisotropies affect the SHG-CD and how it is not a reliable measure of nonlinear optical chirality when used as a one-shot measurement.

5.2 Experimental Details

5.2.1 Optical set-up

The laser and photon counting detection system described in Chapter 4 were used in the nonlinear optical investigations of the metamaterial nanohelices. The layout of the optical bench is shown in Figure 5.2. The Mai Tai laser was set to a central wavelength of 800 nm and the average power incident on the sample reduced to 8.5 mW. After the optical chopper, the laser beam passes through an achromatic half waveplate (Thorlabs AHWP10M-980, range: 690 nm - 1200 nm), which is mounted on a computer-controlled rotation stage (Thorlabs PRM1/MZ8 stage). The half waveplate controls the orientation of the linear polarisation.

An anti-reflection coated polariser mounted (Thorlabs GL10-B, AR coating: 650 nm – 1050 nm) in a motor-controlled rotation stage removes any ellipticity induced by the half waveplate. This polariser is necessary because the retardance of the waveplate is not spectrally flat; therefore, not all frequency components of a laser pulse experience the same retardation. An achromatic quarter wave-plate (Thorlabs AQWP10M-980, range: 690 nm – 1200 nm), again mounted in a computer-controlled rotation stage, is used to obtain circular and elliptical polarisation states. The laser beam is focused onto the sample with an achromatic doublet with anti-reflection coating (Thorlabs AC254-150-B-ML, AR coating: 650 nm – 1050 nm, f=150 mm), which results in an ideal spot size of approximately 50 μm. The focusing lens is mounted on a motorised translation stage (Thorlabs DDSM100/M stage) to precisely control its position. A coloured glass filter (Thorlabs FGL665M, Schott Glass RG665 , 1×10^{-5}% transmission at 400 nm, 90% transmission at 800 nm) removes any light at the second harmonic (400 nm). The focused beam is incident on the sample at an angle of 45°. The sample is mounted on a motorised rotation stage (Thorlabs NR360S/M) to rotate it azimuthally.

The reflected beam and SHG signal passes through a coloured glass band pass filter, which rejects the 800 nm fundamental but allows 400 nm SHG to pass through (Thorlabs FGB39, Schott glass BG39 87% transmission at 400 nm and 1.9×10^{-5}% transmission at 800 nm). A second achromatic doublet lens with anti-reflection coating suited to the second

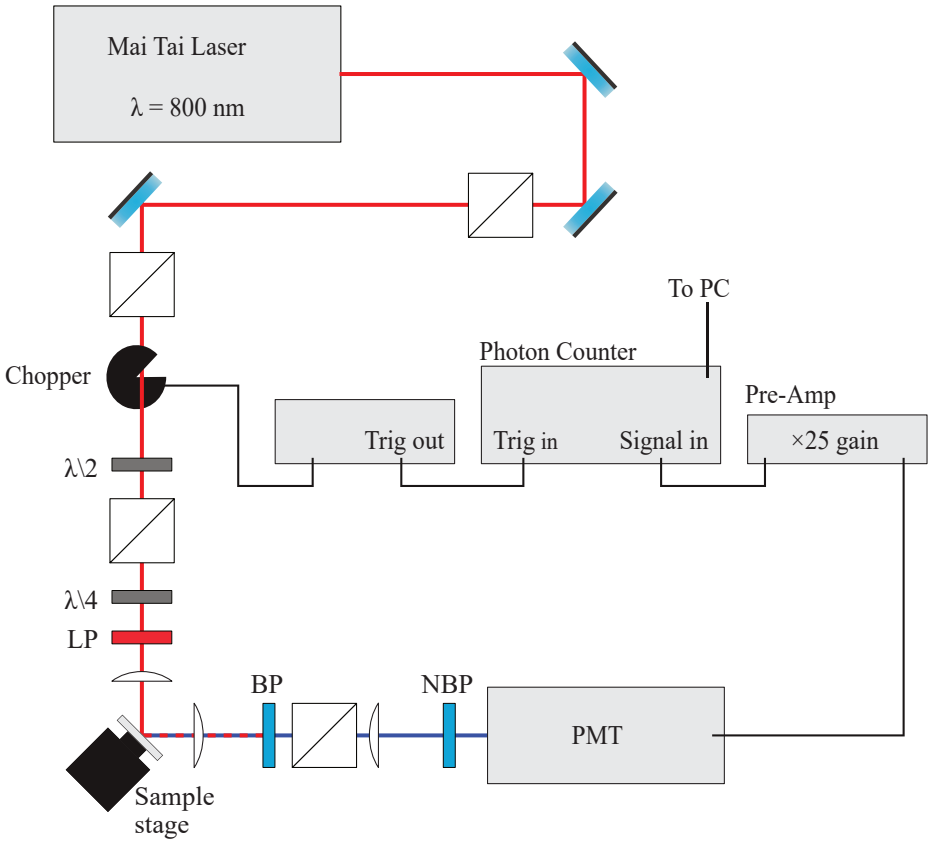

Figure 5.2: Schematic of the optics bench layout used to measure the SHG response of nanohelices. LP = long pass filter, BP = bandpass filter, NBP = narrow bandpass filter.

harmonic (Thorlabs AC254-150-A-ML, AR coating: 350 – 750 nm, f = 150 mm) collimates the SHG. An anti-reflection coated polariser acts as an analyser (Thorlabs GL10-A, AR coating: 350 nm – 700 nm), decomposing the SHG into its vertically and horizontally polarised components. The analyser is mounted in a motorised rotation stage. An anti-reflection coated lens (Thorlabs LA1708-A-ML, AR coating: 350 nm – 700 nm, f=200 mm) focuses the signal into the photomultiplier tube (PMT). A final narrow band pass filter (Thorlabs FB400-10, 37% typical transmission at 400 nm) with a central wavelength of 400 nm and a FWHM of 10 nm rejects any spurious light or light generated from other multiphoton processes. The SHG is detected by the PMT and processed using the scheme described Chapter 4

5.2.2 Continuous polarisation measurements

The advantage of this experimental set-up is that many of the optical components that require adjusting are mounted on computer-controlled rotation or translation stages. Using automatic stages allows experiments to be automated for in-depth characterisations of the nonlinear optical response of samples over large parameter spaces. All motorised stages were controlled using a LabVIEW program that was developed inhouse.

The nanohelices were characterised using a technique named "continuous polarisation measurements", where the polarisation of light incident on the sample is changed using a quarter waveplate (QWP). Rotating the QWP gives access to linear, elliptical, and circular polarisations. Using this method reveals the material's response as the polarisation is continuously changed. In addition to rotating the QWP, the helices were also rotated about their surface normal, revealing how anisotropy influences their nonlinear chiroptical response. In these experiments the samples were rotated in steps of 3° over a full rotation. Then, for each sample rotation the QWP was rotated in 5° steps over a full rotation. This procedure was repeated for all four polariser-analyser combinations, e.g., vertical-in horizontal-out.

5.2.3 QWP and CPL conventions

To properly analyse and interpret the results presented later in this chapter it is important to state the convention used to define the handedness of circularly polarised light. In this chapter, a clockwise rotating electric field vector, as viewed by the receiver, is right circularly polarised (note that this is opposite of the definition given in Section 5.1.1). This definition is important because in these experiments the zero-degree position of the QWP has its fast axis aligned parallel to the plane of the optics bench. Therefore, a P-polarised beam produces RCP light at QWP angles of 45° and 225°, while LCP light is produced at QWP angles of 135° and 315°. On the other hand this is reversed for an S-polarised beam incident on the same QWP, which will give LCP light at 45° and 225°, and RCP light at 135° and 315°. This is shown in Table 5.1.

	Incident polarisation	
QWP Angles	P-in	S-in
45°/225°	RCP	LCP
135°/315°	LCP	RCP

Table 5.1: The resulting circular polarisation states for the different incident orthogonal linear polarisations. RCP denotes right-handed circularly polarised light and LCP denotes left-handed circularly polarised light.

5.3 Nanohelices

5.3.1 Anatomy of a helix

The helix can be considered an archetypical chiral object. So much so that theoretical models of linear and nonlinear optical activity have been based upon the motion of an electron on a helical path. Figure 5.3 shows a rendering of a helix labelled with its basic geometrical parameters. The pitch of a helix is the vertical separation between turns, where a turn is a complete revolution around the helical axis. The height of a helix is determined its pitch and the number of turns. The wire width is the diameter of the circular cross of the helix body. The diameter is the width of the helix, which can be further divided into the inner diameter, outer diameter, and average diameter.

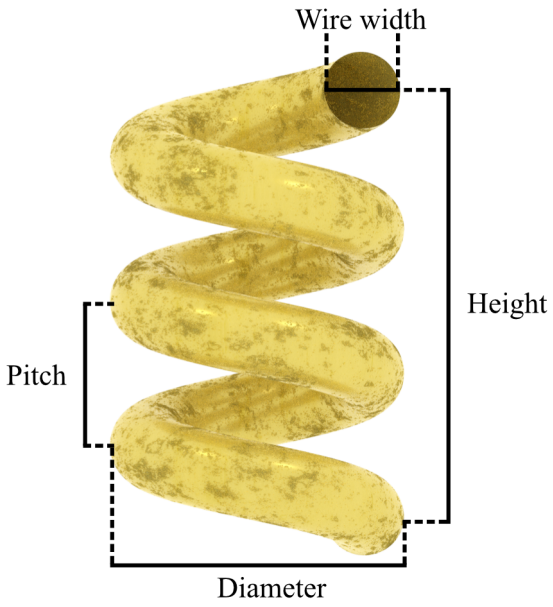

Figure 5.3: A rendering of a metallic helix labelled with its basic geometrical parameters

5.3.2 Fabrication technique

The nanohelices investigated in this work were fabricated by A. G. Mark at the Max Planck Institute for Intelligent Systems in the group of P. Fischer. The fabrication process utilises a combination of dynamic physical vapour deposition and diblock copolymer micelle nanolithography (BCML).[123] This fabrication process allows control of the geometrical parameters of the helices, such as the pitch, number of turns, major and minor radius, and material composition.

The precursor material is a solution of self-assembled micelles, each micelle consists of a gold nanoparticle at its centre surrounded by diblock copolymer.[124] A monolayer of gold loaded micelles is deposited onto the substrate via spin-coating. The gold nanoparticles' size and spacing are controlled by changing the molecular weight of the polymer. The monolayer forms a quasi-hexagonal array on the substrate because of the spherical close packing of the micelles. Plasma etching removes the polymer shell to leave only the gold nanoparticles on the substrate.[125] The gold nanoparticles act as seed points for the growth of the helices. To grow the helices, the substrate is placed into an evaporation chamber at an oblique angle to the vapour flux, a technique known as glancing angle deposition (GLAD). Electron beam evaporation is used to deposit the material. During the deposition columns form on the nanoparticle seeds due to shadow growth. Rotating the substrate during the deposition process results in helices forming. The ratio between the rotation rate and deposition rate determines the pitch of the helix. The height of the helices is determined by the duration of the material deposition.[126]

5.3.3 Sample characteristics

A total of six nanohelix samples where characterised with nonlinear continuous polarisation measurements. The six samples are comprised of three pairs of enantiomorphs. For each pair of enantiomorphs the nominal fabrication parameters were varied to produce helices of different dimensions. The fabrication parameters and measured dimensions of the nanohelices are shown in Appendix D. The heading "pattern" in Appendix D refers to the diblock copolymer micelle nanolithography method used to fabricate the helices. The first value given in the pattern is the diameter of the nanoparticle which acts as the

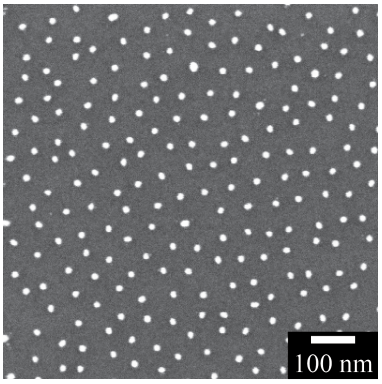

(a)

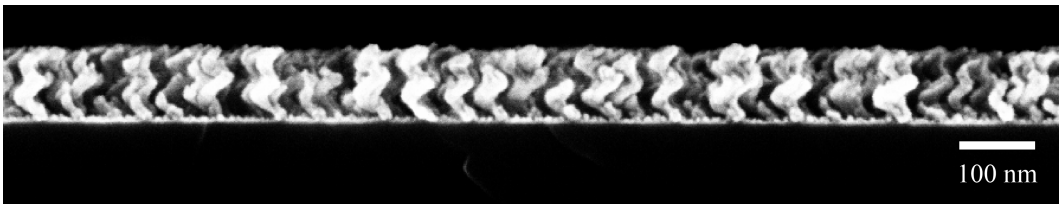

(b)

Figure 5.4: Scanning electron micrographs (SEM) of (a) the gold nanoparticles on a substrate after plasma etching of the micelle monolayer, and (b) the right-handed A-series helices after fabrication. Image courtesy of A. G. Mark.

seed for the helix growth and determines the wire thickness. The second value specified in the pattern is the diameter of the micelle that forms around the metallic nanoparticle, which determines the nanoparticle spacing and hence the array spacing of the finished helices. Each nanohelix is an alloy of 80% gold and 20% copper, alloying is achieved by evaporating the metals simultaneously but at different rates. The nominal dimensions of thickness and pitch are input parameters for the fabrication process, where a negative pitch implies that the resulting helices are right handed. The definition of handedness is given by the right-hand screw rule out of the plane of the substrate. Scanning electron microscopy was used to measure the height and pitch of the helices after fabrication.

The difference between the three sets of helical enantiomorphs is shown schematically in Figure 5.5. The A-series nanohelices have the smallest nanoparticle seed size and array spacing. The B-series sample have the same nominal height and pitch as the A-series but their nanoparticle seed size and array spacing are larger. The C-series have a similar nanoparticle seed size and array spacing to the B-series, but their measured height

and pitch are larger. Investigating three different sets of nanohelices means the effect of changing the helical geometrical parameters on the their nonlinear chiroptical response can be studied.

An example of the linear optical properties of the A-series helices are shown in Figure 5.6. A reflection spectra for the A-LH helices is shown in Figure 5.6a where the spectra was normalised to the reflection spectra of a silver mirror under a ×5 magnification microscope objective and illuminated with a halogen bulb, spectra were recorded with an Ocean optics QE-Pro spectrometer. The linear CD of the A-series helices is shown in Figure 5.6b, spectra were obtained in a similar fashion to the reflection spectra but with an achromatic waveplate in the light path. The CD of the helices is opposite at 800 nm, which is the wavelength of the fundamental used in the nonlinear experiments. From the reflection

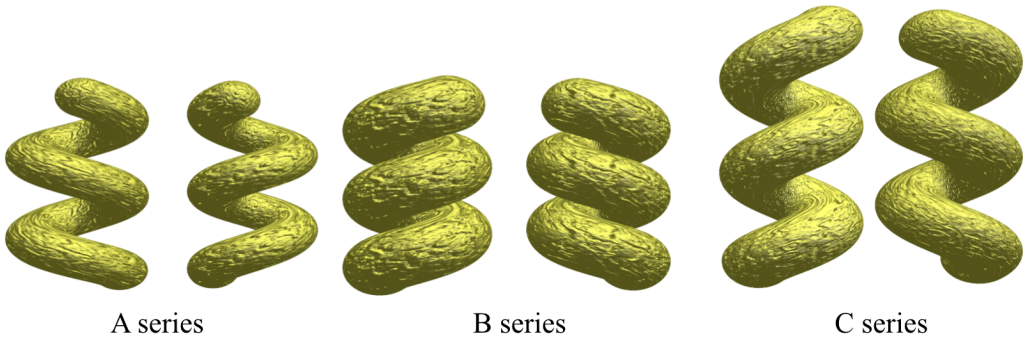

Figure 5.5: Schematic comparing the different size of each set of helices.

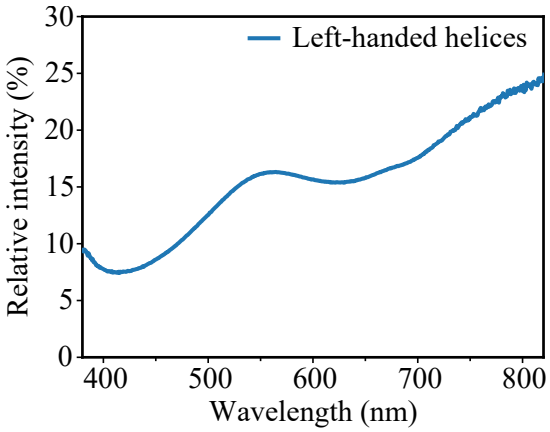

(a) Reflection spectra

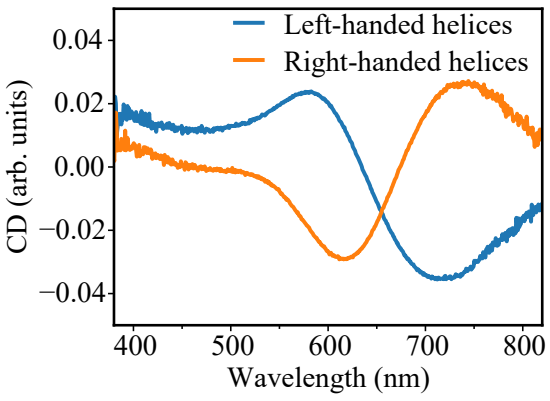

(b) Circular dichorism.

Figure 5.6: (a) Linear reflection spectra of the A-LH nanohelices. (b) Linear circular dichroism of the A-series nanohelices. Data collected by Joel T. Collins

spectra we can see that there is not an LSPR at 800 nm because of the steadily increasing reflection. The reflection spectra reveals that it is likely the LSPR is located in the range between 600-700 nm. Ideally there would be a plasmon resonance within the wavelength range of our experimental capabilities.

5.4 Results and Discussion

5.4.1 A-series nanohelices

Results of the continuous polarisation measurements on the left-handed A series nanohelices (A-LH) are shown Figure 5.7 The plots show how the SHG intensity depends on the sample's azimuthal angle and on the angle of the quarter waveplate. Each plot corresponds to a different state of the initial polarisation, incident on the quarter-wave plate, and the signal output polarisation. These different states are referred to as polariser-analyser configurations.

The P-in P-out data for sample A-LH are shown in Figure 5.7a and clearly demonstrate the effect rotational anisotropy has on the nonlinear optical response of the helices. Maxima in the SHG occur when linearly P-polarised light is incident on the helices. Minima in the SHG response are measured with incident RCP light. The maxima, or SHG "hot spots", are prominent for approximately half a sample rotation. For the other half of the sample rotation there is much less SHG at all incident polarisations. The variation of the SHG signal as the sample is rotated is due to the sample anisotropy. If the samples were rotationally isotropic then the SHG intensity would not vary as the sample is rotated. This particular anisotropy can be attributed to the direction in which the helix radiates SHG. The experiment is performed in reflection, therefore the tip of each helix points towards the direction of observation for half a sample revolution and hence SHG is detected. For the other half of the revolution the helix tip points away from the direction of observation and no signal is detected. To explain why incident P-polarised light produces greater SHG than incident CPL consider that, in the frame of reference of the sample, P-polarised light has a greater component of its electric field along the helical axis. It is potentially easier to drive electron motion along the length of the helix rather than electron motion across

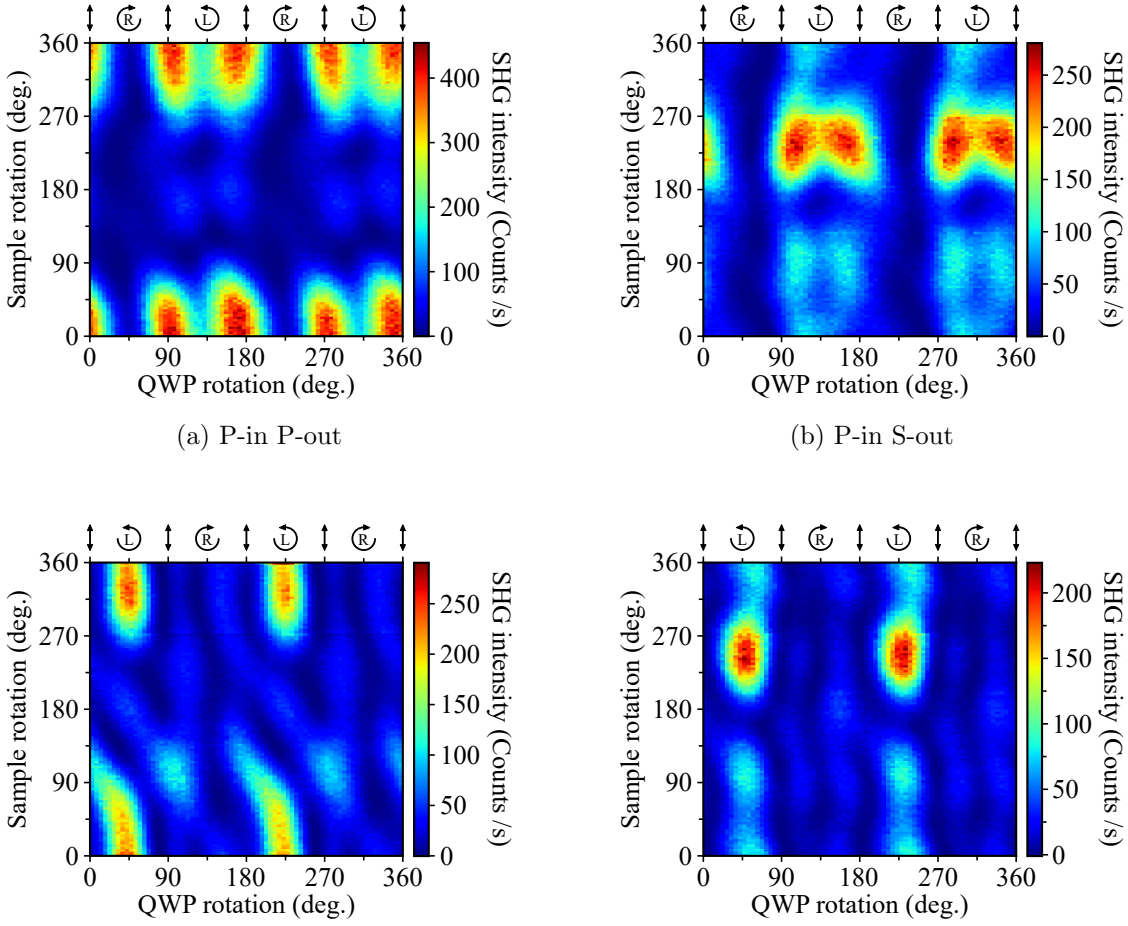

(a) P-in P-out

(b) P-in S-out

(c) S-in P-out

(d) S-in S-out

Figure 5.7: Continuous polarisation maps for the A-LH helices.

the diameter of the helix.

In the P-in S-out data, maxima in the SHG signal occur between 180° and 270° degrees of sample rotation. Similar to the P-in P-out data, the maxima appear for linearly polarised incident light. In the P-in S-out polariser-analyser configuration, SHG optical rotation (SHG-OR) can be identified. SHG-OR from the nanohelix arrays is presented and discussed in further detail by J. T. Collins in reference [127].

The chiral nature of the helices is apparent in the S-in P-out data, where strong SHG is recorded only for LCP incident light. The evolution of the signal as the sample is rotated is almost identical to that of the P-in P-out data. In terms of SHG intensity, S-polarised incident light elicits a much weaker SHG response from the helices, compared to P-polarised incident light. In turn, the SHG from incident CPL appears more prominent.

The prominence of the CPL induced SHG response is also seen in the S-in S-out data, where SHG peaks appear for LCP incident light and in the same sample rotation range as the SHG peak in the P-in S-out data.

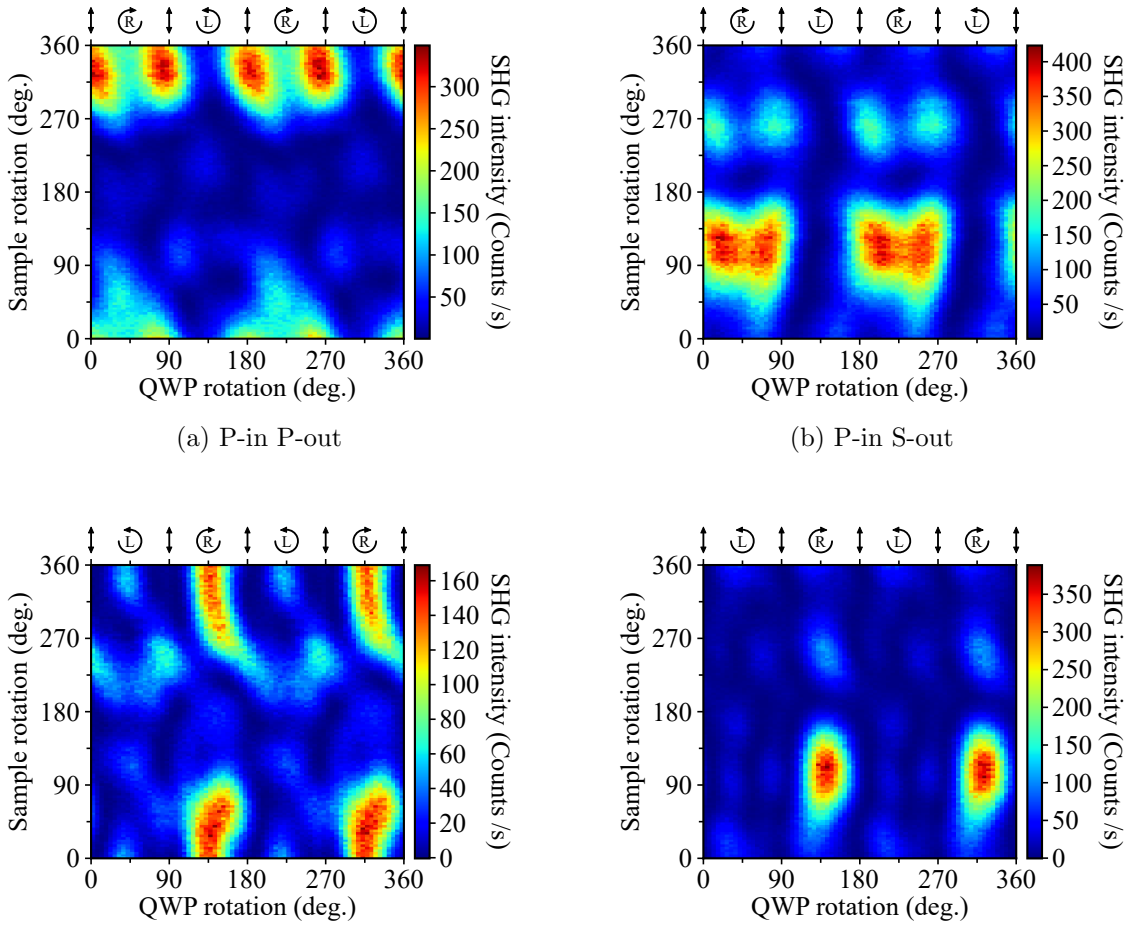

(a) P-in P-out

(b) P-in S-out

(c) S-in P-out

(d) S-in S-out

Figure 5.8: Continuous polarisation maps for the A-RH helices.

Data for the continuous-polarisation measurements of the right-handed A-series enantiomorph (A-RH), are shown in Figure 5.8. The SHG response of A-RH appears almost identical to SHG response of A-LH. Albeit, the response of A-RH is shifted in quarter-wave plate angle because of the opposite handedness of the helices. The opposite chirality of A-RH is evidenced in the P-in P-out and P-in S-out data, where the SHG maxima are centred around RCP incident light, rather than being centred around LCP incident light. Furthermore, in the P-in S-out data for A-RH the peaks are mirrored in sample rotation compared to A-LH. Similarly, in the S-in P-out and S-in S-out data the SHG

peaks occur for RCP incident light and, again, the trends are also mirrored in sample rotation compared to A-LH.

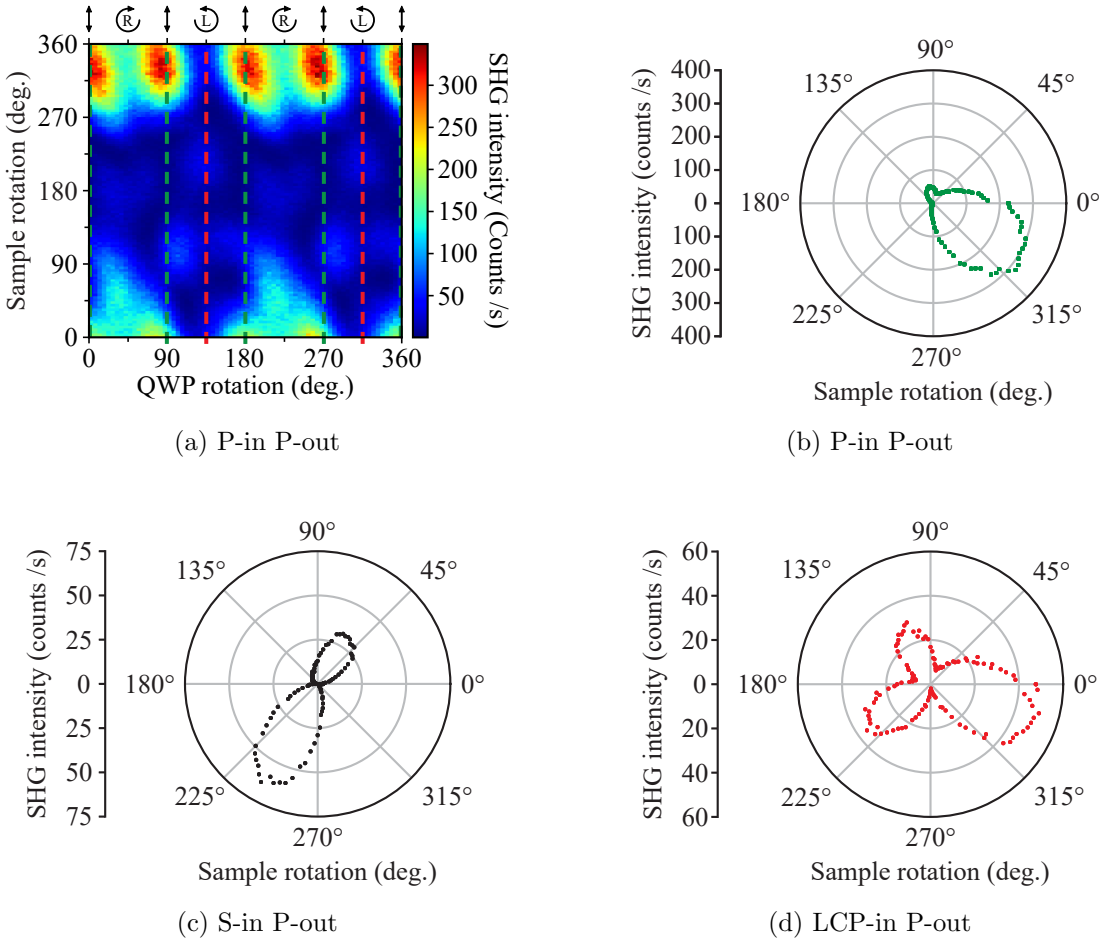

(a) P-in P-out

(b) P-in P-out

(c) S-in P-out

(d) LCP-in P-out

Figure 5.9: Analysis of symmetries the left-handed A-series nanohelices.

Greater insight into the nonlinear chiroptical behaviour of the helices can be gained by inspecting the rotational anisotropy at specific incident polarisations. Figure 5.9 a shows the P-in P-out data for the A-RH helices with coloured dashed lines, where each colour indicates an equivalent incident polarisation. The green dashed lines specify P-polarised light incident on the helices, the average of all the green dashed lines is shown in the polar plot where the azimuthal axis is sample rotation. and the radial axis is the SHG intensity. Here, the one-fold rotational anisotropy caused by the tip of the helices is clearly seen. The red dashed lines mark incident LCP light and the corresponding polar plot is shown in Figure 5.9d. When illuminated with LCP light, the SHG signal is significantly weaker compared to linearly polarised incident light, however, a three-fold symmetry is

revealed. This three-fold rotational symmetry arises because of the six-fold lattice of the helices, which is caused by the close packing of the micelles as described in Section 5.3.2. The symmetry of the lattice is visible because the incident LCP light does not couple well to the helical structures, and in turn, SHG due to the helicity does not dominate the signal, therefore allowing the lattice symmetry to be expressed. Finally, the S-in P-out polariser-analyser configuration displays a two-fold anisotropy, which is attributed to an electric dipole radiating from the tips of the helices. In both the three- and two-fold anisotropies one lobe is larger than the others. This discrepancy can be explained by either a superposition of the one-fold anisotropy onto the higher-order symmetries or by a preferential direction of radiation in the reflection geometry.

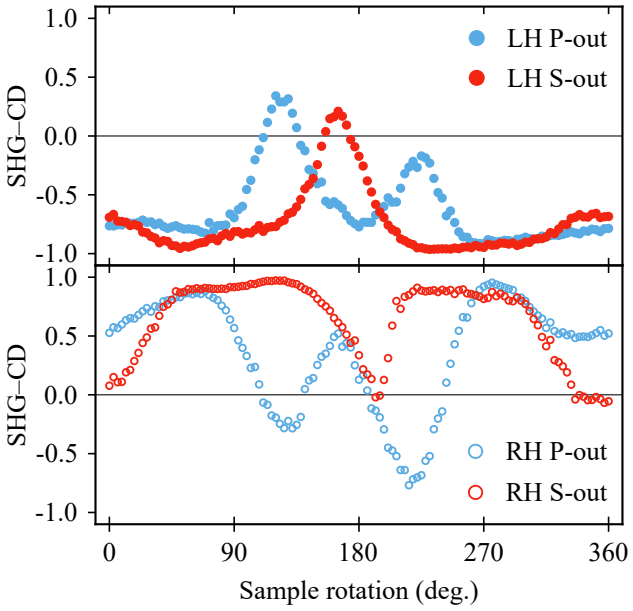

Figure 5.10: SHG-CD for the A-series helices. Top panel, left-handed enantiomer (solid circles). Bottom panel, right-handed enantiomer. The SHG-CD is decomposed into its P-polarised (blue markers) and S-polarised (red markers) components.

The SHG-CD for the A-series helices as a function of sample azimuthal angle is shown in Figure 5.10. The opposite chirality of the helices is apparent as their SHG-CD profiles are mirror images of each other. In general the handedness of a structure can be determined by the sign of its CD. However, as the helices are rotated their SHG-CD changes dramatically, even changing sign multiple times. Therefore, from the SHG-CD data alone, the handedness of the helices cannot be determined. This change of sign of the SHG-CD

cannot come from the intrinsic chirality of the helices, which does not change with orientation, but must be due to the anisotropies which are discussed earlier. The change in sign of the SHG-CD is important because it informs us that the SHG response arising from anisotropy induced chirality is greater than the SHG response due to intrinsic chirality. This data demonstrates that SHG-CD cannot be used to evaluate a metamaterial's nonlinear chiroptical response without taking into account sample orientation or considering other anisotropies.

It should also be noted that the SHG-CD data for left- and right-handed helices are not mirror images of each other. This is largely because the nanoscopic orientation of the helices is unknown. While the helical axis out of the substrate plane is easy to define, information about the direction in which all the helix tips are points is not known. The orientation of the helices is not recorded during fabrication and the scanning electron microscope facilities available were not powerful enough to resolve the wire thickness of the helices, or indeed individual helices. As a a result of the unknown orientation, the x-axis in the SHG-CD plots (sample rotation) has an arbitrary origin. In other words the data are in no way correlated in terms of x-axis position. Because the samples were rotated a full circle the data can be translated in the x-direction.

There are other possible explanations for the deviation of the SHG-CD data being mirrored between LH and RH helices. Firstly, each sample is fabricated independently and as a result the LH and RH helices will show slight differences, apart from the expected opposite handedness, due to fabrication imperfections and tolerances. An example of variation introduced by the fabrication method is that the helices only possess short range in the plane of the array. This arises from the spin coating of the nanoparticle seeds on the substrate. In the ideal case, the nanoparticle seeds will arrange with spherical close packing over the whole substrate leaving a hexagonal array of nanoparticles. However, in practice the spin coating results in nanoparticles with very weak and short range order as seen in Figure 5.4a. Because of this short range order we cannot know how well the helices in the beam spot were ordered.

We can speculate that another factor in determining the SHG-CD is due to the extrinsic chirality introduced by the experimental geometry. As discussed in Section 5.1.5 the

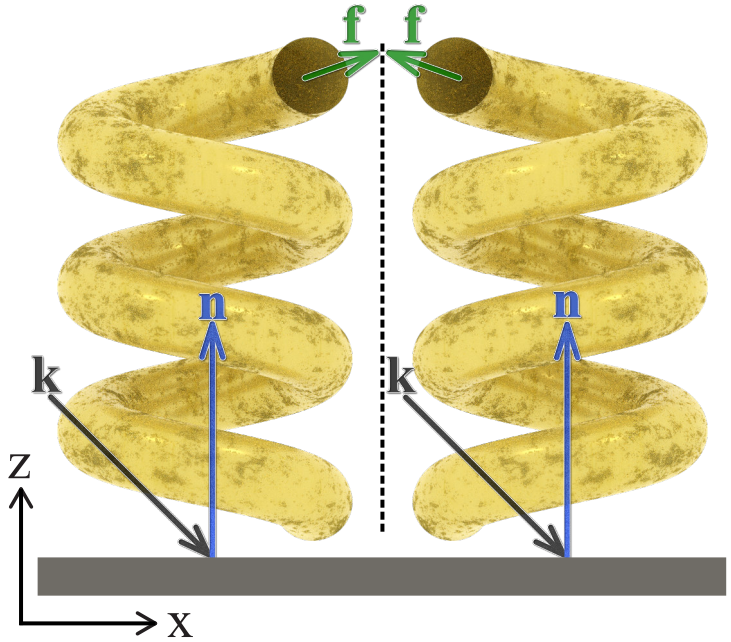

Figure 5.11: Illustration of extrinsic chirality introduced by the experimental geometry and curved tips of the helices.

geometry of an experiment can introduce a chiroptical response. While extrinsic chirality is usually used to obtain a chiroptical response from achiral structures, it can still contribute to the chiroptical response of anisotropic chiral structures. For example consider the tips of the helices as an exaggerated example of the tilted wires shown in Figure 5.1. However, in the case of the helices the wavevector and surface normal stay the same, it is only the helix that is mirrored. The tips of both LH and RH helices trace out the same circle as the sample is rotated. The direction of the tips, denoted by the green arrows in Figure 5.11, point in different directions for equivalent points on the tips circular path thus leading to extrinsic chirality.

5.4.2 B series nanohelices

The next set of helices investigated were the B-series, which were fabricated using micelles with a diameter of 74 nm and loaded with 14 nm diameter nanoparticles. As a result of the larger micelles and larger nanoparticle seeds, the fabricated B-series helices also possess a larger diameter and wire diameter. The nominal fabrication parameters of thickness(height) and pitch of the B-series were identical to the A-series. The measured dimensions of height, 81 nm, and pitch, 34 nm, are comparable to the A-series helices,

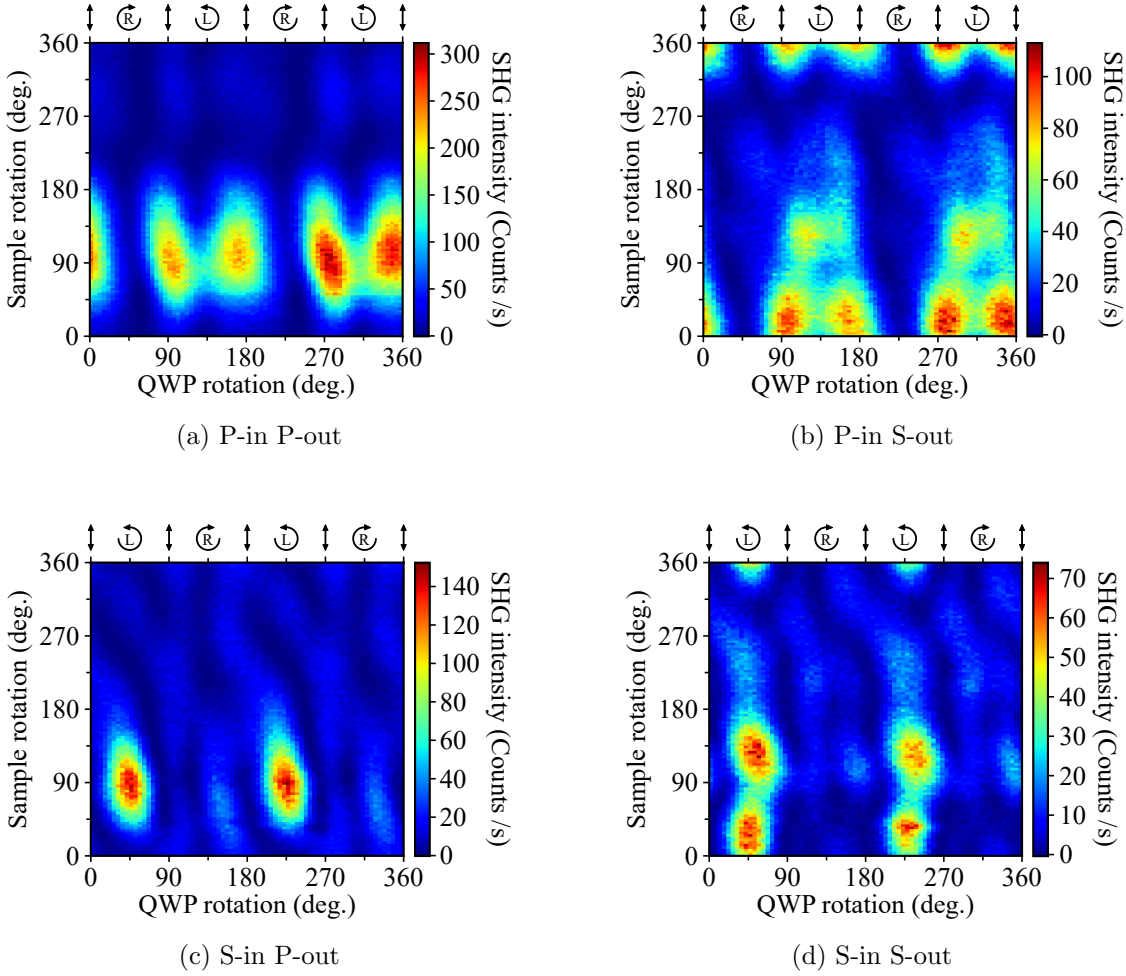

(a) P-in P-out

(b) P-in S-out

(c) S-in P-out

(d) S-in S-out

Figure 5.12: Polarisation-anisotropy maps for B-LH helices.

which is expected because the nominal fabrication parameters are identical. Using the measured height and pitch, each helix has approximately 2.4 turns. Previous linear optical characterisations of helices have shown that changing the seed spacing does not affect greatly affect the plasmonic behaviour of the helices. However, those investigations also demonstrated greatly reduced linear CD for helices fabricated with seed spacings > 60 nm.

The continuous-polarisation measurement data for the left-handed B-series sample (B-LH) are shown in Figure 5.12. In terms of recorded SHG intensity, for B-LH is lower in all plots compared to A-LH. The reduction in SHG intensity can be partially explained by fewer helices being illuminated by the laser spot because of the helices larger diameter. The P-in data for B-LH have the same key features as the A-LH P-in data. That is,

the response of both samples exhibit regions of relatively strong SHG when incident with P-polarised light. While the S-in data for B-LH shows similar behaviour to A-LH, there are notable differences. Firstly, the S-in P-out data for both B-LH and A-LH display peaks for incident LCP light, however, B-LH's response is much more confined in sample rotation. Secondly, there is an additional peak in the S-in S-out data of B-LH, whereas for A-LH there is only a single strong peak.

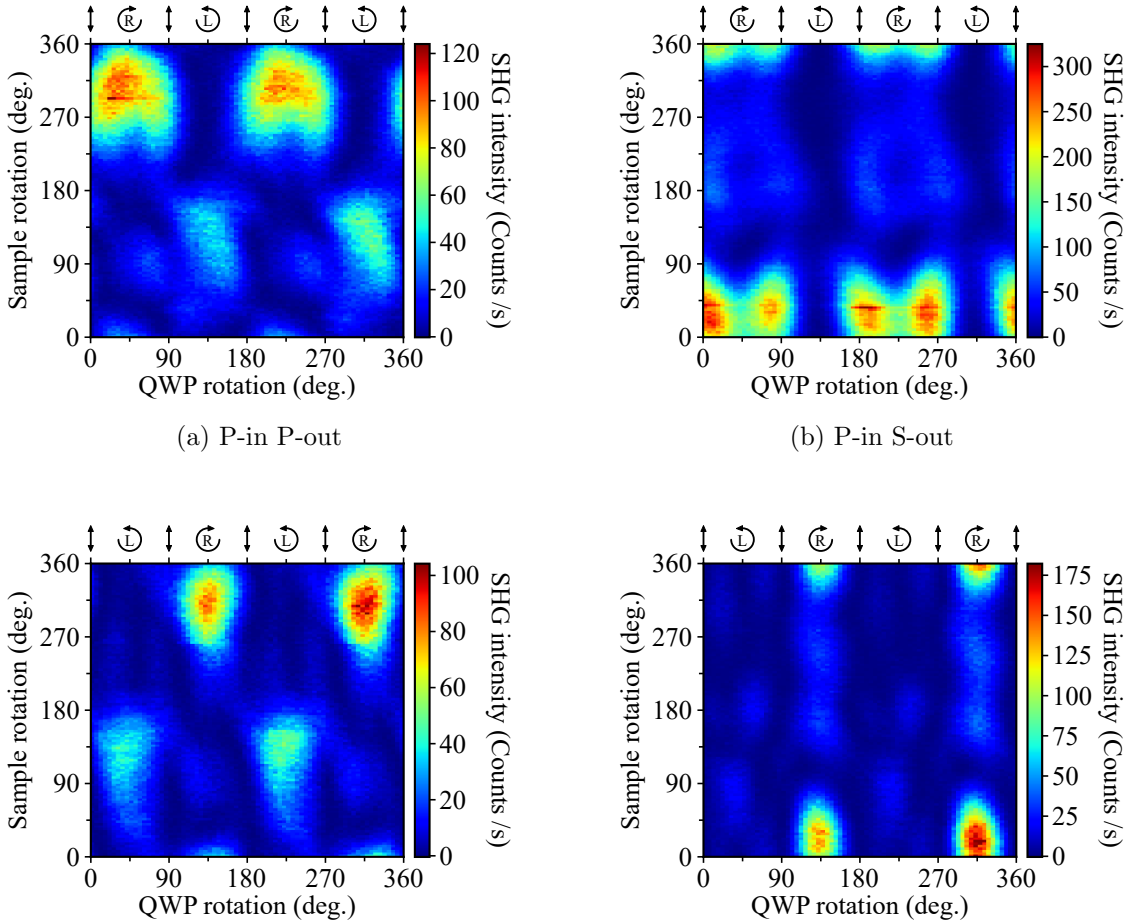

(a) P-in P-out

(b) P-in S-out

(c) S-in P-out

(d) S-in S-out

Figure 5.13: Polarisation-anisotropy maps for B-RH helices.

Experimental data for the right-handed B-series (B-RH) helices are given in Figure 5.13. Compared to A-RH, the nonlinear optical response of B-RH is reduced in intensity. In the P-in P-out data there is an SHG peak for incident RCP light. However, while B-RH shows a single peak centred on RCP, A-RH displays two distinct peaks centred on linearly polarised light. For the P-in S-out data, the strongest SHG regions are more localised to

linearly polarised light and no weaker secondary peaks appear, compared to A-RH. The changes seen in the B-RH S-in P-out data are similar to the changes observed between A-LH and B-LH. In the S-in P-out configuration, the SHG response of B-RH is more localised in terms of sample rotation compared to A-RH. Additionally, weak secondary peaks occur between 90° and 135° sample rotation for incident LCP light. These secondary peaks are also seen in the Pin P-out data for B-RH because the incident polarisation and analyser configuration are equivalent. No drastic changes are noticeable between A-RH and B-RH for the S-in S-out map.

The SHG-CD as a function of sample rotation for the B-series helices is shown in Figure 5.14. The SHG-CD response of B-LH follows the same trend as A-LH. Both left-handed samples present a predominately negative SHG-CD for both P- and S-polarised components. The negative SHG-CD correlates with the strong SHG response when the left-handed helices are incident with LCP light. The P-polarised SHG-CD component of B-LH displays two regions where it changes sign and becomes positive, whereas the S-out component only has one peak that changes sign. The B-RH P-out SHG-CD is negative for approximately half a sample rotation and positive for the other half. This trend for the B-RH P-out data results in two crossing points, this is in comparison to the four crossing points seen in the P-out SHG-CD for A-RH. The B-RH S-out SHG-CD also has two crossing points, changing from approximately 1 at its maximum to -0.6 at its minimum. This reversal is much more distinct compared to the change from 1 to -0.1 for the A-RH S-out SHG-CD.

Overall the differences in SHG-CD between the the A-LH and B-LH helices are minor. On the other hand, a more dramatic difference is observed between the right-handed helices A-RH and B-RH. These differences are apparent by the secondary SHG peaks in the B-RH P-out data at LCP. The difference in SHG-CD for the right-handed helices may be caused by extrinsic chirality introduced by the experimental geometry. It can be speculated that the handedness of the extrinsic chirality will more greatly affect the chiroptical response of one handedness of helices compared to the other. Just as one handedness of CPL produces a different SHG response in each enantiomorph, because of two chiral systems interacting, the handedness of the experiment could elicit a different responses from the

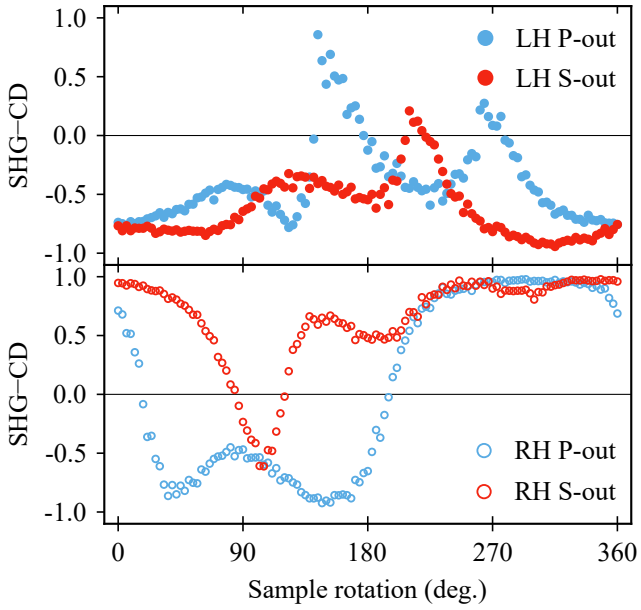

Figure 5.14: SHG-CD for the B-series helices. Top panel, left-handed enantiomer (solid circles). Bottom panel, right-handed enantiomer. The SHG-CD is decomposed into its P-polarised (blue markers) and S-polarised (red markers) components.

helices which is revealed through the SHG-CD measurements. To test this hypothesis the experimental geometry could be mirrored, producing the opposite handedness experiment, and the helices measured again.

The major physical differences between the A- and B-series helices are their diameter and wire thickness. The SHG response of both sets of helices are very similar, as seen from the continuous polarisation measurements. Changing the diameter and wire thickness of the helices did not cause drastic new features to appear in their SHG responses. A possible explanation for the similarity in the results may be because parameters such as the pitch, height, and number of turns play more important roles in determining the nonlinear chiroptical responses from nanohelices. This is a reasonable explanation because parameters such as helical pitch and number of turns are more closely related to geometrical chirality.

Furthermore, the variations introduced because of fabrication tolerances cannot be ignored. Firstly, spin coating the gold nanoparticle seeds is a random process, creating only small areas with short range structure. The uniformity of the nanoparticle spin coating over the whole wafer/sample is not known. Additionally, each sample is created in a separate run of the evaporation chamber introducing variations between samples. These

variations can be seen in the pitch of the A- and B-series helices. The nominal fabrication pitch for both series was set to a magnitude of 250 nm, however the measured pitches were 37 and 34 nm for the A- and B-series, respectively.

5.4.3 C series nanohelices

The final set of helices studied were the C-series, with a measured height of 122 nm and a pitch of approximately 50 nm. These dimensions mean that the C-series helices are significantly taller. However, the number of turns for the C-series helices is approximately 2.4, which remains similar to the 2.2 and 2.4 turns for the A- and B-series, respectively. The C series have an array spacing of 79 nm, which is only marginally larger than the 74 nm of the B series. The left- and right-handed C-series helices were fabricated with 14 nm and 11 nm nanoparticle seeds, respectively. The C-series helices have a greater pitch and height compared to the A- and B-series helices. Previous investigations show that increasing the pitch of the helices red shifts the maximum linear CD.[116] Additionally, it would be expected that any plasmon resonance would be red shifted due the larger size of the C-series helices.

Experimental data for the left-handed C-series (C-LH) helices are presented in Figure 5.15. The most immediate difference is that the overall SHG intensity for C-LH is higher than either the A- or B-series. The increased height of the C-series helices could play a role in the increased SHG intensity. A taller helix has a greater surface area from which surface SHG emission can occur, thereby explaining the stronger SHG response. The second prominent difference is that the SHG response of C-LH exhibits more fine structure compared to the responses of A- and B-series helices. For example, the P-in data show stronger secondary peaks for linearly polarised incident light. Furthermore, the S-in data show that C-LH interacts with both and left- and right-handed CPL, although the strongest response is obtained with LCP illumination. Determining the handedness of C-LH is not as clear compared to using the S-in data to determine the handedness of the A- and B-series samples.

The SHG response of the right-handed C-series (C-RH) helices presents an even richer behaviour as shown in Figure 5.16. For the P-in P-out measurement the highest intensity

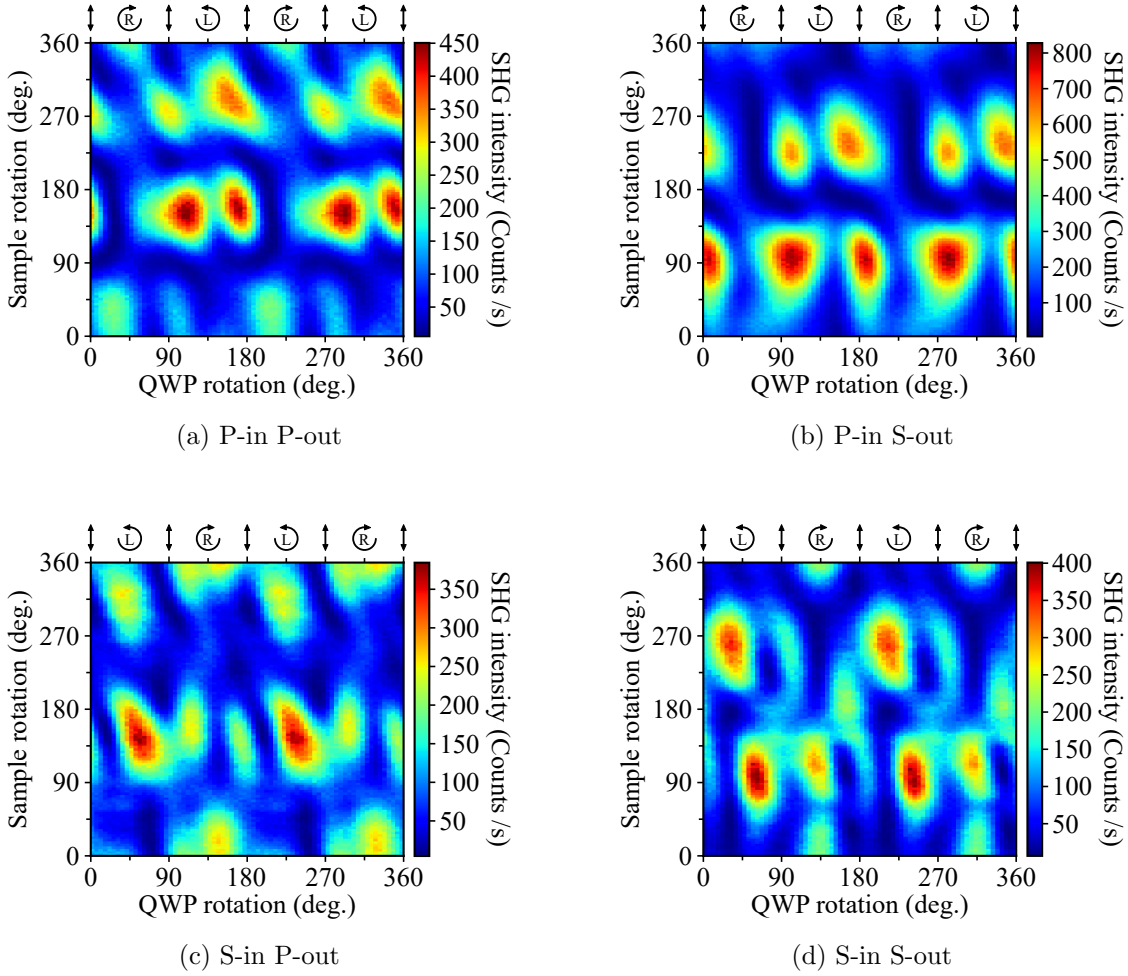

(a) P-in P-out

(b) P-in S-out

(c) S-in P-out

(d) S-in S-out

Figure 5.15: Polarisation-anisotropy maps for C-LH helices

SHG is obtained with elliptically polarised light, rather than linearly polarised light as observed with all the previous samples. Additionally, C-RH responds to both handednesses of CPL to produce SHG, a behaviour not observed in the P-in P-out data for the other helices. Features seen in the P-in S-out data are comparable to C-LH. Again, similar to C-LH, the S-in data display a more complex behaviour and produces SHG for both LCP and RCP light. On other hand, the S-in data for C-RH demonstrate a drastically different behaviour compared to C-LH. The discrepancy in nanoparticle seed size between the two C-series samples could explain these drastic differences.

The SHG-CD of the C-series nanohelices is plotted in Figure 5.17. For C-LH, the SHG-CD behaves in a similar manner to A-LH and B-LH, whereby the P-polarised component of SHG-CD changes sign four times over a single sample rotation. The S-polarised component

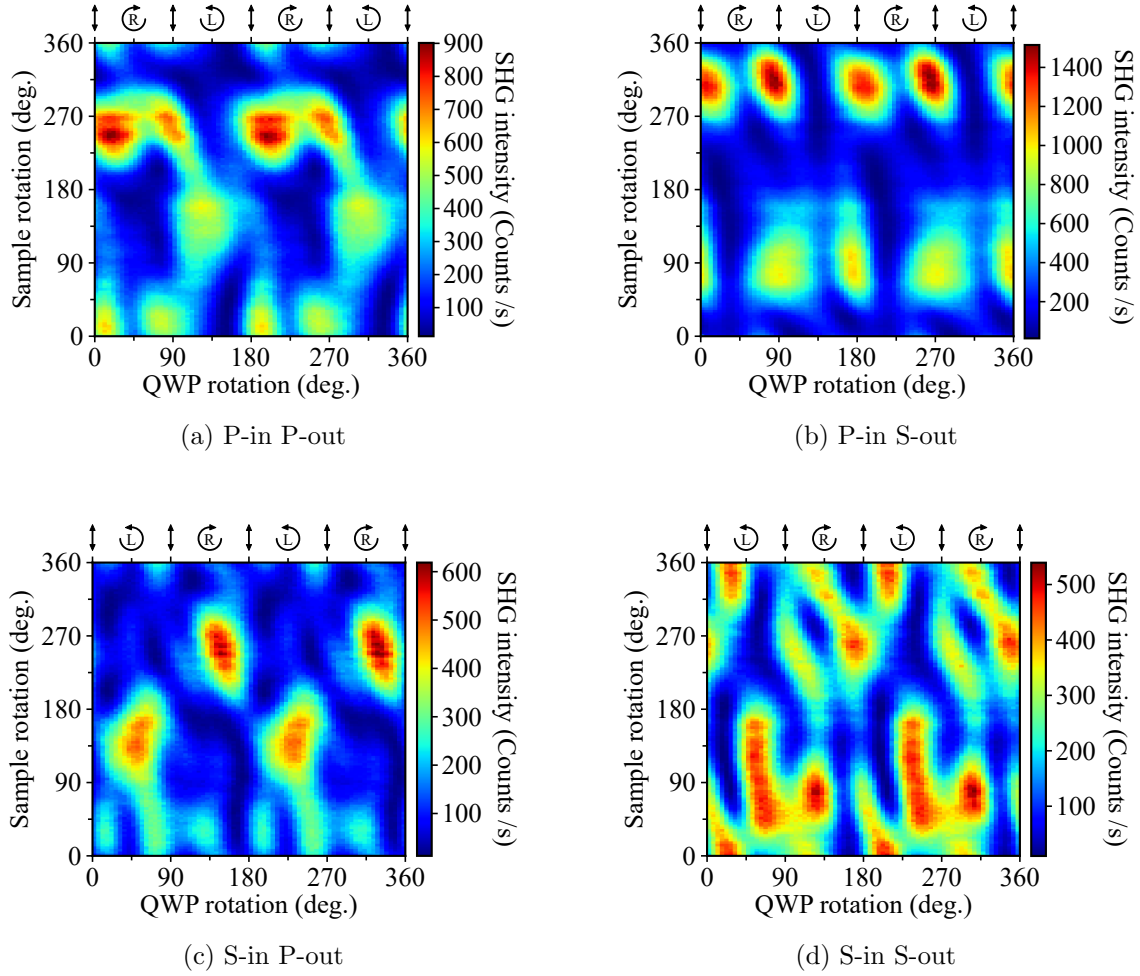

(a) P-in P-out

(b) P-in S-out

(c) S-in P-out

(d) S-in S-out

Figure 5.16: Polarisation-anisotropy maps for C-RH helices.

of SHG-CD also has four crossing points where it changes sign, compared to the two crossing points seen for A-LH and B-LH.

In comparison, the SHG-CD of C-RH does not resemble the SHG-CD trends of either A-RH or B-RH. The P-polarised component of SHG-CD changes sign twice, just as B-RH. It is not possible to make any meaningful comparison between the S-polarised component of SHG-CD of C-RH and the other samples. Indeed, the C-series helices are not perfect enantiomorphs, as their SHG-CD trends are not mirrored. The difference in the nanoparticle seed size between C-LH and C-RH is only 3 nm but it appears to strongly affect the helices SHG response.

Considering that the A- and C-series do not share any similarities in physical dimensions we would not expect them to exhibit similar SHG behaviour, and this is true com-

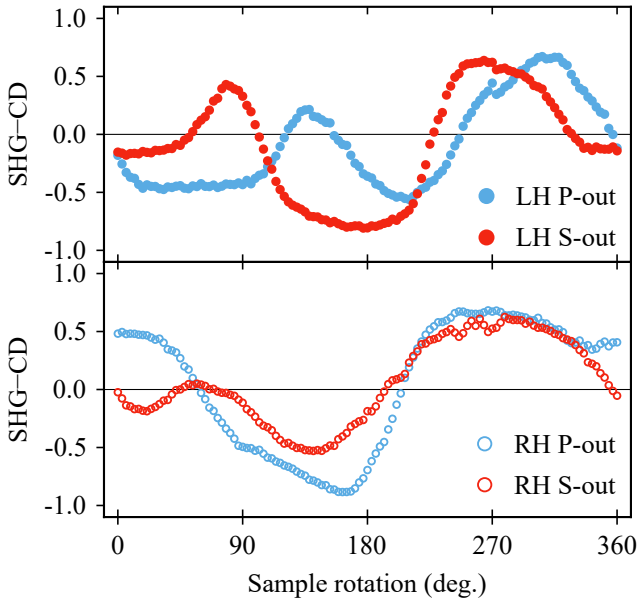

Figure 5.17: SHG-CD for the C-series helices. Top panel, left-handed enantiomer (solid circles). Bottom panel, right-handed enantiomer. The SHG-CD is decomposed into its P-polarised (blue markers) and S-polarised (red markers) components.

paring the polarisation-anisotropy measurements and SHG-CD. However, the nanoparticle seed size and wire thickness of the B- and C-series are similar, yet there is little resemblance between their measured SHG responses. Indeed, the number of turns of each series of helices lies between 2.2 and 2.5 and while the difference between the A- and B-series in minimal, the C-series is drastically different. These differences suggest that the number of turns does not radically alter the SHG response of the helices. Finally this leaves the height of the helices to be examined. The A- and B-series helices possess the same measured height of 81 nm while the C-series have a height of 122 nm, which is 50% taller. At a height of 81 nm the A- and B-series can be considered extremely subwavelength because their height is $\sim \frac{\lambda}{10}$ which means that the helices can be treated as an effective medium. On the other hand, the greater height of the C-series helices may be enough such that the helices can no longer be treated as an effective medium. This transition away from an effective medium could be investigated by fabricating and measuring the SHG response of a series of helices with increasing height. Such an investigation is realistic because the height of the helices is relatively easy to control during the fabrication process.

5.5 Conclusion

The effect of rotational anisotropy on the second harmonic generation response of nanohelix arrays has been investigated. Three pairs of enantiomorphs with varying dimensions were studied using continuous polarisation measurements.

To reveal how the SHG response of each sample depends on sample rotation the experimental data were plotted as heat maps. Inspecting the heat maps shows which incident polarisations and sample rotation angles produce the strongest SHG response. The contributions to the SHG response from different geometrical aspects and symmetries were determined by examining rotational anisotropy at specific configurations of incident polarisation and decomposed SHG signal.

The impact of rotational anisotropy on the SHG-CD response of the nanohelices was also studied. It was observed that the P- and S-polarised components of the SHG-CD change sign for all of the samples studied. The observed change in sign of the SHG-CD clearly demonstrates the difficulties of quantifying the nonlinear chirality of anisotropic systems. Therefore, any quantification of the nonlinear chirality needs to carefully take into account any anisotropy that a sample presents. It can be envisioned that the large data sets produced by continuous-polarisation measurements along with sample rotation can be used to link different symmetries to the nonlinear chiroptical response. Having knowledge of how different symmetries and structures affect the nonlinear chiroptical response would allow for the optimisation and engineering of nonlinear chiroptical nanophotonic platforms.

Furthermore, it is reasonable to assume that the experimental geometry introduces extrinsic chirality, which further complicates the anisotropy of the helices' SHG response. Extrinsic chirality may explain why the SHG-CD measurements of each series of helices are not mirror images of one another. The effect of extrinsic chirality can be tested by mirroring the experimental geometry in order to flip the triad of vectors formed by the incident wavevector, surface normal, and helices.

In terms of how the physical dimensions affect the SHG response of the helices, we have seen that varying the helices' diameter and wire thickness does not appear to greatly alter the response, as seen from comparing the A- and B-series measurements. This weak dependence on helix diameter and wire thickness could be because the change was

relatively small. Both the A- and B-series helices are much smaller than the wavelength of the fundamental, in all dimensions, meaning they can be treated as effective media.

Then with the C-series helices we have seen how increasing the helix hight can greatly affect their SHG response. I speculate that this is because the height of the C-series helices means they can no longer be treated as an effective medium and the response of each helix has an increased effect compared to that of the ensemble. This result highlights the difficulty of working with nanoscale media and designating at which point they act as an effective media or simply act an array of antennae.

Future work would benefit from measuring nanostructures with higher symmetry arranged in various lattices. Choosing structures with higher symmetry would make it easier to identify the different contributions to the SHG response. Then, fabricating the same nanostructures but arranged in a different lattice would allow one to study the interplay between the symmetry of the individual nanostructures and the lattice. A further extension would be to increase the scale of the unit cell of these new structures in order to investigate the transition from a system described as a homogeneous medium to that of a system described as an array of antenna.

Another avenue of focus for future work would be to quantify elements in the nonlinear susceptibility tensor. Extracting values for the tensor elements could be achieved by performing a simultaneous fitting on all of the data collected for a sample. The free coefficients of such a fit would be the tensor elements, which would have to be linked across all data sets of the sample. To accurately model the data would require the correct choice of which multipolar contributions to include in the fitting function. However, including extra terms in the model may result in overfitting, especially if the structure possesses low symmetry and hence many independent tensor elements. To help mitigate the possibility of overfitting, the data and fittings could be compared to numerical simulations.

In conclusion, sample anisotropy can dramatically affect the nonlinear chiroptical response of chiral nanostructures. The engineering and optimisation of nonlinear chiral nanomaterials would greatly benefit from design rules based on the physical processes that give rise to the desired nonlinear chiroptical effect, rather than using the chiroptical effect itself as the benchmark. Future work should focus on determining design rules

based on structure symmetry and scale in order to provide the means for delivering on the promises of chiral nonlinear nanomaterials.

Chapter 6

SHG enhanced by surface lattice resonances

Sections of this chapter have been copied verbatim from the published manuscript "*Second harmonic spectroscopy of surface lattice resonances*", David C. Hooper et al., 2019. The work was performed in collaboration with members from the Teri Odom group at Northwestern University, United States. All samples were fabricated by D. Wang, W. Wang, and, J. Guan at Northwestern University, United States. Numerical simulations were performed by D. Wang and C. Kuppe. Linear and nonlinear optical experiments were performed by myself. The data was analysed by myself. The first draft of the manuscript was produced by myself and V. K. Valev.

In Chapter 3 it was discussed how the plasmonic behaviour of individual nanoparticles and how the localised surface plasmon resonance (LSPR) enhances the local electric fields around the surface of the nanoparticle. To further enhance local fields multiple palsmonic nanoparticles can be arranged into assemblies that take advantage of near-field coupling. These assemblies can include dimers, oligomers and, clusters, with their properties being determined by the near-field coupling between constituent nanoparticles. Fabricating such assemblies requires the constituent elements to be placed extremely close together in order for their near-fields to couple. However, near-field coupling is not the only mechanism by which nanoparticles can interact. For example, plasmonic nanoparticles arranged in a regular array with a periodicity similar to the wavelength of visible light results in diffraction.

At normal incidence a specific wavelength diffracts at an angle of 90°, travelling along the plane of the array. This phenomenon is known as a Rayleigh anomaly and allows radiative coupling between nanoparticles in the lattice. Diffractive radiative coupling has a much greater range compared to the near-field coupling of LSPRs. Furthermore, the wavelength which undergoes a Rayleigh anomaly can be tuned by changing the angle of incidence. By judicious design of the nanoparticles and select choice of the lattice periodicity, the wavelengths of the LSPR and Rayleigh anomaly can be made to coincide. In this case, the diffracted beam of the Rayleigh anomaly interacts with multiple nanoparticles and acts to reinforce the LSPR leading to a collective response named a *surface lattice resonance* (SLR). In this chapter we examine how the electric near-field enhancements provided by surface lattice resonances in nanoparticle arrays leads to enhanced second harmonic generation (SHG). Additionally, the ability to select the Rayleigh anomaly wavelength and hence the SLR leads to a tunable enhancement of SHG.

6.1 Introduction

Recently, nonlinear plasmonics has attracted significant research interest,[128, 129] because nonlinear optical effects scale as a power law of the incident light and plasmonic nanostructures strongly concentrate the incident light into optical near-field "hotspots". As a consequence, within such hotspots, nonlinear plasmonic effects are tremendously enlarged, offering prospects for new and improved applications.

Because nonlinear optical effects find applications in tuning laser light, significant research interest has been devoted to plasmon-enhanced frequency conversion, with increasing efficiency.[130, 131] Nonlinear optical effects also find applications in multiphoton microscopy, useful for biological sciences and material characterisation.[132] Plasmonic nanoparticles have thus been the subject of numerous investigations with second harmonic generation (SHG),[133–135] third harmonic generation,[136, 137] and two-photon luminescence microscopy, to name just a few. Due to the frequency conversion, the measured signal in all these techniques is background free (from the illumination). The improved frequency conversion offered by plasmons can allow imaging with lower laser power and reduced photodamage to specimens (organic or inorganic).[138, 139] The absence of

signal background is also a key factor for the strong sensitivity of nonlinear optical effects, such as SHG chiral optical effects,[40, 90, 93, 140] or magnetisation-induced SHG,[141, 142] compared to their linear optical counterparts.[120] Though considerable attention has been devoted to the SHG enhancements from localized surface plasmons (LSPR) and metasurfaces,[103, 143–148] surface lattice resonances (SLR) [149–153] have received much less consideration.[154, 155]

SLRs are more promising for sensing applications than LSPRs because of their significantly narrower resonance linewidth (< 5 nm).[151, 156–158] Since the resonance wavelength depends on the refractive index of the environment,[159] surface plasmons can be used for chemical and biological sensing, in both liquid and gaseous media. The usefulness of a plasmonic resonance for sensing can be quantified by a figure of merit (FoM). The FoM is defined as FoM $= \frac{\partial\lambda}{\partial n \Delta\lambda}$, where $\frac{\partial\lambda}{\partial n}$ is the wavelength shift of the resoance due to a change in refective index and $\Delta\lambda$ is the full width half maximum of the resonance. Therefore, a broad resonace needs a large shift in wavelength in response to a change in the surrounding refractive index to be useful for sensing. On the other hand, a very sharp resoance needs only to shift a little in response to refractive index changes to be useful for sensing. While the FoM for LSPRs is typically on the order of a few units, for SLRs it is much larger,[160, 161] (by one[162] and even two[163] orders of magnitude) and the narrower resonance linewidth is attributed to a Fano-type effect.[164] SLRs occur on plasmonic nanoparticles, arranged periodically, with a lattice constant of the order of the wavelength of incident light. The two determining factors for the SLR are the LSPR and the Rayleigh Anomaly (where light is diffracted in the plane of the array).[164–166] Specifically, the SLRs result from the coupling of the broad LSPR with the narrow frequency of the Rayleigh Anomaly, and hence exhibit a dual sensitivity – surface (on the nanoparticles) and bulk (between the nanoparticles).[167]

Here, SHG spectroscopy of SLRs is demonstrated, where the SHG signal is enhanced up to 450 times by SLRs; much greater than the previous reports of 10 and 30 times increase.[154, 155] The measured SHG resonances can be as sharp as 5 nm in FWHM, which is promising for sensing. Indeed, the SHG signal is shown to be very sensitive to the factors determining SLRs; the SHG is successfully tuned by varying the fundamental wavelength,

the angle of incidence, the lattice parameter and the nanoparticle material. Importantly, SHG spectroscopy resonances are discovered that are not associated with electric dipoles. These dipole-forbidden resonances are attributed to higher-order contributions, enhanced by the SLRs. For individual nanoparticles with diameter $>$ 100 nm, retardation effects lead to higher-order terms (quadrupoles,[168] octupoles, etc.[169–172]), at the second harmonic frequency.[173, 174] Whereas in previous decades, such higher-order contributions did not play a major role in material properties, recent progress in nanofabrication has pushed them to the forefront of nonlinear plasmonics.[175, 176]

6.2 Rayleigh anomalies

For a Rayleigh anomaly to occur the in-plane component of the incident wave vector is required to be supplemented by the reciprocal lattice vectors in order for the diffracted beam to scatter in the plane. The condition for this requirement is given by,

$$\mathbf{k'} = \mathbf{k_{inc\parallel}} + \mathbf{G}, \tag{6.1}$$

where $\mathbf{k'}$ is the wave vector of the diffracted beam . $\mathbf{k_{inc\parallel}}$ is the in-plane wave vector component of the incident beam. $\mathbf{G}$ is the sum of the reciprocal lattice vectors. For a two-dimensional grating, $\mathbf{G} = \alpha\mathbf{a}^* + \beta\mathbf{b}^*$ where $\mathbf{a}^*$ and $\mathbf{b}^*$ are the reciprocal lattice vectors and α and β are integers. To find the in-plane component of the incident wave vector, consider the general case shown in Figure 6.1, where z lies along the grating normal, θ is the polar angle and, ϕ is the azimuthal angle. The momentum matching condition in Equation 6.1 can now be expanded to give,

$$\mathbf{k'} = \mathbf{k_{inc}}\sin(\theta)\sin(\phi) + \beta\mathbf{b}^* + \mathbf{k_{inc}}\sin(\theta)\cos(\phi) + \alpha\mathbf{a}^*. \tag{6.2}$$

First, we restrict our analysis to a two-dimensional square lattice with the lattice vectors along the x and y axes. Using Equation 6.2 we can plot the Rayleigh anomaly dispersion, when different incident wavelengths undergo a Rayleigh anomaly as a function of the angle of incidence, θ, and azimuthal angle, ϕ. The Rayleigh anomaly dispersion of two lattices with periodicities of 580 nm and 600 nm at different azimuthal angles

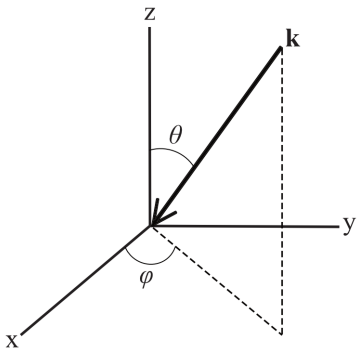

Figure 6.1: Decomposing the wave vector **k** into the xy plane of the sample.

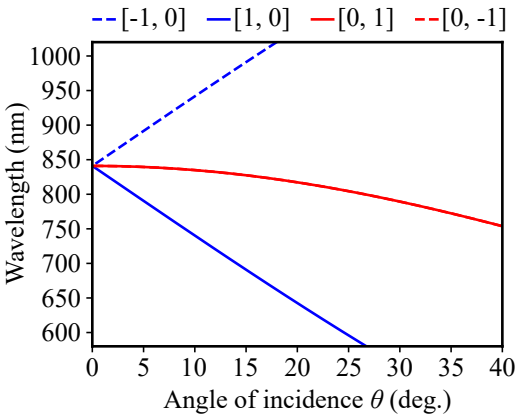

(a) 580 nm periodicity, $\phi = 0°$

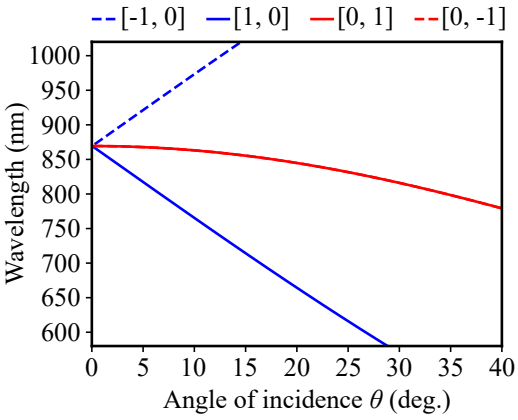

(b) 600 nm periodicity, $\phi = 0°$

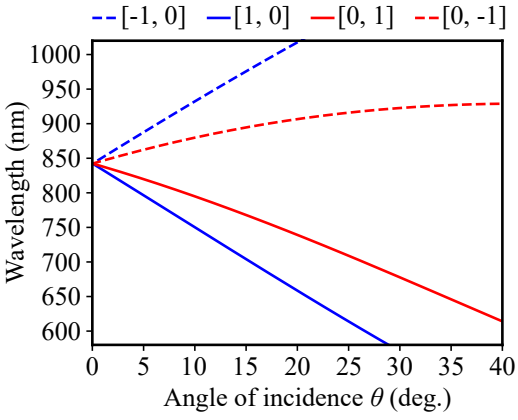

(c) 580 nm periodicity, $\phi = 50°$

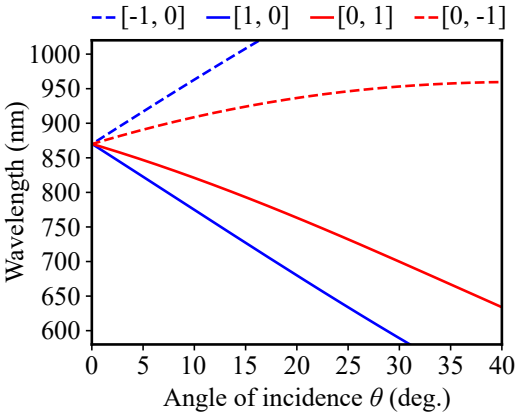

(d) 600 nm periodicity, $\phi = 50°$

Figure 6.2: Calculated Rayleigh anomaly dispersion for nanoparticle arrays with periodicities 580 nm (a,c) and, 600nm (b,d), with azimuthal angle $\phi = 0°$ (a,b) and, at $\phi = 50°$ (c,d). The refractive index of the surrounding media is set to 1.46. The top legends show the diffraction orders [x,y].

(equivalent to rotating the grating around the normal) are shown in Figure 6.2. The refractive index of the surrounding environment of the lattices is set to a constant of 1.46. Each dispersion line corresponds to a diffraction order which is related to the integers α and β in Equation 6.1. In Figures 6.2a and 6.2b we can see that when $\phi = 0°$ the $[0, 1]$ and $[0, -1]$ diffraction orders are degenerate and that by introducing an azimuthal angle to the incident wave vector the degeneracy is lifted, as seen in Figures 6.2c and 6.2d. At normal incidence the wavelength of the Rayleigh anomaly is determined by the lattice periodicity and the refractive index of the surrounding environment. The former dependency can be seen by comparing the y-intercept in Figures 6.2a and 6.2b where only the lattice periodicity has changed, resulting in normal incidence Rayleigh anomaly wavelengths of 840 nm and 872 nm for the 580 nm and 600 nm period lattices, respectively.

By changing the lattice parameters and refractive index of the surrounding environment the Rayleigh anomaly dispersion of a grating can be engineered. Furthermore, a specific Rayleigh anomaly wavelength can be targeted by controlling the angles at which the incident beam strikes the grating. This ability to target a Rayleigh anomaly wavelength is utilised later in this chapter in order to selectively enhance second harmonic generation from nanoparticle arrays.

6.3 Surface lattice resonances

The response of gratings formed by arrays of nanoparticles can be described by the the coupled dipole approximation (CDA).[153] In the CDA a polarisation is induced in each nanoparticle given by $\mathbf{P}_i = \alpha_i \mathbf{E}_{\mathrm{loc},i}$, where α_i is the polarisability of the nanoparticle and, $\mathbf{E}_{\mathrm{loc},i}$ is the local electric field at the position of the nanoparticle.[164] The local electric field is obtained by the addition of the incident electric field and the sum of retarded dipole fields produced by the other nanoparticles in the array.

Assuming that the polarisation of each nanoparticle in the array is identical allows a modified nanoparticle polarisability to be written,[152]

$$\alpha^{\mathrm{mod}} = \frac{1}{\alpha_{\mathrm{NP}}^{-1} - S}, \tag{6.3}$$

where α_{NP} is the polarisability of an isolated nanoparticle and S is a retarded dipole sum often referred to as the array factor, because it takes into account the geometry of the array. When the real parts of $\alpha_{\mathrm{NP}}^{-1}$ and S are equal, the real part of the denominator in Equation 6.3 becomes small and hence α^{mod} becomes large. This means that the polarisability of each nanoparticle in the array is large. The condition that $\alpha_{\mathrm{NP}}^{-1}$ and S are comparable occurs when diffracted beams travel across the plane of the array which allows S to become large in comparison to $\alpha_{\mathrm{NP}}^{-1}$. Such a condition is met with a Rayleigh anomaly.

Surface lattice resonances are characterised by narrow dips in the transmission of a grating. The SLR is dependent on the geometrical parameters of the array, as well as the properties of the individual nanoparticles. These extra degrees of freedom allow the position and width of the SLR to be engineered. The extra degrees of freedom in design are advantageous when compared to using the resonance of single nanoparticles which are much broader and are strongly dependent on material choice. The small FWHM of SLRs means they posses a high quality factors, of upto $Q = 200$,[153] which has been utilised for sensing applications.[177][162]

6.4 Second harmonic spectroscopy of surface lattice resonances

6.4.1 Array specifications and linear characterisation

Initially, nanoparticle arrays whose linear optical properties are described well by the coupled dipole approximation were investigated. Four such samples were investigated. The arrays were made of gold and silver plasmonic nanoparticles arranged in a square lattice. Two lattice periods, 580 nm and 600 nm, were chosen so that the SLRs could be excited by the laser system. The gold nanoparticle discs/cylinders have a diameter of 120 nm and a height of 50 nm, while the silver discs have a diameter of 130 nm and a height of 50 nm. The arrays were prepared on fused silica substrates (n=1.46) and a 150 nm thick film of SU8 polymer (n=1.48, from MicroChem) was spin-coated on top of the arrays, to provide a uniform refractive index environment around the nanoparticles. The

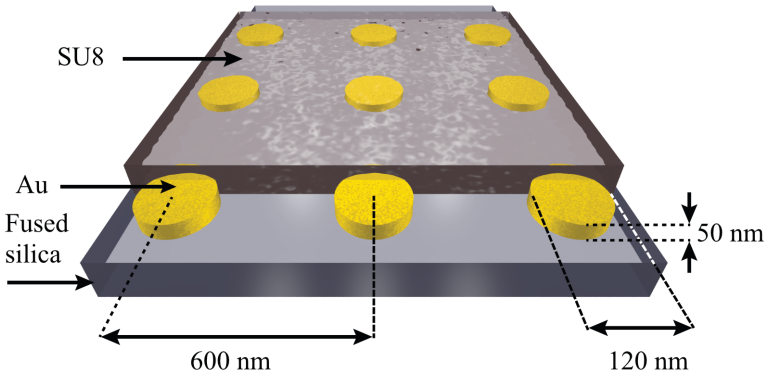

(a) Sample layout

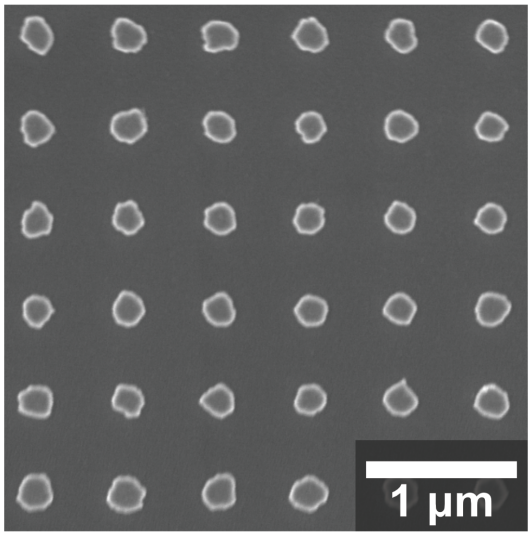

(b) Sample SEM

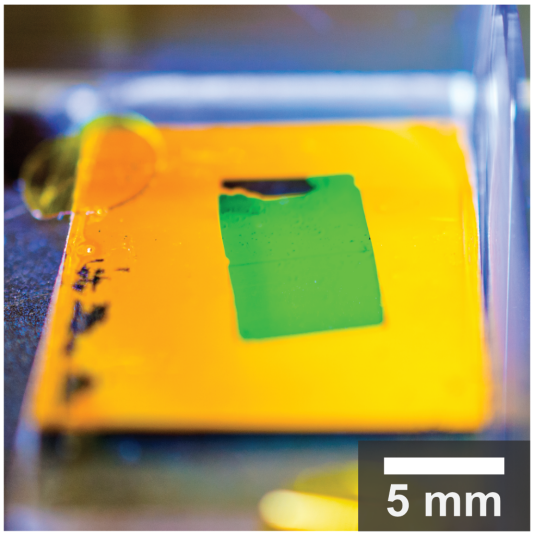

(c) Sample photo

Figure 6.3: Characterisation of the sample geometry. (a) Sample schematic and dimensions showing gold nanoparticles on a fused silica substrate and capped with photoresist (SU8). (b) Scanning electron micrograph of the fabricated nanoparticle array before capping with SU8. (c) Photograph of an investigated sample, the large-area nanostructured array appears green.

sample geometry is shown in Figure 6.3a. The nanoparticle arrays were fabricated using PEEL (a combination of photolithography, e-beam deposition, etching and lift-off). A scanning electron micrograph (SEM) of the 600 nm period array is shown in Figure 6.3b. An advantage of this fabrication technique is the ability to create large-area (cm^2) uniform arrays, as demonstrated in Figure 6.3c, where the nanoparticle array appears green due to its diffractive properties.

Measured transmission spectra of the arrays as a function of the angle of incidence are shown in Figure 6.4. The arrays were illuminated using a tungsten halogen lamp (Ocean Optics DH-2000-BAL), the intensity was attenuated using a reflective neutral density filter with an optical density of 1.0 (Thorlabs ND10A) so that the reference spectrum did not saturate the spectrometer. A calcite polariser (Thorlabs GL10) was used to select vertically polarised light. The beam was then focused onto the sample using an anti-reflection coated achromatic doublet lens with a focal length of 40 mm (Thorlabs AC254-040-A-ML). The sample was mounted on a rotation stage (Thorlabs NR360S/M NanoRotator stage) to control the angle of incidence. The sample was orientated with one of its lattice vectors parallel to the polarisation of the incident beam. Transmitted light was collected using a lens with a focal length of 35 mm (Thorlabs LA1027) and delivered by fibre to the spectrometer (Ocean Optics QE Pro). Spectra were acquired by taking the average of 10 spectra each with a 30 ms acquisition time. The measured spectra were normalised to a reference spectrum of the light source, acquired when the sample was removed from the set up, in order to obtain normalised transmission spectra.

It should be noted that some broadening of the Rayleigh anomalies should be expected in the spectra. This broadening arises because the white light source was focused onto the sample using a lens. Therefore, not all of the light will be normally incident because the numerical aperture results in a range of incident angles. The lens used in these linear characterisations had a focal length of 40 mm, a diameter of 25.4 mm, and a clear aperture of 90%, which can be used to calculate a maximum angle of incidence of 16° and a numerical aperture of approximately $NA = 0.4$ assuming a refractive index of $n = 1.5$ for N-BK7 glass. However, the clear aperture of the lens was only partially illuminated so the maximal angle of incidence would have been much less than 16° in practice. We can

see from Figure 6.2 that a 16° angle on incidence would shift the Rayleigh anomaly by over 100 nm, yet we can still resolve the Rayleigh anomalies in Figure 6.4 which demonstrates that any broadening due to focusing is not detrimental.

From the measured transmission spectra we can see that the normal incidence SLR occurs at 840 nm for the 580 nm period arrays, see Figures 6.4a and 6.4c, and at 870 nm for the 600 nm period array, see Figures 6.4b and 6.4d. We can also note that the lowest transmission is obtained for the silver nanoparticle arrays in Figures 6.4c and 6.4d. The 600 nm period arrays also have lower transmission in comparison to the 580 nm period arrays. By illuminating with only vertically polarised light the $[0, 1]$ and $[0, -1]$ diffraction orders have been suppressed and therefore do not appear in the measured transmission spectra. Using these transmission spectra allows a range of incident angles to be selected in order to target specific fundamental wavelengths for SHG enhancement.

Figure 6.5a shows a numerically calculated transmission spectrum of the 600 nm period gold nanoparticle array at normal incidence, performed using the commerically available finite difference time domain solver Lumerical.[178] The dip in transmission at 675 nm is attributable to the localised surface plasmon resonance. The Rayleigh anomaly is at 870 nm and the SLR is at 872 nm. The measured transmission for the 600 nm period gold at normal incidence is shown in Figure 6.5b. We can see that the simulated transmission reproduces the SLR well in terms of wavelength position. The width of the SLR is wider in the measured transmission likely due to broadening caused by the experiment and because the simulation deals with an ideal case. The simulated transmission however, does not reproduce well the feature at 700 nm seen in the measured transmission.

To illustrate the specific electromagnetic behaviour of the SLR, numerical simulations at two different wavelengths were performed – at the SLR and away from it. Specifically, these are electric field simulations, at the surface of a single nanoparticle, with periodic boundary conditions. In Figure 6.5c, at 780 nm, i.e. away from the SLR, the electric field is concentrated around the nanoparticle. By contrast, in Figure 6.5d, at 872 nm, i.e. at the wavelength of the SLR, the electric field radiated by the nanoparticle dipole extends to neighboring nanoparticles. This is evidenced by the dipole radiation reaching beyond a single unit cell. The enhancement of the electric near-field at the SLR leads to

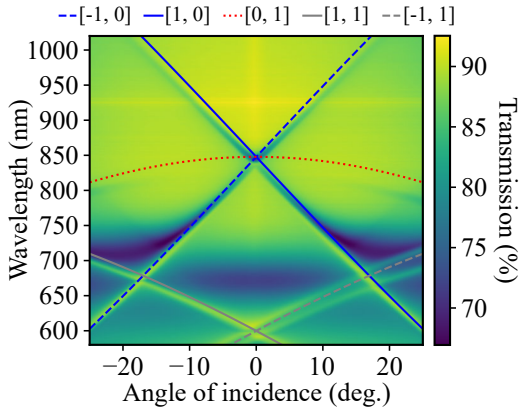

(a) Au nanoparticles with 580 nm periodicity

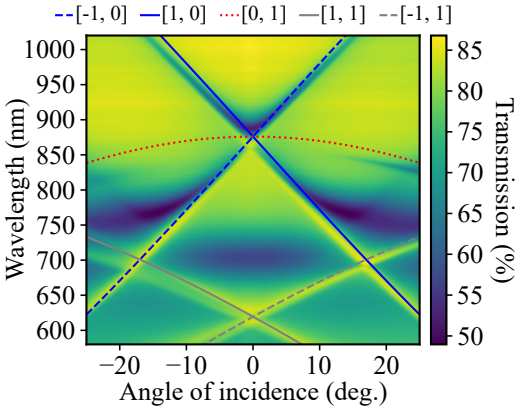

(b) Au nanoparticles with 600 nm periodicity

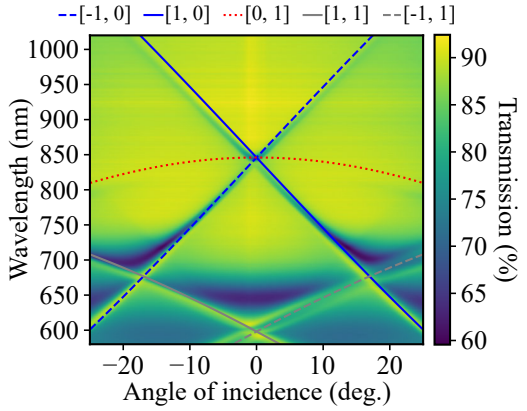

(c) Ag nanoparticles with 580 nm periodicity

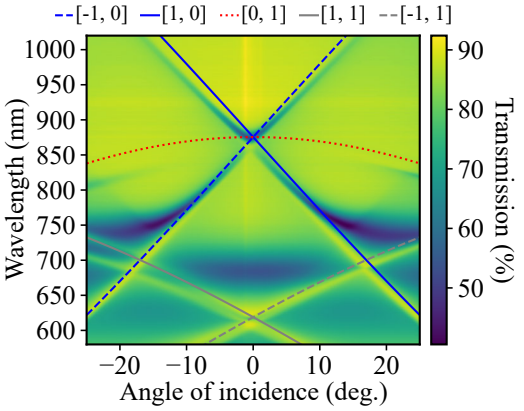

(d) Ag nanoparticles with 600 nm periodicity

Figure 6.4: Measured Rayleigh anomaly dispersion. Au and Ag nanoparticle arrays (a,b) and (c,d) with periodicities of 580 nm and 600 nm (a,c) and (b,d), respectively. The solid and dashed lines indicate the calculated Rayleigh anomaly dispersion, where the top legends show the diffraction orders [x,y].

an increased SHG signal.

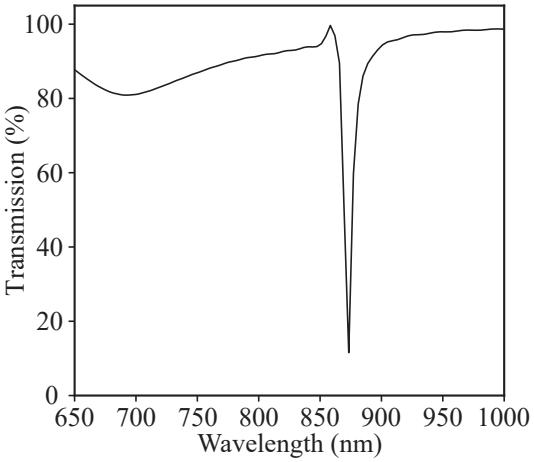

(a) Calculated transmission

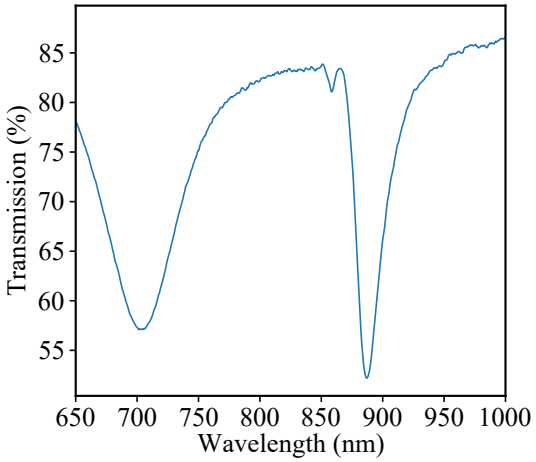

(b) Measured transmision

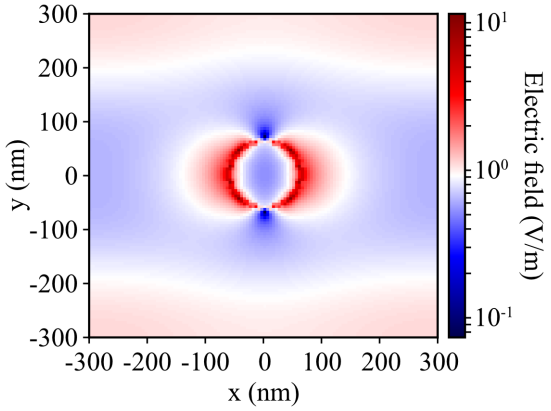

(c) $\lambda = 780$ nm

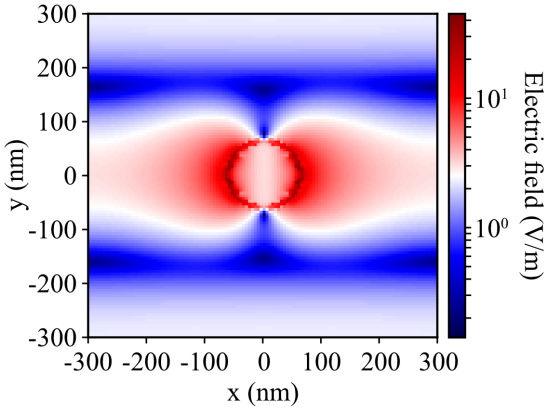

(d) $\lambda = 872$ nm

Figure 6.5: Numerical simulations illustrating the surface lattice resonance (SLR) enhancement of electric near-fields. (a) Calculated transmission for the 600 nm period gold array at normal incidence displays an SLR at 872 nm. (b) Measured transmission of the 600 nm period gold array at normal incidence. (c) The electric near-field at the surface of a gold nanoparticle in the 600 nm period array, away from resonance at $\lambda = 780$ nm. (d) The electric near-field at the surface of a gold nanoparticle in the 600 nm period array, at $\lambda = 872$ nm, the wavelength of the SLR. A distinctive radiative dipole can be seen, illustrating the nature of the SLR.

6.4.2 SHG tensor analysis for square arrays

As discussed in Chapter 2, SHG is caused by a part of the material polarisation that occurs and radiates at 2ω, i.e. twice the fundamental driving frequency ω. The second

order nonlinear polarisation given in Equation 2.30 can be rewritten as,

$$\mathbf{P}(2\omega) = \mathbf{P}^{\mathrm{D}}(2\omega) + \mathbf{P}^{\mathrm{Q}}(2\omega), \tag{6.4}$$

where $\mathbf{P}^{\mathrm{D}}(2\omega)$ is the dipole contribution to the second harmonic polarisation as in Equation 2.30, and $\mathbf{P}^{\mathrm{Q}}(2\omega)$ represents a quadrupolar contribution. These two terms can then be written in full as,[179]

$$P_{\mathrm{i}}^{\mathrm{D}}(2\omega) = \chi_{\mathrm{ijk}}^{(2,\mathrm{D})} E_{\mathrm{j}}(\omega) E_{\mathrm{k}}(\omega) \tag{6.5}$$

$$P_{\mathrm{i}}^{\mathrm{Q}}(2\omega) = \chi_{\mathrm{ijkl}}^{(2,\mathrm{Q})} E_{\mathrm{j}}(\omega) \nabla_{\mathrm{k}} E_{\mathrm{l}}(\omega), \tag{6.6}$$

where summation over repeated indices is implied. The indices i, j, and k, take the Cartesian directions and $E(\omega)$ is the electric field of the incident light. Here, $\chi_{\mathrm{ijk}}^{(2,\mathrm{D})}$ is the rank three tensor denoting the electric dipole susceptibility at the second harmonic, the first index designates the direction of the polarisation and the final two indices are the polarisation directions of the input fields. The quadrupolar contribution is represented by the rank four tensor $\chi_{\mathrm{ijkl}}^{(2,\mathrm{Q})}$. The expression for $P_{\mathrm{i}}^{\mathrm{Q}}(2\omega)$ in Equation 6.6 is obtained by a Taylor expansion and represents the quadrupolar contribution to the second order polarisation. Electric dipole contributions to SHG are forbidden in systems with inversion symmetry. The nanoparticle arrays are arranged in two-dimensional lattices that possess C_{4v} symmetry, for which the corresponding tensor is,[21]

$$\chi_{ijk}^{(2,\mathrm{D})} = \begin{bmatrix} 0 & 0 & 0 & 0 & \chi_{xxz} & 0 \\ 0 & 0 & 0 & \chi_{xxz} & 0 & 0 \\ \chi_{zxx} & \chi_{zxx} & \chi_{zzz} & 0 & 0 & 0 \end{bmatrix}. \tag{6.7}$$

The tensor in Equation 6.7 is mathematically identical to the rotationally isotropic surface tensor, $C_{\infty v}$. Equation 6.6 shows that the dipolar contribution to SHG scales as a power law of the electric field of incident light and that the quadrupolar contribution is proportional to the gradients of the local electric field. On the one hand, SLRs are surface-sensitive: a spectral shift is induced in response to the refractive index change in the local environment. On the other hand, they are bulk-sensitive: the electromagnetic field of the

SLR is not confined to the plane of the array, it extends over a volume, tens of hundreds of nm across.[180, 181] Consequently, combining SLRs and SHG presents obvious advantages and SHG spectroscopy of SLRs is currently of increasing interest.[154, 155, 182]

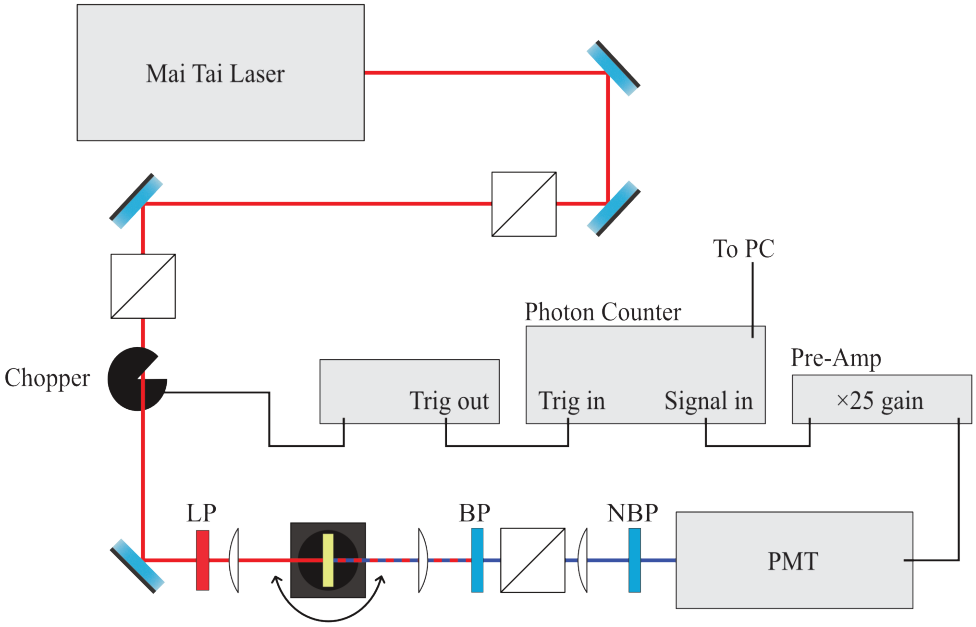

Figure 6.6: Schematic of the optics bench layout used to measure SHG from nanoparticle arrays. LP = long pass filter, BP = bandpass filter, NBP = narrow bandpass filter.

6.4.3 Nonlinear characterisation

These experiments demonstrate two types of SHG enhancement mechanism: one dominated by dipolar contribution (sensitive to the amplitude of SLR enhanced near-fields) and one dominated by higher-order contributions (additionally sensitive to the gradients of SLR enhanced near-fields). The layout of the optical bench for the SHG experiments is shown in Figure 6.6 while a more detailed schematic of the SHG experimental geometry is shown in Figure 6.7a. Experiments were performed using the tunable femtosecond pulsed laser and gated photon counting procedure outlined in Chapter 4. The average laser power was 0.5 mW across all experiments. The pulse fluence at this power is approximately 18.5 μJcm^{-2} considering the 80 MHz repetition of the laser. the 1.7% duty cycle of the chopper and approximate laser spot size of 50 µm. The laser was focused onto the samples using an anti-reflection coated achromatic doublet lens with a focal length of 100 mm (Thorlabs

AC254-100-B-ML). The samples were mounted on an automated rotation stage to change the angle of optical incidence, and an analysing polariser was used to decompose the SHG signal into its vertically (S) and horizontally (P) polarised components.

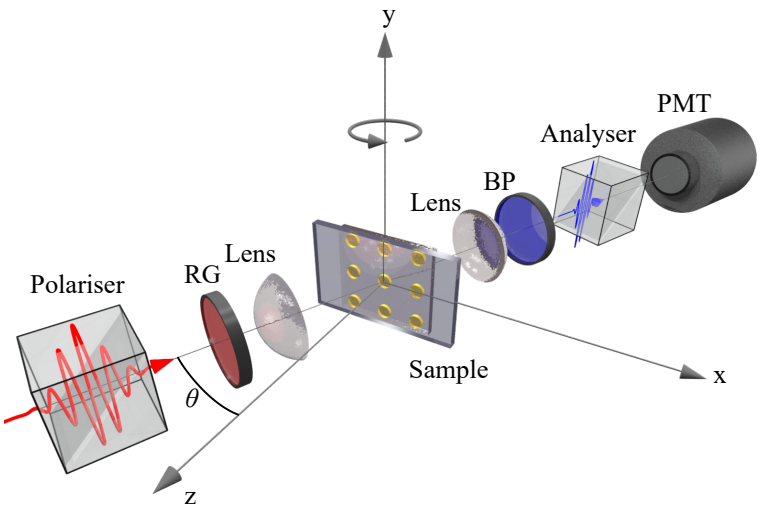

(a) Experimental geometry

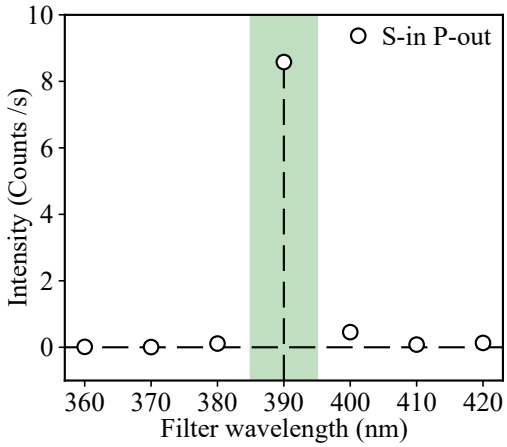

(b) Multiphoton background

Figure 6.7: The second harmonic generation (SHG) signal clearly stands out from the multiphoton background. (a) Experimental configuration for the SHG measurements, where θ is the angle of incidence. (b) For illumination with 780 nm fundamental light, the multiphoton emission is plotted versus wavelength. A 10 nm FWHM bandpass filter was used for each detection wavelength, the shaded region shows the FWHM of the filter. The dashed vertical line shows the SHG signal.

First, it is important to establish that the measurements correspond to SHG; for instance, three-photon luminescence could spectrally overlap with the detected SHG signal.

To characterise the respective contributions from multiphoton luminescence and SHG, a series of bandpass filters were used with their central wavelengths spaced in 10 nm intervals each with a 10 nm FWHM (Thorlabs FBxxx-10 where xxx is the central wavelength). In this experiment, the fundamental wavelength and the angle of incidence were kept constant at 780 nm and 9.2°, respectively. These values are close to an SLR in the 600 nm period samples. As Figure 6.7b illustrates, the strongest signal occurs at 390 nm, which is the SHG. For wavelengths 380 nm and below, as well as for wavelengths 400 nm and above, there is negligible signal, establishing that there is no contribution from multiphoton luminescence. The results unambiguously demonstrate that the signals measured in later experiments correspond to pure SHG.

In Figure 6.4 the measured Rayleigh anomaly dispersions are symmetric around normal incidence. This is further confirmed in Figure 6.8b, which shows the transmission of 800 nm light as a function of the angle of incidence. Therefore, if SHG is enhanced by an SLR the SHG signal will peak identically at positive and negative angles of incidence. To test for the symmetric enhancement of SHG the 600 nm period gold array was illuminated with 810 nm laser light. Then, the angle of incidence was scanned from positive to negative angles. In Figure 6.8a, the SHG intensity is plotted as a function of the angle of incidence, for the S-in P-out polariser-analyser configuration (i.e. vertical-in horizontal-out). Two strong SHG enhancements are observed at around ±6° angle of incidence. For angles of incidence between the peaks, there is no enhancement of SHG and the signal is below 0.2 counts per second. From these data, SHG at resonance is enhanced by over 150 times compared to off resonance, due to the strong electric near-fields around the nanoparticles provided by the SLR. Notably, this enhancement is already greater compared to the previous reports of 10 and 30 times.[154][155].

As mentioned previously, some broadening of the SLR peaks is to be expected because of the use of a focusing lens, which introduces a range of angles of incidence. For the lens used in these experiments the maximal angle of incidence is approximately 6.5°. However, the beam size incident on the lens is approximately 1.2 mm in diameter which should result in angles of incidence of less than 1°, which should not cause significant broadening of the SLR and hence the SHG peak. Another cause of broadening is Mai Tai laser, which

is the source of the fundamental. Because we are using a femto-second pulsed laser, each laser pulse has a bandwidth of approximately 10 nm in wavelength. Each wavelength component of the pulse will drive and SLR which could produce SHG. I speculate that it is the bandwidth of the laser pulses which contributes most to the broadening of the SHG peaks in Figure 6.8a and the data presented below.

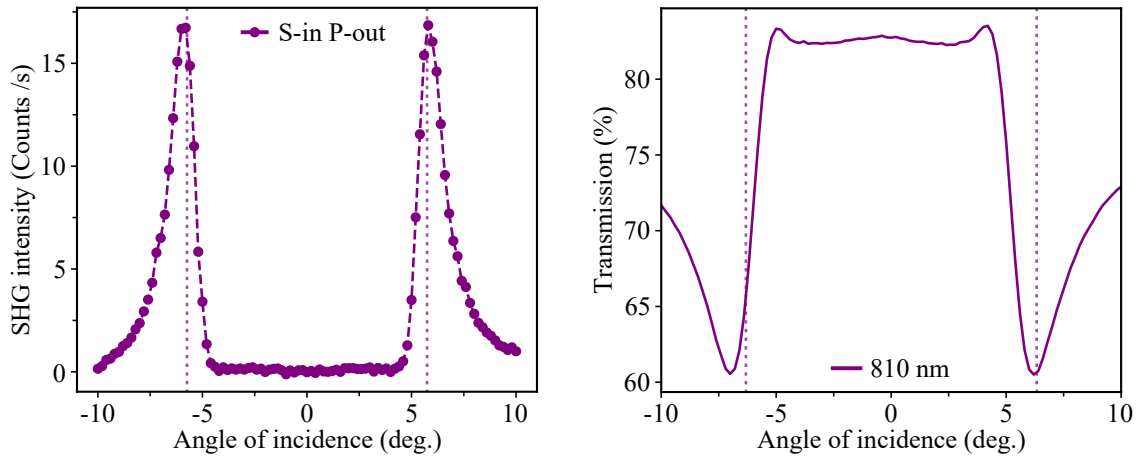

(a) Au nanoparticles with 600 nm periodicity, 810 nm fundamental

(b) Measured transmission of Au nanoparticles with 600 nm periodicity

Figure 6.8: (a) SHG enhancement from an SLR occurs near the Rayleigh anomaly corresponding to the fundamental wavelength of 810 nm for the 600 nm period gold array. Enhancement occurs symmetrically for positive and negative angles of incidence. (b) Measured transmission over the same angular range for the same wavelength used in (a). Vertical lines denote the calculated positions of the Rayleigh anomalies.

Now that it has been established that the measured signal is SHG it can be examined how the SLR enhancement of SHG is affected by parameters such as the fundamental wavelength, array periodicity and nanoparticle material. We begin with the gold nanoparticle arrays with periodicities of 580 nm and 600 nm. For the gold samples, the SHG was measured at four fundamental wavelengths: 800 nm, 790 nm, 780 nm and, 770 nm while varying the angle of incidence. The results are shown in Figures 6.9a and 6.9b for the 580 nm and 600 nm period arrays respectively. These figures show that, as the fundamental wavelength is decreased, the corresponding SHG enhancement shifts to greater angles of incidence. The SHG peaks track the angle of incidence at which a corresponding SLR occurs. Between Figures 6.9a and 6.9b the peaks are offset in angle of incidence. This offset is due to the change in array periodicity, which affects the position of the SLRs. It

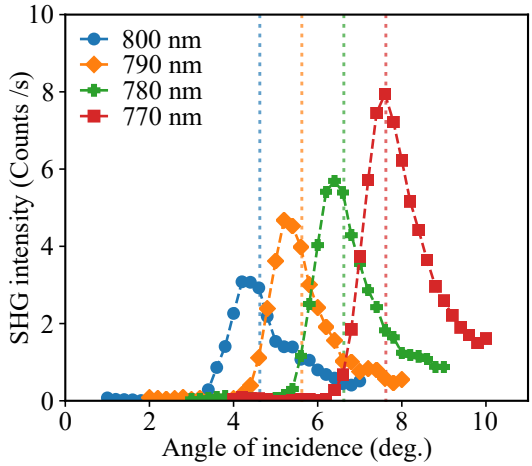

(a) Au nanoparticles with 580 nm periodicity

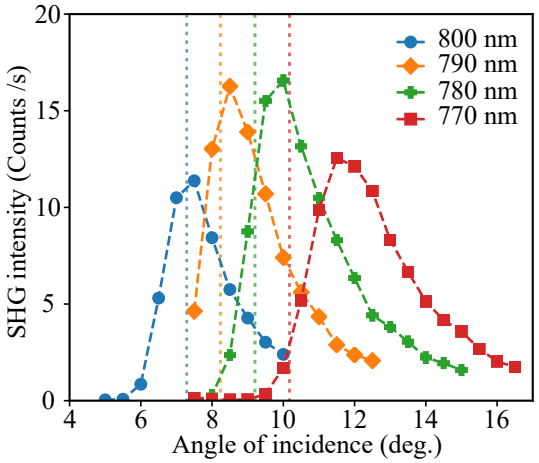

(b) Au nanoparticles with 600 nm periodicity

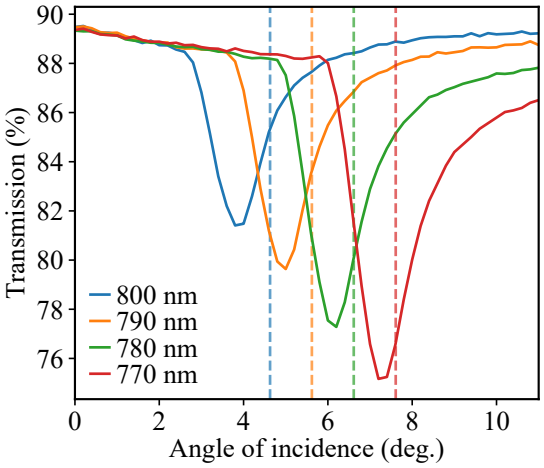

(c) Measured transmission of Au nanoparticles with 580 nm periodicity

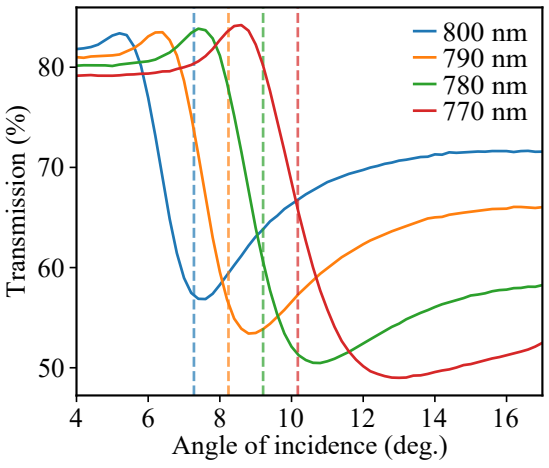

(d) Measured transmission of Au nanoparticles with 600 nm periodicity

Figure 6.9: Second harmonic generation (SHG) measured at different fundamental wavelengths with changing angle of incidence for the gold nanoparticle arrays. (a) 580 nm period array and (b) 600 nm period array. (c) and (d) Measured transmission over the same angular range and wavelengths as (a) and (b), respectively. The vertical dashed lines denote the calculated positions of the Rayleigh anomalies.

should be noted that all of the samples are covered with SU8, and that the difference in their behaviour is therefore not due to differences in their refractive index environment. In Figure 6.2 it was shown that the Rayleigh anomaly dispersion depends on the sample azimuthal angle. Therefore, all of the samples were orientated with one of their lattice vectors parallel to the polarisation of the incident fundamental beam.

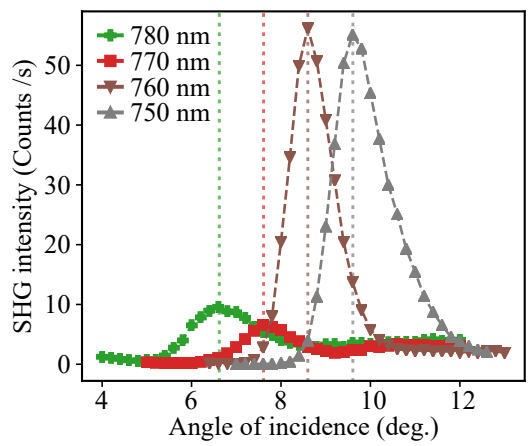

(a) Ag 580 nm

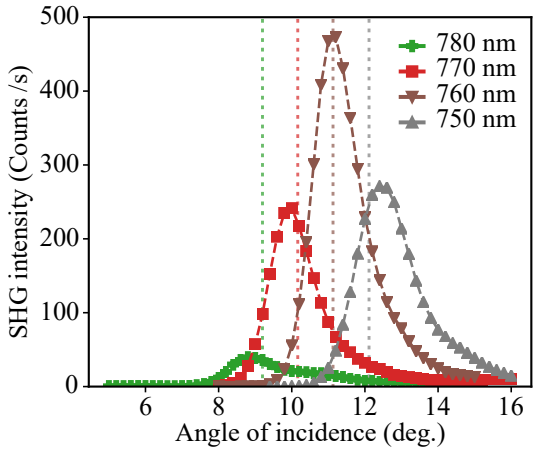

(b) Ag 600 nm

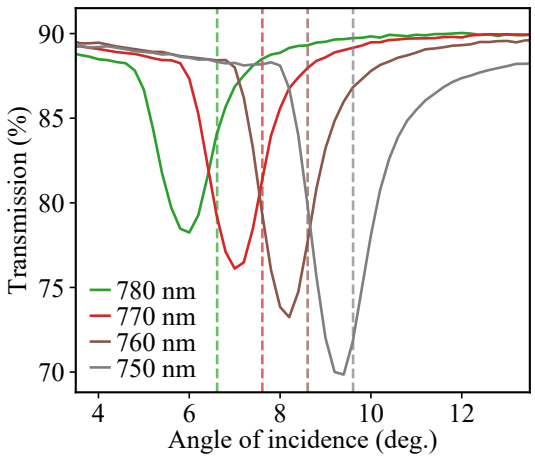

(c) Ag 580 nm measured transmission

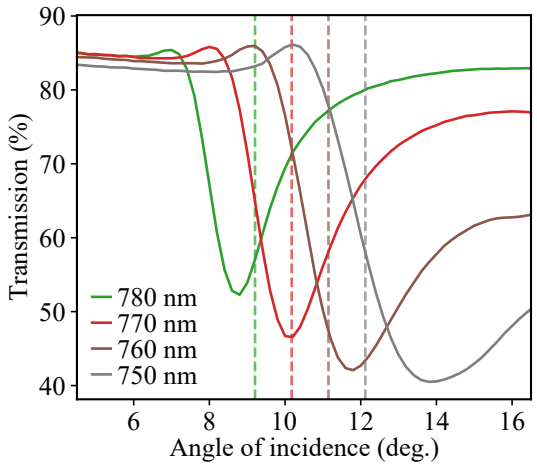

(d) Ag 600 nm measured transmission

Figure 6.10: Second harmonic generation measured at different fundamental wavelengths with changing angle of incidence for the silver nanoparticle arrays. (a) 580 nm period array and (b) 600 nm period array. Strong enhancements of the second harmonic generation follow the angles of incidence that correspond to a Rayleigh anomaly induced surface lattice resonance at the fundamental wavelength. All data acquired for the vertical-horizontal polariser-analyser configuration. (c) and (d) Measured transmission over the same angular range and wavelengths as (a) and (b), respectively. The vertical dashed lines denote the calculated positions of the Rayleigh anomalies.

To investigate the effect of nanoparticle material on the SHG enhancement arrays of silver nanoparticles were studied. The array periodicities were kept identical to the gold nanoarrays: 600 nm and 580 nm. For the silver samples, the SHG was measured at four fundamental wavelengths: 780 nm, 770 nm, 760 nm and, 750 nm while varying the angle of incidence. In the case of silver, an SHG enhancement of up to 450 times is observed for the 600 nm period array, as shown in Figure 6.10b. This enhancement occurs for a fundamental wavelength of 760 nm, at incident angle of 11.2°. The strength of this SHG enhancement can be attributed to a strong SLR. Indeed, the SHG scales as the 4^{th} power of the electric near-fields, which are enhanced at the SLR. In Figure 6.4d, the deep dark colour at the intersection of 760 nm and approximately 11° indicates very low transmission through the arrays, suggesting a strong SLR which results in the large enhancement of SHG.

At normal incidence the nanoparticle arrays are inversion symmetric and SHG is not expected in the dipole approximation. Increasing the angle of incidence breaks inversion symmetry and allows SHG. One might expect the SHG response to be stronger for SLRs at greater angles of incidence because increasing the angle of incidence further removes the array from its inversion symmetric state. However, we can see in Figures 6.9b and 6.10b that the SHG peaks for 770 and 750 nm fundamentals have lower amplitudes than the preceding SHG peaks at 780 and 760 nm. These diminished amplitudes occur despite that the SLRs for 770 and 750 nm SLRS appear at greater angles of incidence than the 780 and 760 nm SLRs. However, in Figures 6.9a and 6.10a the SHG response does increase for fundamental frequencies that produce SLRs at greater angles of incidence. Together, these data suggest that there is not a simple relationship between increasing angle of incidence and increasing SHG response because of further symmetry breaking.

It appears that other factors influence the strength of the SHG response. For example, the 600 nm period arrays yield more SHG compared to the 580 nm period arrays, suggesting that periodicity has a greater influence than angle of incidence. We can also see that the silver nanoparticles produce at least $\times 5$ more SHG than the gold nanoparticles, highlighting that the material of the nanoparticles has the greatest effect on the strength of the SHG response.

Furthermore, we can examine the transmission of each fundamental wavelength as a function of the angle of incidence. Figures 6.9c and 6.9d show the transmission spectra for the 580 and 600 nm period gold arrays, respectively. For the 580 nm period gold array the the SLRs appear to increase in strength as the fundamental wavelength is decreased. The SHG results reflect this behaviour as the SHG peaks increase in amplitude for shorter wavelength fundamentals. While the transmission spectra for the 600 nm period gold array again shows decreasing transmission for shorter wavelength fundamentals. However, the SHG peaks do not follow the behaviour of respective transmission lines in terms of amplitude, suggesting that the strength of the SLRs is not the only factor to determine the amplitude of the SHG peaks. On the other hand, the transmission for the 600 nm array is much lower than the 580 nm array, which works to confirm that SLR strength does play some role in determining the SHG peak amplitude. Additionally, the apparent width of the SLR peaks may determine the width of the SHG peaks, which would explain why the SHG peaks for the 600 nm gold array are much wider compared to the 580 nm array.

The transmission spectra for the 580 and 600 nm period silver arrays are shown in Figures 6.10c and 6.10d, respectively. The transmission spectra for the silver arrays show many of the same features as the transmission spectra for the gold arrays, albeit the SLRs and SHG peaks are shifted accordingly. One noticeable difference is that the minimums of transmission for the silver arrays are generally lower, indicating stronger SLRs. These stronger SLRs could be the reason why the SHG response of the silver arrays is much greater that the gold arrays.

In both Figure 6.9 and Figure 6.10, the SHG signal is electric dipole allowed. The experimental geometries (polariser-analyser combinations and angles of optical incidence) address the non-zero tensor elements in Equation 6.7. In order to evidence the higher-order contributions to SHG, an experimental geometry that is electric dipole forbidden must be selected, i.e. one which addresses a zero tensor component in Equation 6.7.

In Figure 6.11, the SLR enhancement of the higher-order contributions to SHG are demonstrated. Here, the experimental geometry of interest is the S-in S-out (vertical-vertical) polariser-analyser configuration, at normal incidence. Under these conditions,

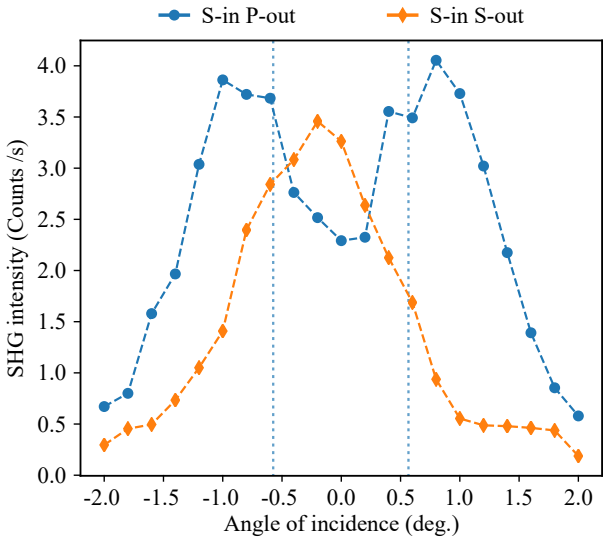

(a) $\lambda = 870$nm

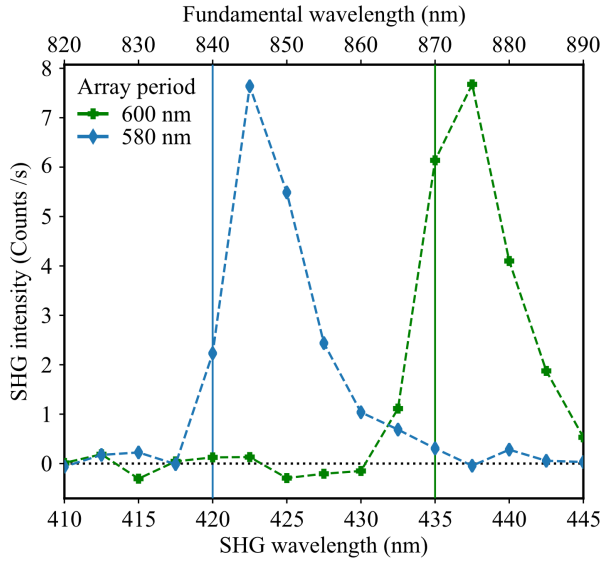

(b)

Figure 6.11: (a) S-in P-out (blue dots) SHG signal is attributable to electric dipolar contributions. The fundamental light is at 870 nm and the peaks correspond to the SLRs. For S-in S-out (orange diamonds), the signal peaks at normal incidence, where the higher-order contributions to SHG appear. The blue vertical dotted lines indicate the position of the Rayleigh anomaly for 870 nm light. (b) Measuring SHG spectra, for S-in S-out and at normal incidence, these higher-order contributions to SHG peak at the normal incidence SLR wavelength, for both the 600 nm and 580 nm period arrays. The blue and green solid lines indicate the Rayleigh anomalies for the 580 and 600 nm periodicities, respectively.

within the electric dipole tensor, only the tensor component yyy is addressed. As seen in Equation 6.7, this component is zero, for our samples, i.e. SHG is from electric dipoles is forbidden. Figure 6.11a shows the SHG signal versus the angle of incidence, for a fundamental wavelength of 870 nm incident on the 600 nm period gold nanoparticle array. For the S-in S-out (vertical-vertical) polariser-analyser configuration, a distinct SHG peak can be seen (orange diamonds), centred at normal incidence, i.e. precisely in the electric dipole forbidden configuration. This enhancement is attributable to the SLR near normal incidence. Indeed, 870 nm is very close to the normal incidence SLR, as demonstrated by both theory and experiment. The wavelength of the normal incident SLR was numerically calculated to be at 872 nm, see Figure 6.5a. Experimentally, in the S-in P-out (vertical-horizontal) polariser-analyser configuration, which is electric dipole allowed, we observe two peaks (blue dots) that are similar to the data in Figures 6.9 and 6.10 and are only 2° apart in angle of incidence.

Additionally, Figure 6.11b unambiguously demonstrates that the SHG enhancement in the electric dipole forbidden configuration is due to the normal incidence SLR. The data were recorded for both gold nanoparticle samples, in the S-in S-out (vertical-vertical) polariser-analyser configuration and at normal incidence. For each sample, the SHG spectra peak (10 nm FWHM) is at the wavelengths of the SLR, red-shifted with respect to the wavelength of Rayleigh anomaly. Physically, there is a direct link between SLRs and the higher-order contributions to SHG. First, it should be noted that we do not discuss plasmonic quadrupolar modes of the nanoparticles. Rather it can be seen from Equation 6.6, that the quadrupolar contribution to the second harmonic polarisation is proportional to gradients of the local electric field. At the SLR, such electric field gradients are quite pronounced, see Figure 6.5d. Quadrupolar SHG originating from the surface of nanoparticles has been demonstrated previosuly.[183]

The analysis of the SHG results presented in Figure 6.11 is based on the assumption that the zero tensor component in Equation 6.7 is addressed, which implies isotropic symmetry. However, small shape imperfections of the nanostructures can break the isotropy leading to the appearance of electric dipole allowed SHG at normal incidence.[184, 185] Moreover, lattice defects can also lead to electric dipole allowed SHG. These hypothetical

electric dipole contributions would usually be very small but, in these experiments, they could be enhanced by the SLRs and become measurable. However, as can be seen in Figure 6.11a, the SHG signal for S-in S-out peaks at normal incidence and not at the angles corresponding to the SRLs, where electric dipole SHG attributable to surface lattice resonantly-enhanced imperfections should have appeared ($\pm 1°$). Therefore, the S-in S-out signal cannot be attributed to an SLR enhanced electric dipolar contribution to SHG.

6.5 Hybrid quadrupole lattice mode

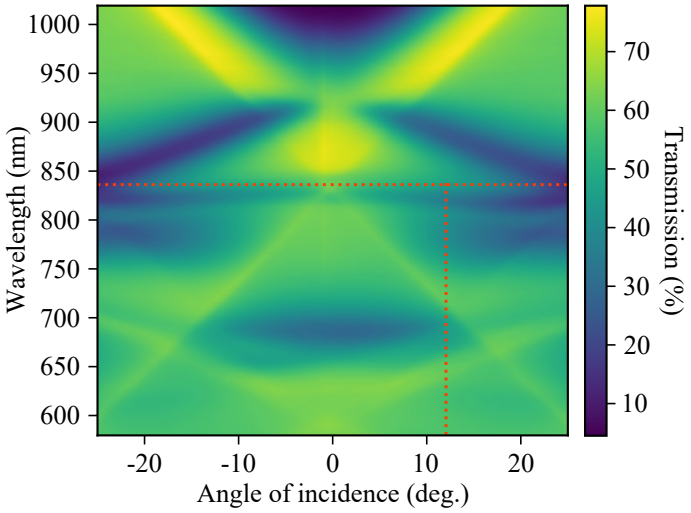

Figure 6.12: Measured Rayleigh anomaly dispersion for the array that supports a hybrid quadrupole lattice mode which occurs at a wavelength of approximately 836 nm, indicated by the red horizontal dashed line.

In the samples examined so far the surface lattice resonances have been mediated by radiative dipole coupling between the nanoparticles. The geometry of the individual nanoparticles is one determining factor as to which plasmonic modes the nanoparticles can support. For small nanoparticles (<50 nm) only the dipolar mode can be excited by light at optical frequencies.[186]. Altering the aspect ratio of the nanoparticles, for instance by increasing their height or by fabricating rods, means they are able to support a quadrupolar mode. Dipole-quadrupole coupling can occur while the dipole and quadrupole mode couple to the diffraction mode creating what is called a *hybrid quadrupole lattice mode* (HQL). The charge distribution in the nanoparticle at the HQL mode is a superposition of the dipole and quadrupole mode charge distributions. As a result of this superposition, an

asymmetry in the charge distribution in the nanoparticle occurs along the z direction (out of the array plane). This asymmetry leads to a net-dipole moment in the $x - y$ plane (plane of the array) which facilitates coupling to the far field.

The measured dispersion of an array that supports an HQL mode is shown in Figure 6.12, where the HQL mode occurs at a wavelength of 836 nm. The HQL mode presents as a flat band that intersects the normal incidence Rayleigh anomaly. Distinct regions of lower transmission also appear in the wavelength range of 840 - 920 nm which begin at a few degrees away from normal incidence and continues over the measurable range of angles of incidence. It is these new features in the HQL sample Rayleigh anomaly dispersion that present potentially novel mechanisms for enhancing SHG compared to the purely dipolar-mediated SLR.

To investigate how the HQL mode behaviour affects the SHG emission from the arrays we used the experimental geometry shown in Figure 6.7a. Fundamental wavelengths of 836 nm and 900 nm were chosen to probe the new features in the Rayleigh anomaly dispersion shown in Figure 6.12. The nanoparticles in the HQL sample have a diameter of 260 nm, a height of 120 nm and are capped with a 200 nm layer of SU8. Because the nanoparticles are arranged in a square lattice the samples were orientated with one of their lattice vectors parallel to the polarisation of the fundamental beam. SHG from the HQL mode at 836 nm as a function of angle of incidence is shown in Figure 6.13a. In contrast to the clear peaks of SHG enhancement seen in Figures 6.9 and 6.10, the SHG from the HQL sample shows no such peak. Instead, the SHG emission appears to continue increasing with increasing angle of incidence. However, two regimes of enhancement can be identified in Figure 6.13a, the first occurs for angles of incidence from 6° to 12°, where the gradient is steepest. The second regime occurs for angles of incidence from 12° to 20°, where the increase in SHG slows and the gradient is less steep. Careful inspection of Figure 6.12 reveals that the transmission begins to increase around 12° angle of incidence (marked by the red vertical dashed line) suggesting that the HQL mode at 836 nm is diminished, which explains the change in the gradient between the two regimes. However, if we examine Figure 6.13c, which shows the transmission of the HQL sample at 836 nm as a function of angle of incidence, we find that there is not a sharp transition of the in the

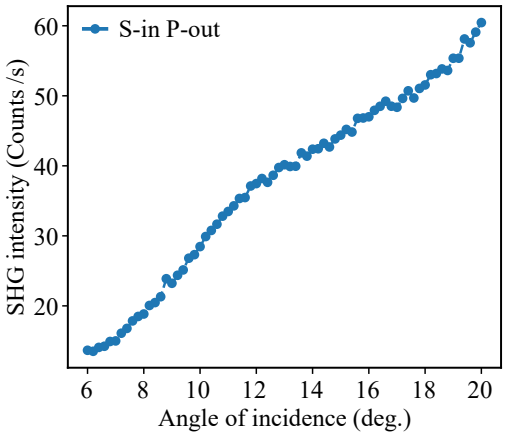

(a) $\lambda = 836$ nm

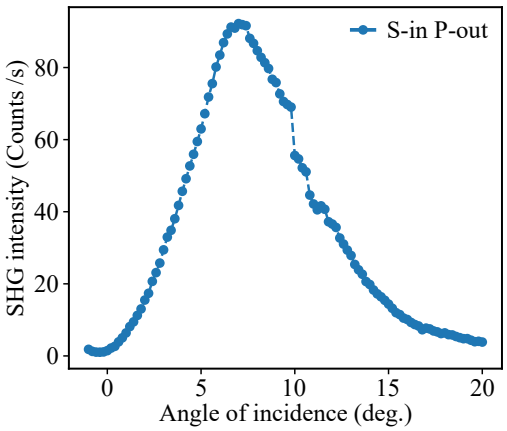

(b) $\lambda = 900$ nm

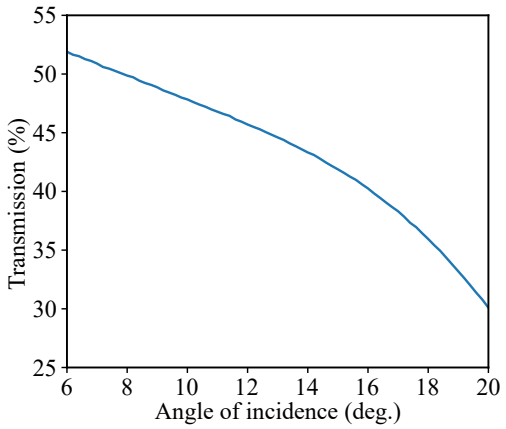

(c) Transmission at $\lambda = 836$ nm

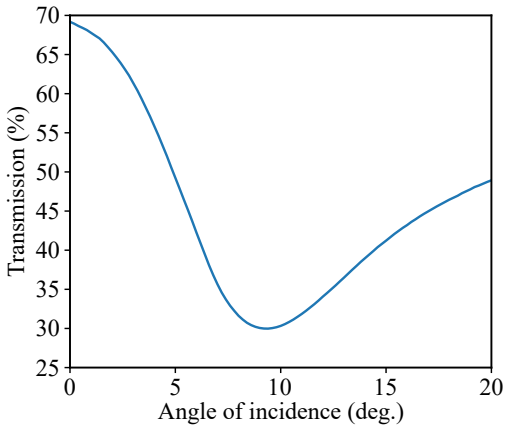

(d) Transmission at $\lambda = 900$ nm

Figure 6.13: Second harmonic generation measurements of the array that supports a hybrid quadrupole lattice (HQL) mode. (a) At the wavelength of the HQL mode. (b) A wavelength away from the HQL mode. (c) and (d) show the measured transmission at wavelengths of 836 and 900 nm respectively.

transmission. Rather, the transmission slowly decreases in comparison to the relatively sharp change in gradient seen in the SHG data.

Next, a fundamental wavelength of 900 nm is chosen to examine the SHG response of the other unique feature in the Rayleigh anomaly dispersion of the HQL sample. A peak in the SHG enhancement from the HQL sample can clearly be seen in Figure 6.13b. This peak is similar to the responses seen in Figures 6.9 and 6.10 albeit, the FWHM of the peak in Figure 6.13b is approximately doubled. Again, close examination of Figure 6.12 provides an explanation to the observed behaviour. Light with a wavelength of 900 nm experiences strong absorption and scattering between 4° and 12° angle of incidence. For incident angles greater than approximately 12° the transmission of the array begins to increase. This trend in transmission can be seen in Figure 6.13d, where the transmission falls from a maximum of approximately 70% down to a minimum of about 30% at a turning point at a 9° angle of incidence. However, the transmission spectra fails to reproduce the feature on the right shoulder of the SHG data. It is difficult to speculate as to what causes the behaviours for 900 nm because they are not part of the hybrid-quadrupole lattice mode and conventional SLRs are not expected in this parameter space.

6.6 Nickel nanoparticle arrays

The noble metals gold and silver are favoured for plasmonic applications. However, other metals can be utilised, especially if they possess properties not displayed by gold and silver, such as magnetism. Nickel is ferromagnetic and has been used in nanoparticle arrays previously.[187] An applied magnetic field can act as another tuning parameter in magnetic systems. In SHG this occurs through magnetisation-induced SHG. The work presented here was performed at zero-field but serves as a proof of principle that nickel nanoparticle arrays can produce SHG. In order to obtain a surface lattice resonance the nanoparticles were fabricated with a diameter of 130 nm, a height of 50 nm with a 200 nm capping layer of SU8. The period of the lattice was kept to 600 nm. Firstly, the Rayleigh anomaly dispersion of the nickel nanoparticle array was measured and is presented in Figure 6.14. Noticeably the overall transmission away from the Rayleigh anomalies is significantly lower compared to Figure 6.4 which is due to the higher absorption of nickel

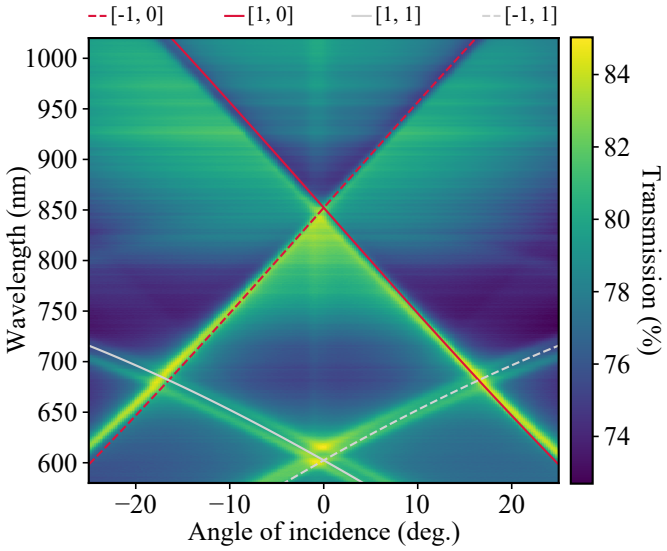

Figure 6.14: Measured Rayleigh anomaly dispersion for the nickel nanoparticle array. The absorption is much greater compared to the gold and silver nanoparticle arrays. The solid and dashed lines show the calculated positions of the Rayleigh anomalies.

metal compared to gold and silver.

As with Figure 6.8a surface lattice enhanced SHG can be tested for by scanning positive and negative angles of incidence at a single wavelength. Peaks symmetric around normal incidence will occur if the SHG is being enhanced by SLRs. A wavelength of 800 nm was chosen as the equipment has optimal detection efficiency at 400 nm, the second harmonic. Results of the symmetric angle of incidence scan are shown in Figure 6.15a which shows SHG peaks at $\pm 5°$, confirming that the SHG is being enhanced by SLRs. The position of the peaks correspond well to the position of the SLRs shown in the transmission measurement in Figure 6.15c. Figure 6.15b shows an extended range of positive angles of incidence, again at a wavelength of 800 nm. However, the overall SHG intensity is lower, which could suggest that the array is being damaged. Also, the SHG does not decrease to its initial level after the first peak, instead there is a second peak at 8° angle of incidence. This second peak could be as a result of damage as the dispersion diagram in Figure 6.14 does not indicate any reason for a secondary peak. Nonetheless, the data in 6.15a clearly demonstrates SHG enhanced by SLRs. Additionally, we can see in Figure 6.15d that there is no secondary peak in the transmission in the measured range of angles of incidence, further suggesting that the secondary SHG peak is not caused by a SLR.

Future work should focus on mitigating damage to the array, for example by using a lens with a longer focal length in order to decrease the power density of the incident beam.

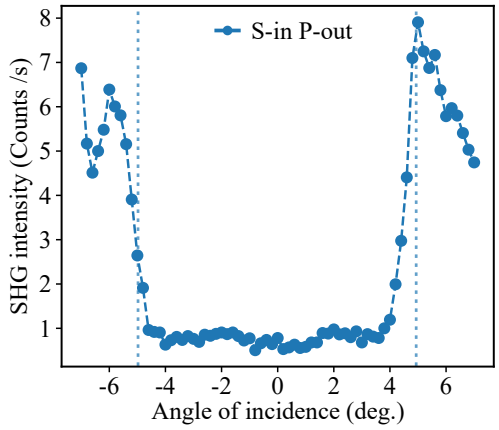

(a) $\lambda = 800$ nm

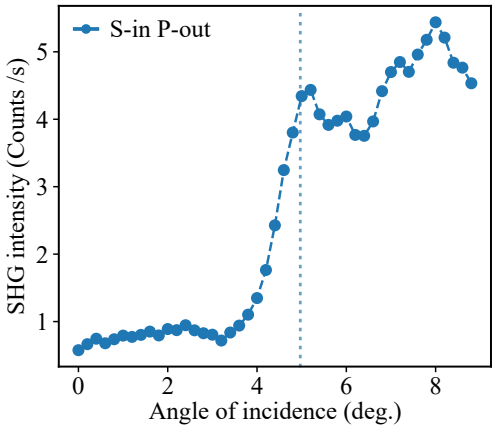

(b) $\lambda = 800$ nm

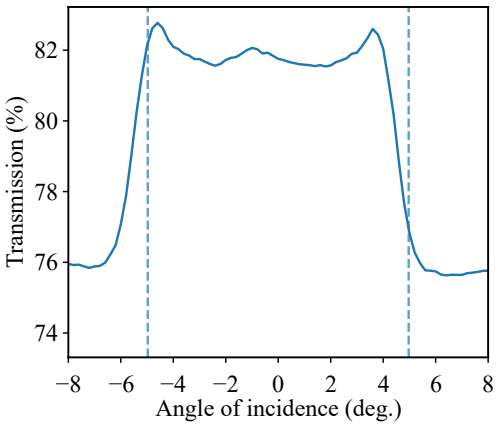

(c) Transmission at $\lambda = 800$ nm

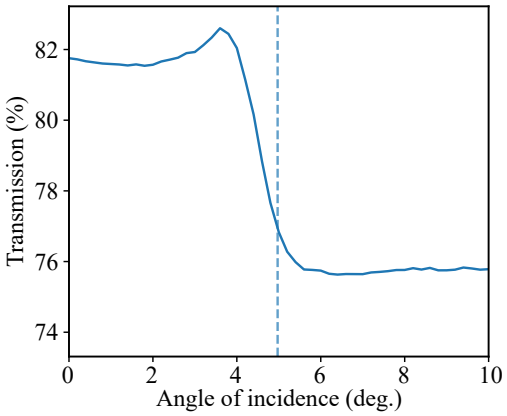

(d) Transmission at $\lambda = 800$ nm

Figure 6.15: Second harmonic generation measurements of the nickel nanoparticle array. (a) Measurement symmetric around normal incidence. (b) Measurement with extended range of positive angles of incidence. (c) and (d) show the measured transmission over the same angular ranges of (a) and (b) respectively. The blue vertical dotted lines show the calcualted position of the Rayleigh anomaly.

6.7 Conclusions

In conclusion, spectroscopy of SHG enhanced by SLRs was demonstrated, where the signal can be enhanced up to 450 times. Both electric-dipole allowed (in Figures 6.9 and 6.10) and electric-dipole forbidden (in Figure 6.11) SHG resonances are presented. The observed

SHG resonances are as narrow as 5 nm FWHM, which indicates that a high FoM can be achieved, opening new avenues for chemical and biosensing applications. Moreover, the SHG technique is intrinsically surface-sensitive, which can lead to improved near-field surface sensing, especially using higher-order resonances that originate from gradients in plasmonic near-fields, see Equation 6.6. Equation 6.6 also demonstrates how SHG can improve upon the bulk sensitivity of SLRs. This bulk sensitivity originates from far-field coupling between nanoparticles and, for electric dipole allowed SHG resonances, the sensitivity would additionally benefit from a power law dependence on the far-fields. It should also be pointed out that the SHG process occurs via virtual energy levels at ultrafast timescales.[21] This process could therefore enable ultrafast probes of the refractive index and could be useful for monitoring chemical reactions, e.g. catalysis by the nanoparticles. To explore the limits of these applications, future work should focus on the importance of the environment surrounding the nanoparticle arrays.[188, 189]

The position of the SHG peaks were compared to their respective linear transmission measurements. A good agreement was found between the position of the SLRs located in transmission measurements and the SHG peaks. On the other hand, the calculated position of the predicted SLR did not always match with the experimental data. This mismatch is due to how sensitive the Rayliegh anomaly calculation is to the refractive index, even changes as small as 0.01 can cause the Rayleigh anomalies to shift dramatically. While the position of the SLRs corresponds well to the SHG peaks, indicating that SLRs enhance SHG, the magnitude of the transmission does not predict the amplitude of the SHG peaks. This fact is most evident for the 600 nm period arrays, suggesting perhaps that the array periodicity has an effect beyond simply determining the Rayleigh anomalies.

It is also evident that the choice of nanoparticle material determines the nonlinear response. The silver nanoparticle arrays produced more SHG compared to the gold nanoparticle arrays, which may in part be because of their stronger SLRs as indicated by the lower transmission at the Rayleigh anomalies. However, the fundamental wavelengths used to investigate the silver arrays were shorter compared to the gold arrays. Even though the Rayleigh anomalies occur at the same wavelength for both silver and gold arrays, the silver arrays required shorter fundamental wavelengths to generate SHG. This need for

shorter fundamental wavelengths suggests that the plasmonic properties of the individual nanoparticles plays a significant role in the magnitude the arrays' SHG response.

The gold and silver nanoparticle arrays investigated in this work were able to enhance SHG considerably more that previous works. This improved enhancement likely originates from the choice of nanoparticle shape. In this work the nanoparticles were disc shaped and easily supported electric dipoles. However, in previous works the nanoparticles were shaped as L's and as split ring resonators and while both geometries support electric dipoles it is also easier to excite other modes, especially in the case of split ring resonators. Meanwhile, the nanoparticles in the arrays of this work were optimised to produce strong SLRs, hence why the enhancement to SHG is much greater.

Second harmonic generation was also enhanced by a hybrid quadrupole lattice mode. The HQL enhancement of the SHG does not present a clear peak like the dipole dominated SLRs, indicating a different behaviour compared to the dipole SLRs. However, an SHG peak is observed away from the HQL mode using a fundamental wavelength of 900 nm. The HQL mode is obtained by increasing the height the nanoparticles in order to allow for a quadrupole. In turn, the emission profile of the nanoparticle is changed. It can be envisioned that the nanoparticle geometry can be optimised for coupling the SHG into the far field at a specific angle.

Furthermore, nickel nanoparticle arrays were also studied and an SLR enhancement of SHG was observed. While the ferromagnetic elements suffer from oxidation, generally possess high absorption and make poor plasmonic nanoparticles, the ability to alter the SHG via an applied magnetic field is quite appealing. In addition to applying an external field, the geometry of a magnetic nanoparticle contributes to shape anisotropy. The effect of the interplay between lattice resonances and the nanoparticle shape anisotropy makes for an exciting platform to study magnetisation induced SHG.

Overall, nanoparticle arrays and their associated lattice resonances provide a veritable cornucopia of systems with which to control nonlinear optical processes. Applications based on the linear optical properties of SLRs are relatively well developed and are still being explored.[153] However, many parameters have yet to be investigated in regards to their affect on the nonlinear response of nanoparticle arrays. Such parameters include,

dynamic lattice spacing via stretchable substrates,[168] different lattice types,[190] complex unit cells with multiple nanoparticles[191] or arrays with more than one type of nanoparticle material.[192] All of these make for exciting avenues of research in nonlinear nanophotonics.[182]

Chapter 7

Conclusion and outlook

7.1 Conclusions

Nanophotonics and metamaterials aim to control light at subwavelength scales by using arrays of specially designed nanostructures. Developments in nanofabrication techniques have allowed such nanostructures to be realised. These developments along with the excitement surrounding negative refractive index materials and using plasmonics to route light resulted in a growing surge of work on creating nanomaterials with tailored optical properties. The development of nanomaterials that control the linear optical properties of light has made good headway. On the other hand, the development of nonlinear optical nanomaterials is less mature and is in part hampered by the lack of design rules for such materials as well as the complexity of nonlinear processes.

In this thesis, the nonlinear optical characterisations of two types of nanostructured arrays were presented. The aim of these characterisations was to deduce the physical mechanisms that determine the systems nonlinear optical response. This work contributes to the body of knowledge on how to characterise the second harmonic generation of nanomaterials so that in the future robust design rules can be formulated for engineering nanomaterials with bespoke nonlinear optical behaviours.

The rotational anisotropy was shown to have a strong effect on the nonlinear chiroptical response of nanohelix arrays. This result highlights that when quantifying the nonlinear chirality of a nanomaterial, anisotropy needs to be taken into account. If the anisotropy of

a material is not considered in its nonlinear characterisation then it is difficult to deduce meaningful design principles that can be applied in the future.

Enhanced SHG from nanoparticle arrays that support surface lattice resonances was also observed. The narrow FWHM of the resonantly enhanced SHG makes nanoparticle arrays promising platforms for nonlinear sensing applications. Dipole forbidden SHG was also observed, which is attributed to electric field gradients in the individual nanoparticles caused by the strong normal incidence SLR. Potential applications based on the linear optical properties of such nanoparticle arrays are already well developed. The strong enhancement of SHG could further expand the applications of these systems, especially considering the number of degrees of freedom that can be tuned to produce unique behaviours.

The field of nanophotonics currently benefits from sophisticated fabrication techniques and increasingly refined numerical simulations in the drive towards controlling light at the nanoscale. Nanostructures that act as conventional optics, such as lenses, have already been achieved. With these achievements, it appears that using metamaterials for ultra-thin planar optics is within grasp. These ultra-thin optics would replace conventional optical elements have been used for centuries. Then considering that the field of nonlinear optics has only existed for a few decades, since the invention of the laser, then controlling the wavelength of light on the nanoscale seems truly ambitious. However, this goal is attainable with the help of thorough nonlinear characterisations, as presented here, which can be used to build a knowledge base of design rules to create nanomaterials with tailored nonlinear behaviours, further extending our mastery of light.

7.2 Outlook

The nanohelices discussed in Chapter 5 exhibit complicated behaviours that are a convolution of their own intrinsic chirality, their own anisotropy, and extrinsic chirality. There has been interest in studying these factors separately. Hopefully, this work will prompt further investigation into how all these factors can work together as anisotropy could be used to switch or change the response of a material, rather than having to create reconfigurable nanomaterials. Previous works largely focused on planar chiral materials which rely on

the interface to fully break inversion symmetry. The presented work further confirms that SHG is a good probe of symmetry, even for three-dimensional structures. SHG has also been used to study the superchiral fields of chiral nanostructures. With the effectiveness of SHG for investigating three-dimensional structures shown in this work, SHG could experimentally elucidate the nature of superchiral fields predicted to occur in the centre of nanohelices. There is great interest in using chiral materials for chemical sensing, previous works have focused on planar structures in the linear optical regime. Second-order chiroptical effects are more sensitive to chirality and the demonstrated high SHG-CD of the investigated helices show that they are good candidates for chemical sensing especially as they can be fabricated over whole wafers.

Nanoparticle arrays that support surface lattice resonances are currently drawing attention for sensing, lighting, and lasing with an increasing interest for applications in nonlinear optics. The work discussed in Chapter 6 of this thesis demonstrates that nanoparticle arrays can achieve relatively high nonlinear conversion rates, especially when the nanoscale propagation length is considered. While it is unlikely that SHG from SLRs will replace traditional nonlinear crystals in the near future, other applications can be further developed. For instance, refractive index sensing using SLRs has already been established, it can then be envisioned that SHG measurements would add to the versatility of such methods. With the demonstration of SHG from quadrupoles in this work further sensing functions can be anticipated. For example, an analyte that coats the nanoparticle array would experience enhanced electric near fields between the nanoparticles, while the target molecules situated on top of the nanoparticles would experience the surface quadrupoles. Differences between the interaction of the analyte with the dipolar and quadrupolar enhancements could make for interesting sensing platform.

Furthermore, the additional work on SHG from HQL modes and nickel nanoparticle arrays demonstrates the flexibility of collective resonances for enhancing nonlinear optical processes. Results for the HQL modes show that SHG can be enhanced by collective resonances that are not just dipolar in nature, which expands the opportunities for designing nanoparticle arrays with more exotic properties. The nickel nanoparticle arrays show that SHG can enhanced by SLRs even when the nanoparticles are not fabricated from

a traditionally good plasmonic material. By demonstrating that the nanoparticles in an array do not need to possess good plasmonic properties, we have opened the door to integrating more materials into nanoparticle array designs. With more materials from which to choose, nanoparticle arrays can be further engineered to meet bespoke applications in nonlinear nanophotonics.

References

[1]T. H. Maiman, "Stimulated optical radiation in Ruby", Nature **187**, 493–494 (1960).

[2]P. A. Franken, A. E. Hill, C. W. Peters, and G. Weinreich, "Generation of Optical Harmonics", Physical Review Letters **7**, 118–119 (1961).

[3]R. W. Wood, "On a remarkable case of uneven distribution of light in a diffraction grating spectrum", Proceedings of the Physical Society of London **18**, 269–275 (1902).

[4]L. Rayleigh, "III. Note on the remarkable case of diffraction spectra described by Prof. Wood", Philosophical Magazine Series 6 **14**, 60–65 (1907).

[5]L. Rayleigh, "On the Dynamical Theory of Gratings", Proceedings of the Royal Society A: Mathematical, Physical and Engineering Sciences **79**, 399–416 (1907).

[6]U. Fano, "The Theory of Anomalous Diffraction Gratings and of Quasi-Stationary Waves on Metallic Surfaces (Sommerfeld's Waves)", Journal of the Optical Society of America **31**, 213 (1941).

[7]T. W. Ebbesen, H. J. Lezec, H. F. Ghaemi, T. Thio, and P. A. Wolff, "Extraordinary optical transmission through sub-wavelength hole arrays", Nature **391**, 667–669 (1998).

[8]H. A. Bethe, "Theory of diffraction by small holes", Physical Review **66**, 163–182 (1944).

[9]F. J. García de Abajo, "Colloquium : Light scattering by particle and hole arrays", Reviews of Modern Physics **79**, 1267–1290 (2007).

[10]W. L. Barnes, A. Dereux, and T. W. Ebbesen, "Surface plasmon subwavelength optics", Nature **424**, 824–830 (2003).

[11]V. G. Veselago, "The Electrodynamics of Substances with Simultaneously Negative Values of ϵ and μ", Soviet Physics Uspekhi **10**, 509–514 (1968).

[12]J. B. Pendry, "Negative refraction makes a perfect lens", Physical Review Letters **85**, 3966–3969 (2000).

[13]R. A. Shelby, "Experimental Verification of a Negative Index of Refraction", Science **292**, 77–79 (2001).

[14]J. B. Pendry, A. Aubry, D. R. Smith, and S. A. Maier, "Transformation optics and subwavelength control of light", Science **337**, 549–552 (2012).

[15]A. Alu and N. Engheta, "Plasmonic and metamaterial cloaking: Physical mechanisms and potentials", Journal of Optics A: Pure and Applied Optics **10**, 093002 (2008).

[16]I. Liberal and N. Engheta, "Near-zero refractive index photonics", Nature Photonics **11**, 149–158 (2017).

[17]N. C. Panoiu, W. E. I. Sha, D. Y. Lei, and G.-C. Li, "Nonlinear optics in plasmonic nanostructures", Journal of Optics **20**, 083001 (2018).

[18]R. W. Boyd, *Nonlinear Optics*, 3rd (Academic Press, 2008).

[19]P. E. Powers and J. W. Haus, *Fundamentals of Nonlinear Optics*, 2nd (CRC Press, Boca Raton, 2017).

[20]Y. R. Shen, *Principles of Nonlinear Optics* (John Wiley & Sons, 2002).

[21]P. Butcher and D. Cotter, *The Elements of Nonlinear Optics* (Cambridge University Press, 1990).

[22]T. Verbiest, K. Clays, and V. Rodriguez, *Second-Order Nonlinear Optical Characterization Techniques An Introduction*, 1st (CRC Press, Boca Raton, 2009).

[23]S. Bhagavantam and P. V. Pantulu, "Generalized symmetry and Neumann's principle", Proceedings of the Indian Academy of Sciences - Section A **66**, 33–39 (1967).

[24]J. D. Jackson, *Classical Electrodynamics*, 3rd (John Wiley & Sons, 1998).

[25]Y. R. Shen, "Basic Theory of Surface Sum-Frequency Generation", The Journal of Physical Chemistry C **116**, 15505–15509 (2012).

[26]K. D. Bauer, M. Panholzer, and K. Hingerl, "Bulk quadrupole contribution to second harmonic generation from a microscopic response function", Physica Status Solidi (B) Basic Research **253**, 234–240 (2016).

[27]T. Heinz, "Second-Order Nonlinear Optical Effects at Surfaces and Interfaces", in *Modern problems in condensed matter sciences*, Vol. 29 (Elsevier, Jan. 1991), pp. 353–416.

[28]S. A. Maier, *Plasmonics: Fundamentals and applications* (Springer, 2007).

[29]V. M. Shalaev and S. Kawata, *Nanophotonics with Surface Plasmons* (Elsevier, 2007).

[30]L. Novotny and B. Hecht, *Principles of Nano-Optics* (Cambridge University Press, Cambridge, 2012).

[31]V. Myroshnychenko, J. Rodríguez-Fernández, I. Pastoriza-Santos, A. M. Funston, C. Novo, P. Mulvaney, L. M. Liz-Marzán, and F. J. García de Abajo, "Modelling the optical response of gold nanoparticles", Chemical Society Reviews **37**, 1792 (2008).

[32]C. Kittel, *Introduction To Solid State Physics*, 8th (John Wiley & Sons, 2004).

[33]K. A. Willets and R. P. Van Duyne, "Localized Surface Plasmon Resonance Spectroscopy and Sensing", Annual Review of Physical Chemistry **58**, 267–297 (2007).

[34]V. Amendola, R. Pilot, M. Frasconi, O. M. Maragò, and M. A. Iatì, "Surface plasmon resonance in gold nanoparticles: a review", Journal of Physics: Condensed Matter **29**, 203002 (2017).

[35]V. Giannini, A. I. Fernández-Domínguez, S. C. Heck, and S. A. Maier, "Plasmonic Nanoantennas: Fundamentals and Their Use in Controlling the Radiative Properties of Nanoemitters", Chemical Reviews **111**, 3888–3912 (2011).

[36]N. Daldosso and L. Pavesi, "Nanosilicon photonics", Laser and Photonics Reviews **3**, 508–534 (2009).

[37]J. B. Pendry, A. J. Holden, W. J. Stewart, and I. Youngs, "Extremely Low Frequency Plasmons in Metallic Mesostructures", Physical Review Letters **76**, 4773–4776 (1996).

[38]J. B. Pendry, "A chiral route to negative refraction.", Science **306**, 1353–1355 (2004).

[39]S. S. Oh and O. Hess, "Chiral metamaterials: enhancement and control of optical activity and circular dichroism", En, Nano Convergence **2**, 24 (2015).

[40]J. T. Collins, C. Kuppe, D. C. Hooper, C. Sibilia, M. Centini, and V. K. Valev, "Chirality and Chiroptical Effects in Metal Nanostructures: Fundamentals and Current Trends", Advanced Optical Materials **5**, 1700182–1700227 (2017).

[41]N. Liu, H. Guo, L. Fu, S. Kaiser, H. Schweizer, and H. Giessen, "Three-dimensional photonic metamaterials at optical frequencies", Nature Materials **7**, 31–37 (2008).

[42]N. Liu, H. Liu, S. Zhu, and H. Giessen, "Stereometamaterials", Nature Photonics **3**, 157–162 (2009).

[43]M. Decker, R. Zhao, C. M. Soukoulis, S. Linden, and M. Wegener, "Twisted split-ring-resonator photonic metamaterial with huge optical activity", Optics Letters **35**, 1593 (2010).

[44]J. Valentine, S. Zhang, T. Zentgraf, E. Ulin-Avila, D. A. Genov, G. Bartal, and X. Zhang, "Three-dimensional optical metamaterial with a negative refractive index", Nature **455**, 376–379 (2008).

[45]C. García-Meca, J. Hurtado, J. Martí, A. Martínez, W. Dickson, and A. V. Zayats, "Low-loss multilayered metamaterial exhibiting a negative index of refraction at visible wavelengths", Physical Review Letters **106**, 067402 (2011).

[46]D. R. Smith, S. Schultz, P. Markoš, and C. M. Soukoulis, "Determination of effective permittivity and permeability of metamaterials from reflection and transmission coefficients", Physical Review B - Condensed Matter and Materials Physics **65**, 1–5 (2002).

[47]C. M. Soukoulis and M. Wegener, "Past achievements and future challenges in the development of three-dimensional photonic metamaterials", Nature Photonics **5**, 523–530 (2011).

[48]H.-T. Chen, A. J. Taylor, and N. Yu, "A review of metasurfaces: physics and applications", Reports on Progress in Physics **79**, 076401 (2016).

[49]P. Genevet and F. Capasso, "Holographic optical metasurfaces: a review of current progress", Reports on Progress in Physics **78**, 024401 (2015).

[50]A. E. Minovich, A. E. Miroshnichenko, A. Y. Bykov, T. V. Murzina, D. N. Neshev, and Y. S. Kivshar, "Functional and nonlinear optical metasurfaces", Laser and Photonics Reviews **9**, 195–213 (2015).

[51]A. V. Kildishev, A. Boltasseva, and V. M. Shalaev, "Planar Photonics with Metasurfaces", Science **339**, 1232009–1232009 (2013).

[52]N. Yu and F. Capasso, "Flat optics with designer metasurfaces", Nature Materials **13**, 139–150 (2014).

[53]V. K. Valev, "Characterization of nanostructured plasmonic surfaces with second harmonic generation", Langmuir **28**, 15454–15471 (2012).

[54]M. Kauranen, "Freeing Nonlinear Optics from Phase Matching", Science **342**, 1182–1183 (2013).

[55]V. G. Dmitriev, G. G. Gurzadyan, and D. N. Nikogosyan, *Handbook of Nonlinear Optical Crystals*, Vol. 64, Springer Series in Optical Sciences (Springer Berlin Heidelberg, Berlin, Heidelberg, 1999).

[56]J. Butet, G. Bachelier, I. Russier-Antoine, C. Jonin, E. Benichou, and P.-F. Brevet, "Interference between Selected Dipoles and Octupoles in the Optical Second-Harmonic Generation from Spherical Gold Nanoparticles", Physical Review Letters **105**, 077401 (2010).

[57]J. Butet, J. Duboisset, G. Bachelier, I. Russier-Antoine, E. Benichou, C. Jonin, and P.-F. Brevet, "Optical Second Harmonic Generation of Single Metallic Nanoparticles Embedded in a Homogeneous Medium", Nano Letters **10**, 1717–1721 (2010).

[58]J. Nappa, G. Revillod, I. Russier-Antoine, E. Benichou, C. Jonin, and P. F. Brevet, "Electric dipole origin of the second harmonic generation of small metallic particles", Physical Review B - Condensed Matter and Materials Physics **71**, 165407 (2005).

[59]I. Russier-Antoine, E. Benichou, G. Bachelier, C. Jonin, and P. F. Brevet, "Multipolar Contributions of the Second Harmonic Generation from Silver and Gold Nanoparticles", The Journal of Physical Chemistry C **111**, 9044–9048 (2007).

[60]C. Hubert, L. Billot, P.-M. Adam, R. Bachelot, P. Royer, J. Grand, D. Gindre, K. D. Dorkenoo, and A. Fort, "Role of surface plasmon in second harmonic generation from gold nanorods", Applied Physics Letters **90**, 181105 (2007).

[61]B. Metzger, L. Gui, J. Fuchs, D. Floess, M. Hentschel, and H. Giessen, "Strong Enhancement of Second Harmonic Emission by Plasmonic Resonances at the Second Harmonic Wavelength", Nano Letters **15**, 3917–3922 (2015).

[62]H. Aouani, M. Navarro-Cia, M. Rahmani, T. P. H. Sidiropoulos, M. Hong, R. F. Oulton, and S. A. Maier, "Multiresonant Broadband Optical Antennas As Efficient Tunable Nanosources of Second Harmonic Light", Nano Letters **12**, 4997–5002 (2012).

[63]K. Thyagarajan, S. Rivier, A. Lovera, and O. J. Martin, "Enhanced second-harmonic generation from double resonant plasmonic antennae", Optics Express **20**, 12860 (2012).

[64]M. Celebrano, X. Wu, M. Baselli, S. Großmann, P. Biagioni, A. Locatelli, C. De Angelis, G. Cerullo, R. Osellame, B. Hecht, L. Duò, F. Ciccacci, and M. Finazzi, "Mode matching in multiresonant plasmonic nanoantennas for enhanced second harmonic generation", Nature Nanotechnology **10**, 412–417 (2015).

[65]R. Camacho-Morales, M. Rahmani, S. Kruk, L. Wang, L. Xu, D. A. Smirnova, A. S. Solntsev, A. Miroshnichenko, H. H. Tan, F. Karouta, S. Naureen, K. Vora, L. Carletti, C. De Angelis, C. Jagadish, Y. S. Kivshar, and D. N. Neshev, "Nonlinear Generation of Vector Beams From AlGaAs Nanoantennas", Nano Letters **16**, 7191–7197 (2016).

[66]Y. Tang and A. E. Cohen, "Optical chirality and its interaction with matter", Physical Review Letters **104**, 163901 (2010).

[67]W. T. Kelvin, "The molecular tactics of a crystal", Clarendon Press (1894).

[68]W. T. Kelvin, *Baltimore lectures on molecular dynamics and the wave theory of light*, 1904.

[69]F. Arago, "Mémoire sur une modification remarquable qu'éprouvent les rayons lumineux dans leur passage à travers certains corps diaphanes et sur quelques autres nouveaux phénomènes d'optique", Mémoires de la classe des sciences math. et phys. de l'Institut Impérial de France, 93–134 (1811).

[70]Y. Xu, M. Schnell, and G. Tarczay, "Introduction to the special issue on Chirality-Sensitive Spectroscopy", Journal of Molecular Spectroscopy **356**, 37–38 (2019).

[71]X. Ma, M. Pu, X. Li, Y. Guo, P. Gao, X. Luo, X. Ma, M. Pu, X. Li, Y. Guo, P. Gao, and X. Luo, "Meta-Chirality: Fundamentals, Construction and Applications", Nanomaterials **7**, 116 (2017).

[72]Z. Wang, F. Cheng, T. Winsor, and Y. Liu, "Optical chiral metamaterials: a review of the fundamentals, fabrication methods and applications", Nanotechnology **27**, 412001 (2016).

[73]D. M. Lipkin, "Existence of a new conservation law in electromagnetic theory", Journal of Mathematical Physics **5**, 696–700 (1964).

[74]T. W. Kibble, "Conservation laws for free fields", Journal of Mathematical Physics **6**, 1022–1026 (1965).

[75]Y. Tang and A. E. Cohen, "Enhanced Enantioselectivity in Excitation of Chiral Molecules by Superchiral Light", Science **332**, 333–336 (2011).

[76]P. Guyot-Sionnest, W. Chen, and Y. R. Shen, "General considerations on optical second-harmonic generation from surfaces and interfaces", Physical Review B **33**, 8254–8263 (1986).

[77]N. Abdulrahman, C. D. Syme, C. Jack, A. Karimullah, L. D. Barron, N. Gadegaard, and M. Kadodwala, "The origin of off-resonance non-linear optical activity of a gold chiral nanomaterial", Nanoscale **5**, 12651–12657 (2013).

[78]P. Fischer and A. D. Buckingham, "Surface second-order nonlinear optical activity", Journal of the Optical Society of America B **15**, 2951 (1998).

[79]T. Verbiest, M. Kauranen, Y. Van Rompaey, and A. Persoons, "Optical Activity of Anisotropic Achiral Surfaces", Physical Review Letters **77**, 1456–1459 (1996).

[80]T. Verbiest, M. Kauranen, and A. Persoons, "Optical activity of anisotropic achiral surfaces", Journal of the Optical Society of America B **15**, 451 (1998).

[81]M. Kauranen, S. Van Elshocht, T. Verbiest, A. A. Persoons, S. V. Elshocht, T. Verbiest, and A. A. Persoons, "Tensor analysis of the second-order nonlinear optical susceptibility of chiral anisotropic thin films", Journal of Chemical Physics **112**, 1497–1502 (2000).

[82]S. Sioncke, S. Van Elshocht, T. Verbiest, A. Persoons, M. Kauranen, K. E. S. Phillips, and T. J. Katz, "Optical activity effects in second harmonic generation from anisotropic chiral thin films", The Journal of Chemical Physics **113**, 7578–7581 (2000).

[83]M. J. Huttunen, M. Erkintalo, and M. Kauranen, "Absolute nonlinear optical probes of surface chirality", Journal of Optics A: Pure and Applied Optics **11**, 034006 (2009).

[84]M. J. Huttunen, M. Virkki, M. Erkintalo, E. Vuorimaa, A. Efimov, H. Lemmetyinen, and M. Kauranen, "Absolute probe of surface chirality based on focused circularly polarized light", Journal of Physical Chemistry Letters **1**, 1826–1829 (2010).

[85]E. A. Mamonov, T. V. Murzina, I. A. Kolmychek, A. I. Maydykovsky, V. K. Valev, A. V. Silhanek, E. Ponizovskaya, A. Bratkovsky, T. Verbiest, V. V. Moshchalkov, and O. A. Aktsipetrov, "Coherent and incoherent second harmonic generation in planar G-shaped nanostructures", Optics Letters **36**, 3681 (2011).

[86]E. Mamonov, T. Murzina, I. Kolmychek, A. Maydykovsky, V. Valev, A. Silhanek, T. Verbiest, V. Moshchalkov, and O. Aktsipetrov, "Chirality in nonlinear-optical response of planar G-shaped nanostructures", Optics Express **20**, 8518 (2012).

[87]E. A. Mamonov, I. A. Kolmychek, S. Vandendriessche, M. Hojeij, Y. Ekinci, V. K. Valev, T. Verbiest, and T. V. Murzina, "Anisotropy versus circular dichroism in second harmonic generation from fourfold symmetric arrays of G-shaped nanostructures", Physical Review B **89**, 121113 (2014).

[88]E. Plum, V. A. Fedotov, and N. I. Zheludev, "Optical activity in extrinsically chiral metamaterial", Applied Physics Letters **93**, 191911 (2008).

[89]E. Plum, X. X. Liu, V. A. Fedotov, Y. Chen, D. P. Tsai, and N. I. Zheludev, "Metamaterials: Optical activity without chirality", Physical Review Letters **102**, 113902 (2009).

[90]A. Belardini, M. C. Larciprete, M. Centini, E. Fazio, C. Sibilia, D. Chiappe, C. Martella, A. Toma, M. Giordano, and F. Buatier de Mongeot, "Circular dichroism in the optical second-harmonic emission of curved gold metal nanowires", Physical Review Letters **107**, 257401–257405 (2011).

[91]A. Belardini, M. Centini, G. Leahu, D. C. Hooper, R. Li Voti, E. Fazio, J. W. Haus, A. Sarangan, V. K. Valev, and C. Sibilia, "Chiral light intrinsically couples to extrinsic/pseudo-chiral metasurfaces made of tilted gold nanowires", Scientific Reports **6**, 31796 (2016).

[92]C. M. Soukoulis and M. Wegener, "Past achievements and future challenges in the development of three-dimensional photonic metamaterials", Nature Photonics **5**, 523 (2011).

[93]V. K. Valev, J. J. Baumberg, C. Sibilia, and T. Verbiest, "Chirality and Chiroptical Effects in Plasmonic Nanostructures: Fundamentals, Recent Progress, and Outlook", Advanced Materials **25**, 2517–2534 (2013).

[94]M. Hentschel, M. Schäferling, X. Duan, H. Giessen, and N. Liu, "Chiral plasmonics", Science Advances **3**, e1602735 (2017).

[95]Y. Luo, C. Chi, M. Jiang, R. Li, S. Zu, Y. Li, and Z. Fang, "Plasmonic Chiral Nanostructures: Chiroptical Effects and Applications", Advanced Optical Materials **5**, 1700040 (2017).

[96]E. Hendry, T. Carpy, J. Johnston, M. Popland, R. V. Mikhaylovskiy, a. J. Lapthorn, S. M. Kelly, L. D. Barron, N. Gadegaard, and M. Kadodwala, "Ultrasensitive detection and characterization of biomolecules using superchiral fields", Nature nanotechnology **5**, 783–787 (2010).

[97]M. Schäferling, D. Dregely, M. Hentschel, and H. Giessen, "Tailoring enhanced optical chirality: Design principles for chiral plasmonic nanostructures", Physical Review X **2**, 031010 (2012).

[98]M. Schäferling, X. Yin, N. Engheta, and H. Giessen, "Helical Plasmonic Nanostructures as Prototypical Chiral Near-Field Sources", ACS Photonics **1**, 530–537 (2014).

[99]J. Kaschke, J. K. Gansel, and M. Wegener, "On metamaterial circular polarizers based on metal N-helices.", Optics express **20**, 26012–26020 (2012).

[100]J. K. Gansel, M. Wegener, S. Burger, and S. Linden, "Gold helix photonic metamaterials: a numerical parameter study.", Optics express **18**, 1059–1069 (2010).

[101]W. Li, Z. J. Coppens, L. V. Besteiro, W. Wang, A. O. Govorov, and J. Valentine, "Circularly polarized light detection with hot electrons in chiral plasmonic metamaterials", Nature Communications **6**, 8379 (2015).

[102]T. Narushima, S. Hashiyada, and H. Okamoto, "Nanoscopic Study on Developing Optical Activity with Increasing Chirality for Two-Dimensional Metal Nanostructures", ACS Photonics **1**, 732–738 (2014).

[103]V. K. Valev, J. J. Baumberg, B. De Clercq, N. Braz, X. Zheng, E. J. Osley, S. Vandendriessche, M. Hojeij, C. Blejean, J. Mertens, C. G. Biris, V. Volskiy, M. Ameloot, Y. Ekinci, G. A. E. Vandenbosch, P. A. Warburton, V. V. Moshchalkov, N. C. Panoiu, and T. Verbiest, "Nonlinear Superchiral Meta-Surfaces: Tuning Chirality and Disentangling Non-Reciprocity at the Nanoscale", Advanced Materials **26**, 4074–4081 (2014).

[104]S. Chen, F. Zeuner, M. Weismann, B. Reineke, G. Li, V. K. Valev, K. W. Cheah, N. C. Panoiu, T. Zentgraf, and S. Zhang, "Giant Nonlinear Optical Activity of Achiral Origin in Planar Metasurfaces with Quadratic and Cubic Nonlinearities", Advanced Materials **28**, 2992–2999 (2016).

[105]S. Zu, Y. Bao, and Z. Fang, "Planar plasmonic chiral nanostructures", Nanoscale **8**, 3900–3905 (2016).

[106]M. Kuwata-Gonokami, N. Saito, Y. Ino, M. Kauranen, K. Jefimovs, T. Vallius, J. Turunen, and Y. Svirko, "Giant Optical Activity in Quasi-Two-Dimensional Planar Nanostructures", Physical review letters **95**, 1–4 (2005).

[107]E. Plum, V. A. Fedotov, A. S. Schwanecke, N. I. Zheludev, and Y. Chen, "Giant optical gyrotropy due to electromagnetic coupling", Applied Physics Letters **90**, 223113 (2007).

[108]D.-H. Kwon, P. L. Werner, and D. H. Werner, "Optical planar chiral metamaterial designs for strong circular dichroism and polarization rotation", Optics Express **16**, 11802 (2008).

[109]Y. Cui, L. Kang, S. Lan, S. Rodrigues, and W. Cai, "Giant Chiral Optical Response from a Twisted-Arc Metamaterial", Nano Letters **14**, 1021–1025 (2014).

[110]A. S. Karimullah, C. Jack, R. Tullius, V. M. Rotello, G. Cooke, N. Gadegaard, L. D. Barron, and M. Kadodwala, "Disposable Plasmonics: Plastic Templated Plasmonic Metamaterials with Tunable Chirality", Advanced Materials **27**, 5610–5616 (2015).

[111]M. Decker, R. Zhao, C. M. Soukoulis, S. Linden, and M. Wegener, "Twisted split-ring-resonator photonic metamaterial with huge optical activity.", Optics letters **35**, 1593 (2010).

[112]M. Hentschel, M. Schäferling, T. Weiss, N. Liu, and H. Giessen, "Three-Dimensional Chiral Plasmonic Oligomers", Nano letters **12**, 2542–2547 (2012).

[113]M. Hentschel, L. Wu, M. Schäferling, P. Bai, E. P. Li, and H. Giessen, "Optical Properties of Chiral Three-Dimensional Plasmonic Oligomers at the Onset of Charge-Transfer Plasmons", ACS Nano **6**, 10355–10365 (2012).

[114]J. A. Dolan, B. D. Wilts, S. Vignolini, J. J. Baumberg, U. Steiner, and T. D. Wilkinson, "Optical Properties of Gyroid Structured Materials: From Photonic Crystals to Metamaterials", Advanced Optical Materials **3**, 12–32 (2015).

[115]M. Esposito, V. Tasco, F. Todisco, M. Cuscunà, A. Benedetti, D. Sanvitto, and A. Passaseo, "Triple-helical nanowires by tomographic rotatory growth for chiral photonics", Nature Communications **6**, 6484 (2015).

[116]J. G. Gibbs, A. G. Mark, S. Eslami, and P. Fischer, "Plasmonic nanohelix metamaterials with tailorable giant circular dichroism", Applied Physics Letters **103**, 213101 (2013).

[117]V. Tasco, M. Esposito, F. Todisco, A. Benedetti, M. Cuscunà, D. Sanvitto, and A. Passaseo, "Three-dimensional nanohelices for chiral photonics", Applied Physics A **122**, 280 (2016).

[118]J. Kaschke, L. Blume, L. Wu, M. Thiel, K. Bade, Z. Yang, and M. Wegener, "A Helical Metamaterial for Broadband Circular Polarization Conversion", Advanced Optical Materials **3**, 1411–1417 (2015).

[119]J. Kaschke, M. Blome, S. Burger, and M. Wegener, "Tapered N-helical metamaterials with three-fold rotational symmetry as improved circular polarizers.", EN, Optics express **22**, 19936–46 (2014).

[120]T. Petralli-Mallow, T. M. Wong, J. D. Byers, H. I. Yee, and J. M. Hicks, "Circular dichroism spectroscopy at interfaces: A surface second harmonic generation study", Journal of Physical Chemistry **97**, 1383–1388 (1993).

[121]T. Verbiest, M. Kauranen, A. Persoons, M. Ikonen, J. Kurkela, and H. Lemmetyinen, "Nonlinear Optical Activity and Biomolecular Chirality", Journal of the American Chemical Society **116**, 9203–9205 (1994).

[122]J. D. Byers, H. I. Yee, T. Petralli-Mallow, and J. M. Hicks, "Second-harmonic generation circular-dichroism spectroscopy from chiral monolayers", Physical Review B **49**, 14643–14647 (1994).

[123]J. G. Gibbs, A. G. Mark, T.-C. Lee, S. Eslami, D. Schamel, and P. Fischer, "Nanohelices by shadow growth.", Nanoscale **6**, 9457–9466 (2014).

[124]J. P. Spatz, S. Mössmer, C. Hartmann, M. Möller, T. Herzog, M. Krieger, H. G. Boyen, P. Ziemann, and B. Kabius, "Ordered deposition of inorganic clusters from micellar block copolymer films", Langmuir **16**, 407–415 (2000).

[125]R. Glass, M. Möller, and J. P. Spatz, "Block copolymer micelle nanolithography", Nanotechnology **14**, 1153–1160 (2003).

[126]A. G. Mark, J. G. Gibbs, T.-C. C. Lee, and P. Fischer, "Hybrid nanocolloids with programmed three-dimensional shape and material composition.", Nature materials **12**, 802–807 (2013).

[127]J. T. Collins, D. C. Hooper, A. G. Mark, C. Kuppe, and V. K. Valev, "Second-Harmonic Generation Optical Rotation Solely Attributable to Chirality in Plasmonic Metasurfaces", ACS Nano **12**, 5445–5451 (2018).

[128]M. Kauranen and A. V. Zayats, "Nonlinear plasmonics", Nature Photonics **6**, 737–748 (2012).

[129]J. Butet, P.-F. Brevet, and O. J. F. Martin, "Optical Second Harmonic Generation in Plasmonic Nanostructures: From Fundamental Principles to Advanced Applications", ACS nano **9**, 10545–10562 (2015).

[130]T. Shibanuma, G. Grinblat, P. Albella, and S. A. Maier, "Efficient Third Harmonic Generation from Metal-Dielectric Hybrid Nanoantennas", Nano Letters **17**, 2647–2651 (2017).

[131]W. Fan, S. Zhang, N. C. Panoiu, A. Abdenour, S. Krishna, R. M. Osgood, K. J. Malloy, and S. R. Brueck, "Second harmonic generation from a nanopatterned isotropic nonlinear material", Nano Letters **6**, 1027–1030 (2006).

[132]S. Berweger, J. M. Atkin, X. G. Xu, R. L. Olmon, and M. B. Raschke, "Femtosecond nanofocusing with full optical waveform control", Nano Letters **11**, 4309–4313 (2011).

[133]V. K. Valev, N. Smisdom, A. V. Silhanek, B. De Clercq, W. Gillijns, M. Ameloot, V. V. Moshchalkov, and T. Verbiest, "Plasmonic ratchet wheels: Switching circular dichroism by arranging chiral nanostructures", EN, Nano Letters **9**, 3945–3948 (2009).

[134]G. Bautista, C. Dreser, X. Zang, D. P. Kern, M. Kauranen, and M. Fleischer, "Collective Effects in Second-Harmonic Generation from Plasmonic Oligomers", Nano Letters **18**, 2571–2580 (2018).

[135]V. K. Valev, D. Denkova, X. Zheng, A. I. Kuznetsov, C. Reinhardt, B. N. Chichkov, G. Tsutsumanova, E. J. Osley, V. Petkov, B. De Clercq, A. V. Silhanek, Y. Jeyaram, V. Volskiy, P. A. Warburton, G. A. E. Vandenbosch, S. Russev, O. A. Aktsipetrov, M. Ameloot, V. V. Moshchalkov, and T. Verbiest, "Plasmon-enhanced Sub-wavelength laser ablation: Plasmonic nanojets", Advanced Materials **24**, OP29–OP35 (2012).

[136]S. Chen, G. Li, F. Zeuner, W. H. Wong, E. Y. B. Pun, T. Zentgraf, K. W. Cheah, and S. Zhang, "Symmetry-Selective Third-Harmonic Generation from Plasmonic Metacrystals", Physical Review Letters **113**, 033901–033905 (2014).

[137]G. Bautista and M. Kauranen, "Vector-Field Nonlinear Microscopy of Nanostructures", ACS Photonics **3**, 1351–1370 (2016).

[138]S.-P. Tai, Y. Wu, D.-B. Shieh, L.-J. Chen, K.-J. Lin, C.-H. Yu, S.-W. Chu, C.-H. Chang, X.-Y. Shi, Y.-C. Wen, K.-H. Lin, T.-M. Liu, and C.-K. Sun, "Molecular Imaging of Cancer Cells Using Plasmon-Resonant-Enhanced Third-Harmonic-Generation in Silver Nanoparticles", Advanced Materials **19**, 4520–4523 (2007).

[139]V. K. Valev, B. De Clercq, C. G. Biris, X. Zheng, S. Vandendriessche, M. Hojeij, D. Denkova, Y. Jeyaram, N. C. Panoiu, Y. Ekinci, A. V. Silhanek, V. Volskiy, G. A. E. E. Vandenbosch, M. Ameloot, V. V. Moshchalkov, and T. Verbiest, "Distributing the optical near-field for efficient field-enhancements in nanostructures", Advanced Materials **24**, OP208–OP215 (2012).

[140]D. C. Hooper, A. G. Mark, C. Kuppe, J. T. Collins, P. Fischer, and V. K. Valev, "Strong Rotational Anisotropies Affect Nonlinear Chiral Metamaterials", Advanced Materials **29**, 1605110 (2017).

[141]V. K. Valev, A. V. Silhanek, W. Gillijns, Y. Jeyaram, H. Paddubrouskaya, A. Volodin, C. G. Biris, N. C. Panoiu, B. De Clercq, M. Ameloot, O. A. Aktsipetrov, V. V. Moshchalkov, and T. Verbiest, "Plasmons reveal the direction of magnetization in nickel nanostructures", ACS Nano **5**, 91–96 (2011).

[142]W. Zheng, X. Liu, A. T. Hanbicki, B. T. Jonker, and G. Lüpke, "Nonlinear magnetoplasmonics", Optical Materials Express **5**, 2597 (2015).

[143]S. Kruk, M. Weismann, A. Y. Bykov, E. A. Mamonov, I. A. Kolmychek, T. Murzina, N. C. Panoiu, D. N. Neshev, and Y. S. Kivshar, "Enhanced Magnetic Second-Harmonic Generation from Resonant Metasurfaces", ACS Photonics **2**, 1007–1012 (2015).

[144]E. Almeida, G. Shalem, and Y. Prior, "Subwavelength nonlinear phase control and anomalous phase matching in plasmonic metasurfaces", Nature Communications **7**, 10367 (2016).

[145]J. Lee, M. Tymchenko, C. Argyropoulos, P. Y. Chen, F. Lu, F. Demmerle, G. Boehm, M. C. Amann, A. Alù, and M. A. Belkin, "Giant nonlinear response from plasmonic metasurfaces coupled to intersubband transitions", Nature **511**, 65–69 (2014).

[146]G. Li, S. Zhang, and T. Zentgraf, "Nonlinear photonic metasurfaces", Nature Reviews Materials **2**, 17010–17023 (2017).

[147]J. Chen, K. Wang, H. Long, X. Han, H. Hu, W. Liu, B. Wang, and P. Lu, "Tungsten Disulfide-Gold Nanohole Hybrid Metasurfaces for Nonlinear Metalenses in the Visible Region", Nano Letters **18**, 1344–1350 (2018).

[148]C. Schlickriede, N. Waterman, B. Reineke, P. Georgi, G. Li, S. Zhang, and T. Zentgraf, "Imaging through Nonlinear Metalens Using Second Harmonic Generation", Advanced Materials **30**, 1703843 (2018).

[149]K. T. Carron, W. Fluhr, M. Meier, A. Wokaun, and H. W. Lehmann, "Resonances of two-dimensional particle gratings in surface-enhanced Raman scattering", Journal of the Optical Society of America B **3**, 430 (1986).

[150]S. Zou and G. C. Schatz, "Narrow plasmonic/photonic extinction and scattering line shapes for one and two dimensional silver nanoparticle arrays", Journal of Chemical Physics **121**, 12606–12612 (2004).

[151]E. M. Hicks, S. Zou, G. C. Schatz, K. G. Spears, R. P. Van Duyne, L. Gunnarsson, T. Rindzevicius, B. Kasemo, and M. Käll, "Controlling plasmon line shapes through diffractive coupling in linear arrays of cylindrical nanoparticles fabricated by electron beam lithography", Nano Letters **5**, 1065–1070 (2005).

[152]B. Auguié and W. L. Barnes, "Collective resonances in gold nanoparticle arrays", Physical Review Letters **101**, 143902 (2008).

[153]W. Wang, M. Ramezani, A. I. Väkeväinen, P. Törmä, J. G. Rivas, and T. W. Odom, "The rich photonic world of plasmonic nanoparticle arrays", Materials Today **21**, 303–314 (2018).

[154]R. Czaplicki, A. Kiviniemi, J. Laukkanen, J. Lehtolahti, M. Kuittinen, and M. Kauranen, "Surface lattice resonances in second-harmonic generation from metasurfaces", Optics Letters **41**, 2684 (2016).

[155]L. Michaeli, S. Keren-Zur, O. Avayu, H. Suchowski, and T. Ellenbogen, "Nonlinear Surface Lattice Resonance in Plasmonic Nanoparticle Arrays", Physical Review Letters **118**, 243904 (2017).

[156]V. G. Kravets, F. Schedin, A. V. Kabashin, and A. N. Grigorenko, "Sensitivity of collective plasmon modes of gold nanoresonators to local environment.", Optics letters **35**, 956–958 (2010).

[157]B. Spackova, P. Wrobel, M. Bockova, and J. Homola, "Optical Biosensors Based on Plasmonic Nanostructures: A Review", Proceedings of the IEEE **104**, 2380–2408 (2016).

[158]R. R. Gutha, S. M. Sadeghi, C. Sharp, and W. J. Wing, "Biological sensing using hybridization phase of plasmonic resonances with photonic lattice modes in arrays of gold nanoantennas", Nanotechnology **28**, 355504 (2017).

[159]K. S. Lee and M. A. El-Sayed, "Gold and silver nanoparticles in sensing and imaging: Sensitivity of plasmon response to size, shape, and metal composition", Journal of Physical Chemistry B **110**, 19220–19225 (2006).

[160]A. I. Kuznetsov, A. B. Evlyukhin, M. R. Gonçalves, C. Reinhardt, A. Koroleva, M. L. Arnedillo, R. Kiyan, O. Marti, and B. N. Chichkov, "Laser Fabrication of Large-Scale Nanoparticle Arrays for Sensing Applications", ACS Nano **5**, 4843–4849 (2011).

[161]M. Svedendahl, S. Chen, A. Dmitriev, and M. Käll, "Refractometric sensing using propagating versus localized surface plasmons: A direct comparison", Nano Letters **9**, 4428–4433 (2009).

[162]P. Offermans, M. C. Schaafsma, S. R. Rodriguez, Y. Zhang, M. Crego-Calama, S. H. Brongersma, and J. Gómez Rivas, "Universal scaling of the figure of merit of plasmonic sensors", ACS Nano **5**, 5151–5157 (2011).

[163]B. Špačková and J. Homola, "Sensing properties of lattice resonances of 2D metal nanoparticle arrays: An analytical model", Optics Express **21**, 27490 (2013).

[164]S. Zou, N. Janel, and G. C. Schatz, "Silver nanoparticle array structures that produce remarkably narrow plasmon lineshapes", Journal of Chemical Physics **120**, 10871–10875 (2004).

[165]V. A. Markel, "Comment on "Silver nanoparticle array structures that produce remarkably narrow plasmon line shapes" [J. Chem. Phys. 120 10871 (2004)]", Journal of Chemical Physics **122**, 097101 (2005).

[166]S. Zou and G. C. Schatz, "Response to "Comment on 'Silver nanoparticle array structures that produce remarkable narrow plasmon line shapes' "", The Journal of Chemical Physics **122**, 97102 (2005).

[167]J. Li, J. Ye, C. Chen, Y. Li, N. Verellen, V. V. Moshchalkov, L. Lagae, and P. Van Dorpe, "Revisiting the surface sensitivity of nanoplasmonic biosensors", ACS Photonics **2**, 425–431 (2015).

[168]D. Wang, M. R. Bourgeois, W. K. Lee, R. Li, D. Trivedi, M. P. Knudson, W. Wang, G. C. Schatz, and T. W. Odom, "Stretchable Nanolasing from Hybrid Quadrupole Plasmons", Nano Letters **18**, 4549–4555 (2018).

[169]J. Butet, G. Bachelier, I. Russier-Antoine, C. Jonin, E. Benichou, and P.-F. Brevet, "Interference between Selected Dipoles and Octupoles in the Optical Second-Harmonic Generation from Spherical Gold Nanoparticles", Physical Review Letters **105**, 077401 (2010).

[170]J. Nappa, I. Russier-Antoine, E. Benichou, C. Jonin, and P. F. Brevet, "Wavelength dependence of the retardation effects in silver nanoparticles followed by polarization resolved hyper Rayleigh scattering", Chemical Physics Letters **415**, 246–250 (2005).

[171]J. Nappa, I. Russier-Antoine, E. Benichou, C. Jonin, and P. F. Brevet, "Second harmonic generation from small gold metallic particles: From the dipolar to the quadrupolar response", Journal of Chemical Physics **125**, 184712 (2006).

[172]G. Bachelier, J. Butet, I. Russier-Antoine, C. Jonin, E. Benichou, and P. F. Brevet, "Origin of optical second-harmonic generation in spherical gold nanoparticles: Local surface and nonlocal bulk contributions", Physical Review B - Condensed Matter and Materials Physics **82**, 235403 (2010).

[173]A. B. Evlyukhin, C. Reinhardt, U. Zywietz, and B. N. Chichkov, "Collective resonances in metal nanoparticle arrays with dipole-quadrupole interactions", Physical Review B - Condensed Matter and Materials Physics **85**, 245411 (2012).

[174]I. Russier-Antoine, E. Benichou, G. Bachelier, C. Jonin, and P. F. Brevet, "Multipolar contributions of the second harmonic generation from silver and gold nanoparticles", The Journal of Physical Chemistry C **111**, 9044–9048 (2007).

[175]D. Smirnova and Y. S. Kivshar, "Multipolar nonlinear nanophotonics", Optica **3**, 1241 (2016).

[176]D. Timbrell, J. W. You, Y. S. Kivshar, and N. C. Panoiu, "A comparative analysis of surface and bulk contributions to second-harmonic generation in centrosymmetric nanoparticles", Scientific Reports **8**, 3586 (2018).

[177]R. Adato, A. A. Yanik, J. J. Amsden, D. L. Kaplan, F. G. Omenetto, M. K. Hong, S. Erramilli, and H. Altug, "Ultra-sensitive vibrational spectroscopy of protein monolayers with plasmonic nanoantenna arrays", Proceedings of the National Academy of Sciences **106**, 19227–19232 (2009).

[178]*Lumerical Inc. http://www.lumerical.com/tcad-products/fdtd/.*

[179]J. I. Dadap, J. Shan, and T. F. Heinz, "Theory of optical second-harmonic generation from a sphere of centrosymmetric material: small-particle limit", Journal of the Optical Society of America B **21**, 1328–1347 (2004).

[180]G. Vecchi, V. Giannini, and J. Gómez Rivas, "Shaping the Fluorescent Emission by Lattice Resonances in Plasmonic Crystals of Nanoantennas", Physical Review Letters **102**, 146807 (2009).

[181]R. J. Green, R. A. Frazier, K. M. Shakesheff, M. C. Davies, C. J. Roberts, and S. J. B. Tendler, "Surface plasmon resonance analysis of dynamic biological interactions with biomaterials", Biomaterials **21**, 1823–1835 (2000).

[182]M. J. Huttunen, P. Rasekh, R. W. Boyd, and K. Dolgaleva, "Using surface lattice resonances to engineer nonlinear optical processes in metal nanoparticle arrays", Physical Review A **97**, 53817 (2018).

[183]P. Guyot-Sionnest and Y. R. Shen, "Bulk contribution in surface second-harmonic generation", Physical Review B **38**, 7985–7989 (1988).

[184]G. Bachelier, I. Russier-Antoine, E. Benichou, C. Jonin, and P.-F. Brevet, "Multipolar second-harmonic generation in noble metal nanoparticles", Journal of the Optical Society of America B **25**, 955 (2008).

[185]J. Nappa, G. Revillod, I. Russier-Antoine, E. Benichou, C. Jonin, and P. F. Brevet, "Electric dipole origin of the second harmonic generation of small metallic particles", Physical Review B **71**, 165407 (2005).

[186]C. P. Burrows and W. L. Barnes, "Large spectral extinction due to overlap of dipolar and quadrupolar plasmonic modes of metallic nanoparticles in arrays.", Optics express **18**, 3187–98 (2010).

[187]M. Kataja, T. K. Hakala, A. Julku, M. J. Huttunen, S. van Dijken, and P. Törmä, "Surface lattice resonances and magneto-optical response in magnetic nanoparticle arrays.", en, Nature communications **6**, 7072 (2015).

[188]J. Li, J. Ye, C. Chen, L. Hermans, N. Verellen, J. Ryken, H. Jans, W. Van Roy, V. V. Moshchalkov, L. Lagae, and P. Van Dorpe, "Biosensing using diffractively coupled plasmonic crystals: The figure of merit revisited", Advanced Optical Materials **3**, 176–181 (2015).

[189]S. M. Sadeghi, W. J. Wing, and Q. Campbell, "Normal and anomalous plasmonic lattice modes of gold nanodisk arrays in inhomogeneous media", Journal of Applied Physics **119**, 114307 (2016).

[190]R. Guo, T. K. Hakala, and P. Törmä, "Geometry dependence of surface lattice resonances in plasmonic nanoparticle arrays", Physical Review B **95**, 155423 (2017).

[191]S. Baur, S. Sanders, and A. Manjavacas, "Hybridization of Lattice Resonances", ACS Nano **12**, 1618–1629 (2018).

[192]M. Kataja, S. Pourjamal, N. Maccaferri, P. Vavassori, T. K. Hakala, M. J. Huttunen, P. Törmä, and S. van Dijken, "Hybrid plasmonic lattices with tunable magneto-optical activity.", Optics express **24**, 3652–62 (2016).

Appendix A

Diffraction edge derivation

In this appendix a general expression for the Rayleigh anomaly dispersion is derived. We start with Equation 6.1 from Chapter 6,

$$\mathbf{k}' = \mathbf{k_{inc\parallel}} + \mathbf{G}, \tag{A.1}$$

where $\mathbf{k}'$ is the wave vector of the diffracted beam, $\mathbf{k_{inc\parallel}}$ is the in-plane wave vector component of the incident beam. $\mathbf{G}$ is a sum of the reciprocal lattice vectors. Decomposing the incident wave vector into its in-plane components and using the full expression for $\mathbf{G}$ yields,

$$\mathbf{k}' = \mathbf{k_{inc}}\sin(\theta)\sin(\phi) + \beta\mathbf{b}^* + \mathbf{k_{inc}}\sin(\theta)\cos(\phi) + \alpha\mathbf{a}^*, \tag{A.2}$$

where ϕ is the azimuthal angle and, θ is the the polar angle. The magnitude of the incident and scattered wave vectors must be equal which leads to,

$$\mathbf{k}'^2 = (\mathbf{k_{inc}}\sin(\theta)\sin(\phi) + \beta\mathbf{b}^*)^2 + (\mathbf{k_{inc}}\sin(\theta)\cos(\phi) + \alpha\mathbf{a}^*)^2. \tag{A.3}$$

We can now examine specific cases before finding a general expression in terms of wavelength. Consider the case where, $\alpha = 0$, $\phi = \pi/2$ such that Equation A.3 can be written as,

$$\mathbf{k}'^2 = (\mathbf{k_{inc}}\sin(\theta)\sin(\phi) + \beta\mathbf{b}^*)^2, \tag{A.4}$$

and then expanded to give,

$$k'^2 = k_{inc}^2 \sin^2(\theta) + 2k_{inc}\sin(\theta)\beta b^* + \beta^2 b^{*2}. \tag{A.5}$$

Equation A.5 can be expanded in terms of wavelength using the following relations:$|k'| = \frac{2\pi n}{\lambda}$, $|k_{inc}| = \frac{2\pi}{\lambda}$, $|b^*| = \frac{2\pi}{b}$, where n is the refractive index of the environment surrounding the lattice, λ is the vacuum wavelength and, b is the magnitude of the real space lattice vector. Substituting these expressions into A.5 yields,

$$\frac{4\pi^2 n^2}{\lambda^2} = \frac{4\pi^2}{\lambda^2}\sin^2(\theta) + \frac{8\pi^2\beta}{\lambda b}\sin(\theta) + \frac{4\pi^2\beta^2}{b^2}, \tag{A.6}$$

which can be rewritten as,

$$n^2 b^2 = b^2 \sin^2(\theta) + 2\beta\lambda b \sin(\theta) + \lambda^2\beta^2. \tag{A.7}$$

We rearrange Equation A.7 into a quadratic equation in λ and solve using the quadratic formula as follow,

$$\lambda^2\beta^2 + 2\beta\lambda b\sin(\theta) + b^2(\sin^2(\theta) - n^2) = 0, \tag{A.8}$$

$$\lambda = \frac{-2\beta b\sin(\theta) \pm \sqrt{4\beta^2 b^2\sin^2(\theta) - 4\beta^2 b^2(\sin^2(\theta) - n^2)}}{2\beta^2}, \tag{A.9}$$

$$\lambda = \frac{-b\sin(\theta)}{\beta} \pm \sqrt{\frac{b^2\sin^2(\theta)}{\beta^2} - \frac{b^2(\sin^2(\theta) - n^2)}{\beta^2}}, \tag{A.10}$$

$$\lambda = \frac{-b\sin(\theta)}{\beta} \pm \sqrt{\frac{n^2}{\beta^2}}, \tag{A.11}$$

$$\lambda = b\left(\frac{n}{|\beta|} - \frac{\sin(\theta)}{\beta}\right). \tag{A.12}$$

Where the negative solution can be disregarded because it is unphysical.

Next we consider the case: $\beta = 0$, $\phi = 0$ which allows Equation A.3 to be written as,

$$\mathbf{k}'^2 = (\mathbf{k_{inc}}\sin(\theta))^2 + (\alpha\mathbf{a})^2, \tag{A.13}$$

$$k'^2 = k_{inc}2\sin^2(\theta) + \alpha^2 a^{*2}). \tag{A.14}$$

Equation A.14 can be written ins term of wavelength using the same substitutions as in the previous case and $|a^*| = \frac{2\pi}{a}$ where a is the magnitude of a real space lattice vector. In terms of wavelength we obtain,

$$\frac{4\pi^2 n^2}{\lambda^2} = \frac{4\pi^2}{\lambda^2}\sin^2(\theta) + \frac{4\pi^2\alpha^2}{a^2}, \tag{A.15}$$

which can be rewritten as,

$$n^2a^2 = a^2\sin^2(\theta) + \lambda^2\alpha^2. \tag{A.16}$$

Following the same procedure as in the previous case we find a quadratic equation in terms of λ and then solve,

$$\lambda^2\alpha^2 + a^2(\sin^2(\theta) - n^2) = 0, \tag{A.17}$$

$$\lambda = \frac{a}{|\alpha|}\sqrt{(\sin^2(\theta) - n^2)} \tag{A.18}$$

We shall consider the general case with no restriction on ϕ or in the values that the integers α and β can take. We start with Equation A.3 which we expand further,

$$\mathbf{k'}^2 = (\mathbf{k_{inc}}\sin(\theta)\sin(\phi) + \beta\mathbf{b}^*)^2 + (\mathbf{k_{inc}}\sin(\theta)\cos(\phi) + \alpha\mathbf{a}^*)^2, \tag{A.19}$$

$$\begin{aligned} k'^2 = {} & k_{inc}^2\sin^2(\theta)\sin^2(\phi) + 2k_{inc}\sin(\theta)\sin(\phi)\beta b^* + \beta^2 b^{*2} \\ & + k_{inc}^2\sin^2(\theta)\cos^2(\phi) + 2k_{inc}\sin(\theta)\cos(\phi)\alpha a^* + \alpha^2 a^{*2}, \end{aligned} \tag{A.20}$$

$$\begin{aligned} k'^2 = {} & k_{inc}^2\sin^2(\theta)(\sin^2(\phi) + \cos^2(\phi)) \\ & + 2k_{inc}\sin(\theta)(\sin(\phi)\beta b^* + \cos(\phi)\alpha a^*) + \beta^2 b^{*2} + \alpha^2 a^{*2}. \end{aligned} \tag{A.21}$$

We use the substitutions from the previous cases to obtain,

$$\begin{aligned} \frac{4\pi^2 n^2}{\lambda^2} = {} & \frac{4\pi^2}{\lambda^2}\sin^2(\theta) + \frac{4\pi}{\lambda}\sin(\theta)(\frac{2\pi}{b}\beta\sin(\phi) + \frac{2\pi}{a}\alpha\cos(\phi)) \\ & + \frac{4\pi^2}{b^2}\beta^2 + \frac{4\pi^2}{a^2}\alpha^2, \end{aligned} \tag{A.22}$$

which can then rearranged to get a quadratic equation in λ as follows,

$$a^2b^2n^2 = a^2b^2\sin^2(\theta) + 2\lambda\sin(\theta)a^2b^2(\frac{\beta}{b}\sin(\phi) + \frac{\alpha}{a}\cos(\phi)) + \lambda^2(a^2\beta^2 + b^2\alpha^2), \quad \text{(A.23)}$$

$$a^2b^2n^2 = a^2b^2\sin^2(\theta) + 2\lambda\sin(\theta)(a^2b\beta\sin(\phi) + ab^2\alpha\cos(\phi)) + \lambda^2(a^2\beta^2 + b^2\alpha^2) \quad \text{(A.24)}$$

$$\lambda^2(a^2\beta^2 + b^2\alpha^2) + 2\lambda\sin(\theta)(a^2b\beta\sin(\phi) + ab^2\alpha\cos(\phi)) + a^2b^2(\sin^2(\theta) - n^2) = 0. \quad \text{(A.25)}$$

Using the quadratic formula we find the solution,

$$\lambda = \frac{-2\sin(\theta)(a^2b\beta\sin(\phi) + ab^2\alpha\cos(\phi))}{2(a^2\beta^2 + b^2\alpha^2)} \pm \sqrt{\frac{4\sin^2(\theta)(a^2b\beta\sin(\phi) + ab^2\alpha\cos(\phi))^2 - 4(a^2\beta^2 + b^2\alpha^2)(a^2b^2(\sin^2(\theta) - n^2))}{4(a^2\beta^2 + b^2\alpha^2)^2}}, \quad \text{(A.26)}$$

which is rather unwieldy. The solution becomes more tractable is we use the expressions,

$$P = (a^2\beta^2 + b^2\alpha^2), \quad \text{(A.27)}$$

and

$$Q = (a^2b\beta\sin(\phi) + ab^2\alpha\cos(\phi)). \quad \text{(A.28)}$$

Now we can write the solution for λ as,

$$\lambda = \frac{-\sin(\theta)Q}{P} \pm \sqrt{\frac{\sin^2(\theta)Q^2}{P^2} - \frac{a^2b^2(\sin^2(\theta) - n^2)}{P}}. \quad \text{(A.29)}$$

Appendix B

Power dependence tests

When conducting second harmonic generation experiments it is important to verify that the measured signal is SHG. As discussed in Chapter 2 SHG has a quadratic a quadratic dependence on the amplitude of the incident electric field. In terms of more easily measurable quantities, this means that the intensity of any detected SHG depends quadratically on the incident power. Therefore, in order to test for SHG the signal is measured at different incident powers. The results are then fitted to a power law $y = ax^b$, where y is the measured signal, x is the incident power, a and b are free fitting parameters.

B.1 Nanoparticle arrays

A power dependence test for the nanoparticle arrays discussed in 6 is presented in Figure B.1. The test was performed on the silver array with 600 nm spacing, at a wavelength of 760 nm. A narrow bandpass filter centred at 380 nm (Thorlabs FB380-10, FWHM 10 nm, typical transmission 25%) rejected extraneous light. The fitting routine (python module scipy curve fit) returned parameter values of $a = 210.4$ and $b = 1.7$ with an R-squared value of $R^2 = 0.998$. The value of the exponent is close to a value of 2, therefore the measured signal is SHG.

Damage threshold tests were also performed on the sample, again at a wavelength of 760 nm. The average powers tested were: 20 mW, 15 mW, 10 mW, 5 mW, 1 mW, and 0.5 mW. The laser spot size was 50 μm. Following illumination, the sample was inspected using an optical microscope in dark field reflection mode. Damage caused by 20 mW,

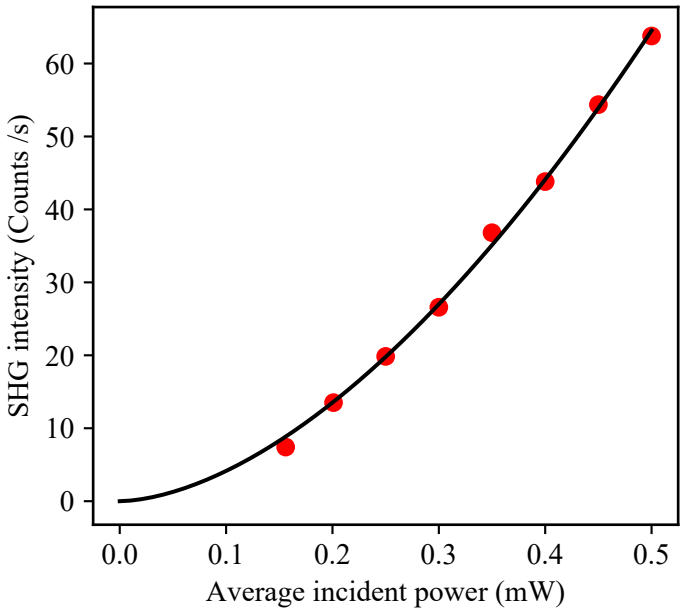

Figure B.1: Power dependence test on 600 nm silver nanoparticle array. Red dots are measured data points. Black solid line is the fitted curve.

15 mW and, 10 mW is easily identified at ×10 and ×20 magnifications in Figure B.2. The regions of illumination were evenly spaced and there is no evidence that powers of 5 mW and below caused any damage. As an incident power of 0.5 mW was used, it can be concluded that the experiments were conducted below the laser damage threshold of the samples.

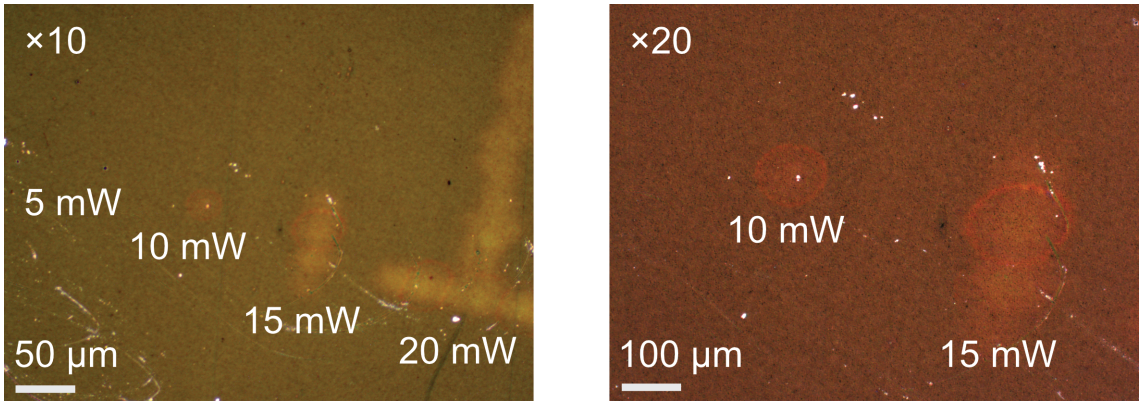

Figure B.2: Damage threshold tests performed on the 600 nm silver nanoparticle array. Images taken using a Zeiss Axio Imager M2 microscope in dark field reflection mode.

B.2 Nanohelices

Results for the power dependence test on the nanohelices (TI540A) are presented in Figure B.3. The helices were illuminated with 800 nm P-polarised light at a 45° angle of incidence. The fitting routine (python module scipy curve fit) returned parameter values of $a = 42.7$ and $b = 2.04$ with an R-squared value of $R^2 = 0.998$. The value of the exponent is close to a value of 2, therefore the measured signal is SHG.

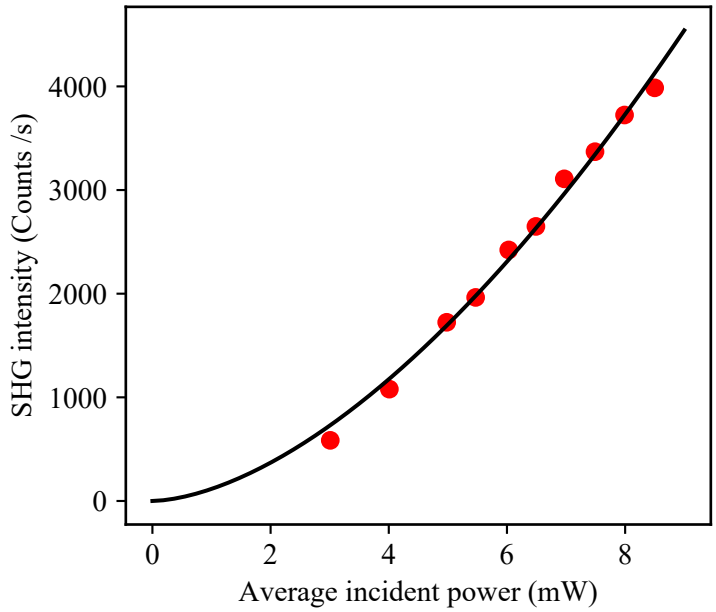

Figure B.3: Power dependence test on the nanohelices. Red dots are measured data points. Black solid line is the fitted curve.

Appendix C

Photon Counter Settings

The photon counting mode is set to "A and B for T-set", so that each channel counts separately for time T-set. Both gates are set to "CW" mode, so that they are continuously counting for the duration of T-set. The system is then set counting, if counts occur the discrimination level is increased after it has finished. This process is repeated until number of dark counts is satisfactorily low. If no counts occurred during the initial run, then the discrimination level is decreased. The discrimination level should not be set high enough to reject actual signal pulses but only dark counts and electrical noise.

Once the gate discrimination levels have been set the gate timings need to be set. The photon counting mode remains "A and B for T-set". However, both gates are set to "gated" mode, instead of "CW". The time duration of the gate width is generally determined by the frequency and duty cycle of the chopper wheel. For a chopper wheel with a duty cycle of 1.7% at a frequency of 42 Hz the chopper window is open for approximately 400 μs. The gate width can be made shorter if a clipped laser beam is undesirable or it can be longer. Ultimately the gate width needs to be less than half of the chopper period in order to minimise the effects of jitter.

Next, the delay between gates A and B is found. To set the gate delay requires a reliable and strong light source. The most convenient method of obtaining light over the spectral range of the PMT is to use an SHG crystal. The SHG crystal is placed in the beam path of the laser. Focusing the laser into the crystal produces a very strong signal which is reduced with neutral density filters with a total optical density (OD) on the order

of 5-7. Once the source is in place the delay on gate A can be scanned manually to find the maximum signal. The built-in scan function of the photon counter can also be used to better determine the best gate delay. It is only necessary to find the delay for gate A because gate B commences immediately after the chopper wheel triggers the photon counter. With the gate width and delay set, the photon counting mode is set to "A-B for T-set" and the photon counting system is ready for operation.

Appendix D

Dimensions of nanohelices

			Nominal Dimensions		Measured Dimensions		
Name	Pattern	Material	Thickness (nm)	Pitch (nm)	Height (nm)	Pitch (nm)	Handedness
A-LH (TI-539A)	8 nm x 55 nm Au	Au:Cu 80:20	500	250	81	37	LH
A-RH (TI-540A)	8 nm x 55 nm Au	Au:Cu 80:20	500	-250	81	37	RH
B-LH (TI-539B)	14 nm x 74 nm Au	Au:Cu 80:20	500	250	81	34	LH
B-RH (TI-540B)	14 nm x 74 nm Au	Au:Cu 80:20	500	-250	81	34	RH
C-LH (TI-808A)	14 nm x 79 nm Au	Au:Cu 80:20	850	425	122	51	LH
C-RH (TI-825)	11 nm x 79 nm Au	Au:Cu 80:20	850	-425	122	50	RH

Table D.1: The nominal growth parameters and measured dimensions of the nanohelices.